Telma da Piedade Silva Marques

Master of Science

Exploiting DNA UV-Vis radiation damage enhanced by nanoparticles

Thesis submitted in partial fulfillment of the requirements for the degree of

Doctor of Philosophy in

Radiation Biology and Biophysics: Biophysics Specialization

Adviser: Nigel J. Mason, Professor, University of Kent

Co-advisers: Jon P. Golding, Senior Lecture, The Open University

Maria de Fátima Guerreiro da Silva Campos Raposo, Associate Professor with Habilitation, NOVA School of Sciences and Technology

Examination Committee:

Chairperson: Orlando Manuel Neves Duarte Teodoro

Rapporteurs: Sylwia Ptasińska

Marie Davídková

Members: Pedro Manuel Brôa Costa

Nigel John Mason

FACULDADE DE CIÊNCIAS E TECNOLOGIA
UNIVERSIDADE NOVA DE LISBOA

September 2021

Exploiting DNA UV-Vis radiation damage enhanced by nanoparticles

To my dearest Pedro, Maria and João, with all my love.

“I would like to tell the young men and women before me not to lose hope and courage. Success can only come to you by courageous devotion to the task lying in front of you.”

C.V. Raman

Acknowledgements

The time has come to write the acknowledgements of all these years of hard work. So many people to acknowledge and I am so happy about that!

This was not only a thesis, it represents a chapter of my life! New country, language, food, habits, labs, climate, friends, culture, new everything while leaving my family and, in particular, my babies. I had hard times, missing so much the family, but I managed to continue working on my experiments, moving forward and never giving up because I had so many people supporting me and believing it was possible, from my dearest husband Pedro and my dearest daughter Maria (João was to small by that time but I know he was supporting Mummy too!), to Professor Nigel, what a supervisor! and Gosia, who always believed and supported me.

To Pedro, there are not enough words to tell how grateful I am! Even knowing this PhD would feel me to a different country, you told me to send my application… This says everything! We had a 3 years old daughter by that time and, still, you had never hesitated that I should pursue this opportunity to learn and increase my knowledge. You are an example to follow to me and I am sure to our babies too! To all the husbands in the world, mine is the GREATEST!

Some of the most important people that helped me during this thesis cannot read English and therefore I need to write a few lines in Portuguese for my children, my parents and my in-laws.

Queridos filhos, Maria e João, a vocês agradeço com o todo o meu coração pela vossa paciência e apoio incondicional. Por vocês, por um mundo melhor e com mais conhecimento, entramos nesta aventura. Não foi fácil estar longe de vocês, da nossa casa, do Pai, não foi fácil ver-te Maria de olhos marejados dizer: "Eu estou feliz Mãe, eu sei que voltas!", e claro que voltava, vocês são o meu tudo. Obrigada meus amores, espero um dia retribuir o carinho, apoio e confiança quando quiserem fazer Erasmus!!!

Aos meus Pais, Isabel e Henrique, agradeço todo o apoio tanto a nível pessoal como a nível familiar. Por estarem sempre disponíveis a ficar com os meus meninos e dar uma mãozinha

ao meu marido. Por me mandarem roupa quentinha para aquele país tão frio! Por nunca terem deixado de me apoiar quando eu um dia decidi sonhar mais alto e tirar um doutoramento. Sei que se orgulham muito de mim e uma grande parte do que sou hoje veio de vocês.

Aos meus Sogros, Silvina e Carlos, muito obrigada pela dedicação aos meus filhos, ao meu marido e à nossa casa. Sem a vossa ajuda e presença no dia-a-dia deles, ser-me-ia impossível ter vivido quase 2 anos em Inglaterra. Sempre saí de casa com um enorme aperto no coração mas apenas pelas saudades que eu já tinha, nunca por achar que a minha família não ia ficar bem. Agradeço de coração todo o vosso apoio, compreensão e carinho ao longo destes anos.

To my brother Bruno and his lovely family, thank you for all the encouragement and support.

After these important acknowledgements, I want to thank my Supervisor, Professor Nigel Mason. It was a great honour to meet and work with you! I am very grateful for the opportunity to engage in this PhD. Professor Nigel always had five minutes to hear my concerns and/or achievements. Thank you for the challenges and opportunities you have offered me while I was your student!

To Professor Maria de Fátima Raposo, my Co-Supervisor, for all the support through this thesis and for always being available for me. Thank you for pushing me up in difficult times and inspire me.

To Professor Sam Eden, thank you very much for accepting me into your lab and for all the great discussions of the results.

To Professor Jon Golding, it was great to have all that brainstorming meetings, chasing for the answers to my results. I have learned so much from you and Gonçalo Ferreira.

To Ilko Bald, Robin Schürmann and Ilko's group, thank you for training me operating Nd:YAG lasers and for sharing your knowledge and expertise. My first steps in this PhD were with you but I had your support until the last stage of the thesis.

To the MBN Research Center Team, especially to Prof. Dr. Andrey V. Solov'yov, for the kind welcome and fantastic teaching in my first contact with computational modelling software for simulation of molecular structure and dynamics of Meso-Bio-Nano (MBN) systems.

One of the best things in life is to meet new people and share great moments with them and for sure, this PhD allowed me to meet outstanding people from so many different countries! I also want to thank to my Milton Keynes friends Janiska, Yaduzinho, Suraj, Nitu, Sophie, Kasia, Gonçalo and Carlos. In different ways and periods of my life in the UK, these are the people I call friends for life. What a pleasure to meet all of you and share amazing experiences from the relaxing moments, parties, BBQ's, games night to all the social events that cheered up my life. Because of these and many other reasons, THANK YOU so much! I want also to thank all my friends and PhD colleagues, especially to Filipa Pires, Gonçalo Ferreira, Alexandra Loupas, André Rebelo, Tiago Cunha, Guilherme Meneses, Alessandra Barbosa, João Ameixa, among many others, with whom I have spent joyful moments and have learned so much.

Gosia, you are the greatest of all times! A model to follow, a mentor! Such an amazing woman, so intelligent, so humble and friendly! I was lucky to meet you, to share beam-time with you. I am really thankful for all the opportunities you gave me, for all the knowledge you have shared and for always believe that I was able to accomplish this thesis. THANK YOU, dear Boss!

I would never forget the support from my life friends, Helena Marcos and Filipa Dinis. You make my life seem easier!

I am grateful for the OU's logistical support and for the technical support provided by C. Hall, R. Seaton, T. Webley, D. Pound and their colleagues in building and maintaining the experiment. Finally, I want to thank Michael Batham (OU) and Oddur Ingolffson (University of Iceland) for providing the UV-Vis spectrometer and the pulsed Nd:YAG laser, respectively.

I would like to acknowledge Prof. Dr. Paulo Limão–Vieira, as a coordinator of the Radiation Biology and Biophysics Doctoral Training Programme (RaBBiT), for the opportunity to pursue my PhD and always rapidly solved a lot of bureaucracy. I would also like to thank the Executive

Committee of the RaBBiT. I am, as well, very grateful to all the lectures given by the RaBBiT Professors, from whom I have learned so much.

Finally, I would like to thank the Department of Physics of NOVA University of Lisbon and CEFITEC through UID/FIS/00068/2020 and PTDC/FIS-NAN/0909/2014, the financial support from The Open University and from the Fundação para a Ciência e a Tecnologia (FCT-MCTES) through PD/BD/106032/2015 scholarship. This work was also supported by Radiation Biology and Biophysics Doctoral Training Programme (RaBBiT, PD/00193/2012); Applied Molecular Biosciences Unit – UCIBIO (UID/Multi/04378/2020).

Abstract

Cancer therapy has been a prominent topic of study for several decades by the medical, academic and pharmaceutical industry communities. In particular, skin cancer has assumed high relevance due to the degradation of the ozone layer and consequent increase in human exposure to UV radiation that induces genetic mutations. The focus has been on novel treatments and agents that increase the effectiveness of therapies, destroying the tumour cells while sparing the surrounding healthy tissues. The aim of this work was to analyse the damage driven by UV and visible radiation in relevant biological molecules and to understand how to enhance the radiation damage, namely by adding AuNPs to illuminated samples. A combination of different techniques represents an innovative and promising approach to be explored. The work described in this thesis addresses this methodology from two different standpoints: 1) the degradation of DNA molecules after exposure to UVC radiation, to design a biological dosimeter that effectively demonstrates and measures the radiation induced damage; and 2) the effects of visible light laser radiation (Nd:YAG) on halogenated nucleobases and plasmid DNA conjugated with gold nanoparticles (AuNPs). The radiation damage induced in biological molecules was evaluated by spectroscopic techniques, microscopies, electrophoresis and measuring the production of free radicals and reactive species during water photolysis. This thesis demonstrates the potential of such a combined chemo-phototherapy methodology and the effectiveness of AuNPs in such treatment. Moreover, we have proven damage enhancement with the combination of pulsed laser and AuNPs in relevant biological molecules. The new findings of the interaction of Nd:YAG light with AuNPs and DNA molecules point to their efficacy and applicability in melanoma therapy. However, additional *in vitro* studies with cell lines, followed by *in vivo* assays, should be conducted, investigating whether the benefits surpass the possible damage caused in the vicinity of the illuminated area.

Keywords: DNA, nucleobases, AuNPs, UV radiation, Nd:YAG.

Resumo

A terapia de cancro, dos mais variados tipos de tumores e possíveis combinações de tratamentos, tem sido tema de estudo há várias décadas por parte das comunidades médica, académica e indústria farmacêutica. Nomeadamente o cancro de pele tem assumido elevada relevância devido à degradação da camada de ozono e consequente exposição a radiações que induzem mutações genéticas. Novos tratamentos, agentes que aumentem a eficácia das terapias com menor dano de células saudáveis, e a conjugação destes dois, representam novas e promissoras técnicas a ser exploradas. Assim, o uso de nanopartículas de metais nobres e a terapia com fotões são práticas cada vez mais procuradas na terapia do cancro de pele. Este trabalho estuda esta problemática com duas abordagens diferentes, nomeadamente 1) estudos da degradação de moléculas de ADN após a exposição a radiação UVC, com o objectivo de conceber um dosímetro biológico que demonstre de uma forma eficaz os danos induzidos; e 2) investigação dos efeitos em nucleobases halogenadas e plasmídeo de ADN da conjugação de nanopartículas de ouro (AuNPs) e radiação no espectro do visível com um feixe de luz a 532 nm produzido por um laser pulsado (Nd:YAG). Os danos induzidos nas moléculas biológicas referidas anteriormente foram avaliados recorrendo a técnicas de espectroscopia, caracterização por microscopia, separação molecular por electroforese e avaliação da produção de radicais livres e espécies reactivas formadas durante a fotólise da água. Este trabalho demonstrou o potencial da quimio-fototerapia combinada estudada, e comprovou eficácia das AuNPs. As novas descobertas da interação de AuNPs com Nd:YAg e moléculas de ADN apontam para a sua eficácia e aplicabilidade em tratamentos de melanomas, contudo mais estudos *in vitro* com linhas celulares, seguidos por ensaios *in vivo* devem ser realizados, investigando se os benefícios são superiores aos possíveis danos causados na proximidade da área iluminada.

Palavras-chave: ADN, nucleobases, AuNPs, radiação UV, Nd:YAG.

Contents

Chapter 3

Chapter 6

Chapter 7

Chapter 8

Annex I

List of Figures

Chapter 2

Chapter 3

Chapter 4

Chapter 5

Chapter 6

Chapter 7

List of Tables

Chapter 3

Chapter 4

Chapter 5

Chapter 6

Chapter 7

Acronyms and Symbols

The list of abbreviations is sorted in alphabetic order and refers to the main text of this thesis.

$^1O_2$	Singlet oxygen
3-CCA	Coumarin-3-carboxylic acid
5BrU	5-Bromouracil
5FU	5-Fluorouracil
7-OHCCA	7-hydroxycoumarin-3-carboxylic acid
A	Adenine
A_{beam}	Area of the circular beam
AB	Atom abstraction
Abs	Absorbance
AFM	Atomic force microscopy
AGE	Agarose gel electrophoresis
$AgNO_3$	Silver nitrate
ATR	Attenuated total reflection
$AuHCl_4$	Chloroauric acid
AuNP	Gold nanoparticle
bp	Base pairs
Br	Bromine
c_{NB}	Concentration of nucleobases
C	Cytosine
C_D	Characteristic dose constant
CaF_2	Calcium fluoride
c_{max}	Maximum concentration of adsorption sites
D	Absorbed dose
DEA	Dissociative electron attachment
DFT	Density functional theory

DHR-123	Dihydrorhodamine-123
DLS	Dynamic light scattering
DNA	Deoxyribonucleic acid
DSB	Double strand break
e	Charge of an electron ($1.602 \times 10^{-19}\ C$)
E. coli	*Escherichia coli*
EB	Ethidium bromide
EDTA	Ethylenediaminetetraacetic acid
EtOH	Ethanol
FDTD	Finite domain time difference
FTIR	Fourier transform infrared
FWHM	Full width half at maximum
ET	Electron transfer
EtOH	Ethanol
G	Guanine
$\hbar$	Planck constant ($1.034 \times 10^{-34} J.s$)
H_2O_2	Hydrogen peroxide
HAT	Hydrogen Atom Transfer
HCL	Hydrochloric acid
IB	Interband
IR	Infra-red
k	Rate constant
k_1	Rate constant at time equal to 1
k_{ad}	Adsorption rate constant
k_{obs}	Observed rate constant
kbp	kilo base pairs
KBr	Potassium bromide
l	Length of the optical path

L	Linear
Laser	Light Amplification by Stimulated Emission of Radiation
LB broth	Luria-Bertani broth
LEE	Low energy electron
ln	Natural logarithm
LSP	Localized surface plasmons
LSPR	Localized surface plasmon resonance
mRNA	Messenger ribonucleic acid
N_{Puls}	Number of laser pulses
NaOH	Sodium hydroxide
NB	Nucleobase
Nd:YAG	Neodymium-doped yttrium aluminum garnet
NIR	Near infrared
$NO^{\bullet}$	Nitric oxide
NP	Nanoparticle
$O_2^{-\bullet}$	Superoxide anion radical
O_3	Ozone
$OH^{\bullet}$	Hydroxyl radical
ONOO-	Peroxynitrite
PBS	Phosphate-buffered saline
pHN	Natural pH
PTT	Photothermal therapy
QS	Quartz glass high performance
R	Relaxed
RA	Radical addition
RHD-123	Rhodamine-123
RNA	Ribonucleic acid
RNS	Reactive nitrogen species

ROS	Reactive Oxygen Species
RT	Room temperature
SAR	Specific absorption rate
SERS	Surface enhanced Raman scattering
SC	Supercoiled
SD	Standard deviation
Si	Silicon
SI	Supporting Information
SP	Surface plasmon
SPR	Surface plasmon resonance
SSB	Single strand break
ssDNA	Single stranded DNA
t	Time
T	Thymine
TAE	Tris-acetate EDTA
TBE	Tris-borate-EDTA
TEM	Transmission electron microscopy
TRIS	Tris(hydroxymethyl)aminomethane
U	Uracil
UHPW	Ultra-high purity water
UHV	Ultra-high vacuum UV
UV	Ultraviolet
UV-Vis	Ultraviolet and visible
Z	Atomic number
Z	Distance from the focus of the laser beam
ε	Extinction coefficient
λ	Wavelength
σ_{abs}	Absorption cross section
σ_{ext}	Extinction cross section

σ_{sca}	Scattering cross section
σ_{SB}	Strand break cross section

Chapter 1

Introduction

Introduction

1.1. Motivational framework

"Nano" is one of the prefixes of the last three decades. In a simple search on a web browser one can find so many new words and different applications of the nano prefix such as nanotechnology, nanoscience, nanomaterials and relevant for this thesis, nanomedicine, nanotoxicology and nanoparticles with the exciting possibilities these brings for cancer treatment.

Cancer is not a new disease, nevertheless we are still far away from having a perfect treatment and sadly for some types of tumours, there is still no effective treatment. According to the World Health Organization, trachea, bronchus and lung cancers deaths are ranked as the 6th leading cause of death in the world, rising from 1.2 million in 2000 to 1.8 million in 2019. Such numbers are even scarier when we account for the considerable investment that has occurred in seeking methods of treatment of such tumours. More technologies and knowledge have become available but the number of deaths continues to increase.

The success of any cancer therapy depends on the efficacy of the treatment, which usually is directly related with the cell death rate [1]. A cell is considered dead when it loses the ability to replicate the genomic information, and thus pass the genes to daughter-cells [2], [3], and a single double strand break (DSB) is known to be able to cause this effect [4], [5]. Ongoing research aims at discovering chemicals with anti-tumour activity to be used on their own or combined with conventional photothermal therapy (PTT), radiotherapy or chemotherapy [6]–[8].

In recent years, different techniques have been developed with the purpose of using pulsed and continuous wave lasers in PTT. Nobel metal nanoparticles are of particular interest in skin cancer treatment with PTT. It is well known that depending on the material, size, structure and shape of the nanoparticle, they present a surface plasmon resonance that can enhance the damage and death of tumour cells during PTT [6], [9], [10].

Gold nanoparticles (AuNPs) are a common choice to be used in PTT since they present biocompatibility and an extraordinary capability to absorb visible light, converting the photon's energy into heat. In pulsed laser the heat generated originates a significant rise of the temperature in the vicinity of the AuNPs, culminating in the damage of the nearby biological material [10], [11]. The irradiation of biological molecules in presence of AuNPs thus leads to DNA damage through temperature increase. However with continuous wave lasers the damage in the cells is caused by hyperthermia, that basically correspond to small increases of the local temperature that lead to denaturation of proteins, modification of the cellular response, disruption of nuclear and cytoskeletal assemblies and membrane blebbing [1], [3], [12]–[14].

The water existent in the irradiated medium also experiences radiolysis leading to the formation of free radicals species (mostly $OH^{\bullet}$ and H_2O_2) and low energy electrons, indeed these entities are responsible by the majority of the DNA damage [15], [16]. Laser irradiation may lead to photodissociation of the water and when incident upon the NPs liberate secondary low energy electrons.

The main objective of this work was understanding the effect in the applications that cause biological damage by sources of light usable in PTT when combined with gold nanoparticles (AuNPs). More concretely, the main objective of this work was understand the effect of radiation in presence of AuNPs on DNA and DNA bases. Another goal was to investigate the production of free radicals during the irradiations of the samples and study the effects on the plasmid DNA, analysing the formation of single and/or double strand breaks with the technique of agarose gel electrophoresis.

This thesis is structured in eight Chapters. In Chapter 1 the reader will find a general introduction to the thesis theme, the relevancy and context of this particular study and the thesis outline. Chapter 2 provides a review of the state of the art of the principal themes addressed in this study. The key concepts are defined and the effects of irradiation of biological molecules are reviewed. The impact of the free radicals in biological damage is also discussed. In the Chapter 3, the instrumental techniques used in the experiments performed in this study are presented. Chapters 4 to 7 of this thesis are presented in manuscript form,

based on a series of peer-reviewed papers published or submitted for publication. The contents of each of the four results chapters are:

- **Chapter 4:** Assessment of the biological damage caused when aqueous solutions of *Calf thymus* DNA are exposed to UV light for different periods of time. The hypothesis of using DNA as a biodosimeter is considered. Publication: Marques, T.S., Pires, F., Magalhães-Mota, G., Ribeiro, P.A., Raposo, M., Mason, Nigel (2018) Development of a DNA Biodosimeter for UV radiation. Proceedings of the 6th International Conference on Photonics, Optics and Laser Technology. 1. pp. 328-333. SCITEPRESS. ISBN 978-989-758-286-8; doi: 10.5220/0006732003280333.
- **Chapter 5:** Investigation of the kinetics of molecular decomposition of 5-bromouracil irradiated with Nd:YAG laser light in the presence of AuNPs. Publication: Telma S. Marques, Robin Schürmann, Kenny Ebel, Christian Heck, Małgorzata A. Śmiałek, Sam Eden, Nigel Mason and Ilko Bald. Kinetics of Molecular Decomposition under Irradiation of Gold Nanoparticles with nanosecond Laser Pulses – A 5-Bromouracil case study. The Journal of Chemical Physics, 152, 124712 (2020); doi: 10.1063/1.5137898. Impact Factor - 3.488 (2020).
- **Chapter 6:** Evaluation of the effects on halogenated nucleobases when illuminated with Nd:YAG nano-pulsed laser. The presence and absence of AuNPs is exploited and the surface plasmon resonance (SPR) excitation studied. Publication: T.S. Marques, M.A. Śmiałek, R. Schürmann, I. Bald, M. Raposo, S. Eden and N.J. Mason. Decomposition of halogenated nucleobases by SPR excitation of gold nanoparticles. European Physical Journal D, Section: Atomic and Molecular Collisions. pp. 1-9, 74, 222 (2020). ISSN: 1434-6060; doi: 10.1140/epjd/e2020-10208-3. Impact Factor - 1.425 (2020).
- **Chapter 7:** Study of free radicals on biological damage of aqueous solutions of plasmid DNA in presence and absence of AuNPs and irradiated with Nd:YAG pulsed laser. Manuscript being prepared for submission.

At the end of this thesis, a summary of the results is presented as well as future work possibilities in this area to improve the success of the AuNPs in skin cancer treatment (Chapter 8). A list of relevant references is also provided as a subsection within each chapter.

1.2. References

[1] R. Schürmann and I. Bald, "Real time monitoring of Plasmon induced Dissociative Electron Transfer to the Potential DNA Radiosensitizer 8-Bromoadenine .," 2017.

[2] J. Rak *et al.*, "Mechanisms of Damage to DNA Labeled with Electrophilic Nucleobases Induced by Ionizing or UV Radiation," *Journal of Physical Chemistry B*, vol. 119, no. 26. American Chemical Society, pp. 8227–8238, 02-Jul-2015.

[3] P. Gananathan, A. P. Rao, G. Singaravelu, and E. Manickam, "Review of Laser in Nanophotonics – A Literature Study for Cellular Mechanism," 2017.

[4] P. A. Jeggo and M. Löbrich, "DNA double-strand breaks: Their cellular and clinical impact?," *Oncogene*, vol. 26, no. 56. Oncogene, pp. 7717–7719, 10-Dec-2007.

[5] M. A. Smialek, "Evaluating experimental molecular physics studies of radiation damage in DNA," 2016.

[6] S. Grellet *et al.*, "Cancer-selective, single agent chemoradiosensitising gold nanoparticles," *PLoS One*, vol. 12, no. 7, 2017.

[7] H. Wang, X. Mu, H. He, and X.-D. Zhang, "Cancer Radiosensitizers," *Trends Pharmacol. Sci.*, vol. 39, no. 1, pp. 24–48, 2018.

[8] The Lancet Oncology, "The real worth of cancer drugs," *The Lancet Oncology*, vol. 21, no. 12. Lancet Publishing Group, p. 1537, 01-Dec-2020.

[9] M. B. Ferruz *et al.*, "New research in ionizing radiation and nanoparticles: The ARGENT project," in *Nanoscale Insights into Ion-Beam Cancer Therapy*, A. Solov'y., Springer, Ed.

Springer International Publishing, 2016, pp. 379–434.

[10] N. S. Abadeer and C. J. Murphy, “Recent Progress in Cancer Thermal Therapy Using Gold Nanoparticles,” *Journal of Physical Chemistry C*, vol. 120, no. 9. American Chemical Society, pp. 4691–4716, 10-Mar-2016.

[11] Y. Zheng and L. Sanche, “Gold Nanoparticles Enhance DNA Damage Induced by Anti-cancer Drugs and Radiation,” *Radiat. Res.*, vol. 172, no. 1, pp. 114–119, Jul. 2009.

[12] R. R. Letfullin, C. Joenathan, T. F. George, and V. P. Zharov, “Laser-induced explosion of gold nanoparticles: potential role for nanophotothermolysis of cancer,” *Nanomedicine*, vol. 1, no. 4, pp. 473–480, 2006.

[13] L. A. Dykman and N. G. Khlebtsov, “Gold nanoparticles in chemo-, immuno-, and combined therapy: review [Invited],” *Biomed. Opt. Express*, vol. 10, no. 7, p. 3152, Jul. 2019.

[14] D. Jaque *et al.*, “Nanoparticles for photothermal therapies,” 2014.

[15] L. Sanche, “Biological chemistry: Beyond radical thinking,” *Nature*, vol. 461, no. 7262. Nature, pp. 358–359, 17-Sep-2009.

[16] C. von Sonntag, *Free-Radical-Induced DNA Damage and Its Repair*. 2006.

Chapter 2

Introductory Concepts

Introductory Concepts

In this chapter, the background to the experimental work undertaken and reported in this thesis is exploited. The main concepts and knowledge of the mechanisms and principles of radiation damage in DNA as we understand them today are presented. The need to increase the knowledge on the mechanisms by which radiosensitisers enhance radiation damage and the biological effects of different radiations will be explored/evidenced.

2.1. DNA and RNA

Deoxyribonucleic acid (DNA) and Ribonucleic acid (RNA) are the most relevant biological molecules since DNA carries the genetic information, i.e., instructions for the development, functioning, growth and reproduction of living organisms and virus. While RNA presents various biological roles in coding, decoding, regulation and expression of genes. First described by Watson and Crick [1], DNA consists of two double chains composed by the nucleotides Guanine (G), Adenine (A), Cytosine (C), and Thymine (T). The first two nucleotides are purine molecules while the last are pyrimidine molecules. Nucleotides are bonded together through phosphate groups, ribose sugars and hydrogen bonding. To form the double-strands, the four nucleobases are interlinked with each other by Watson-Crick base pairing which means that two complementary base pairs such as G-C and A-T are connected via hydrogen bonds (Figure 2.1) [1].

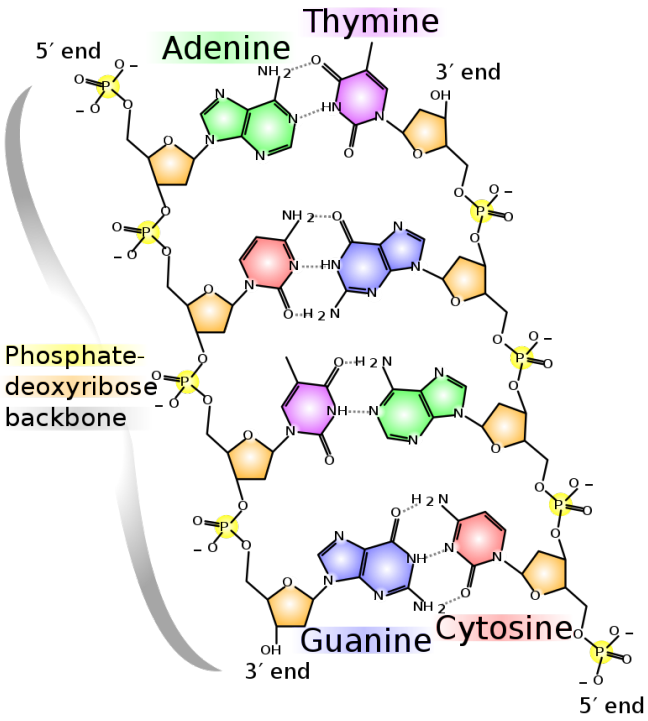

Figure 2.1 – Chemical structure of DNA with the representation of the four nucleobases, Adenine (green), Thymine (purple), Cytosine (red) and Guanine (blue), the phosphate groups (yellow) and the deoxyribonucleic sugars (orange). The atoms shown are P=phosphorus, O=oxygen, N=nitrogen and H=hydrogen. In Wikimedia.

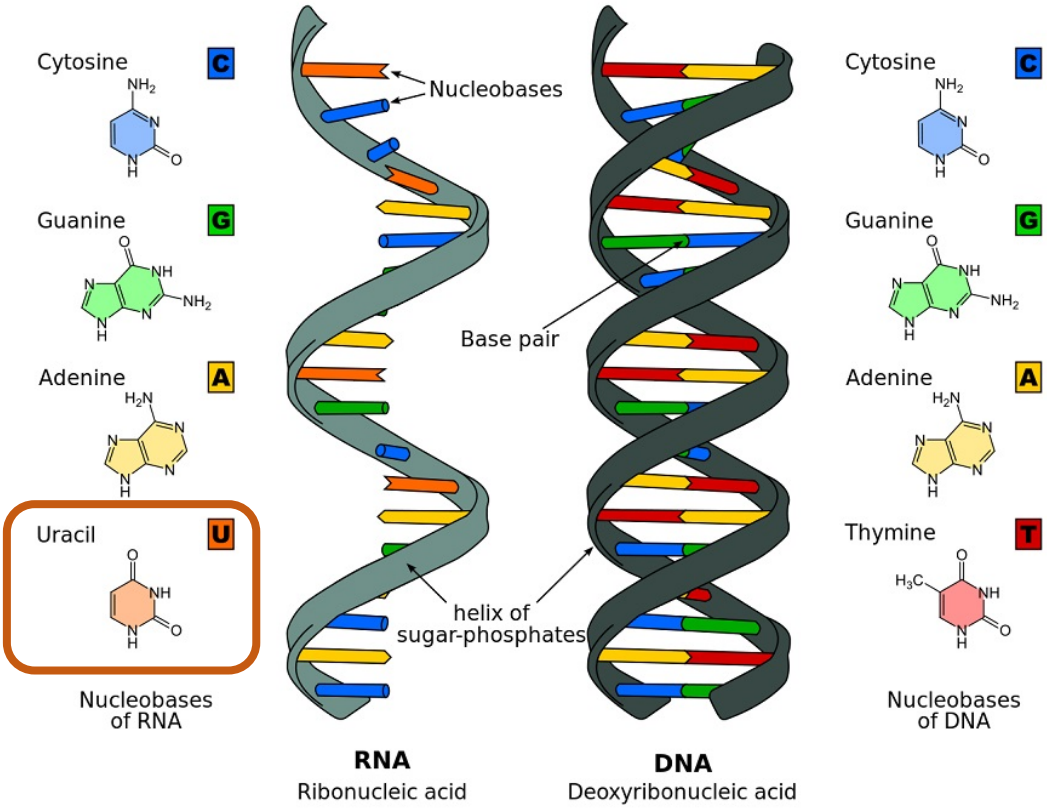

Figure 2.2 – DNA and RNA nucleobases and helix structure. Adapted from [2].

The duplication of the genetic information and transmission to the daughter cells is achieved by the unique sequence of the bases that make DNA. DNA and RNA are the two types of nucleic acids, polymers based on nucleotides, and the main difference between the two is related to the sugar present in the structure and the pyrimidines. In DNA one can find 2'-deoxyribose and T and C are the pyrimidines bases present. On the other hand, RNA contains the sugar ribose and the pyrimidine base T is replaced by uracil (U) (Figure 2.2). In both biological molecules, the nucleotides are joined together through phosphodiester linkages between the hydroxyl group of one pentose in position 5' and the hydroxyl group in position 3' of the next sugar [3]–[6]. The base-pair G-C has 3 hydrogen bonds and A-T only presents two (Figure 2.3).

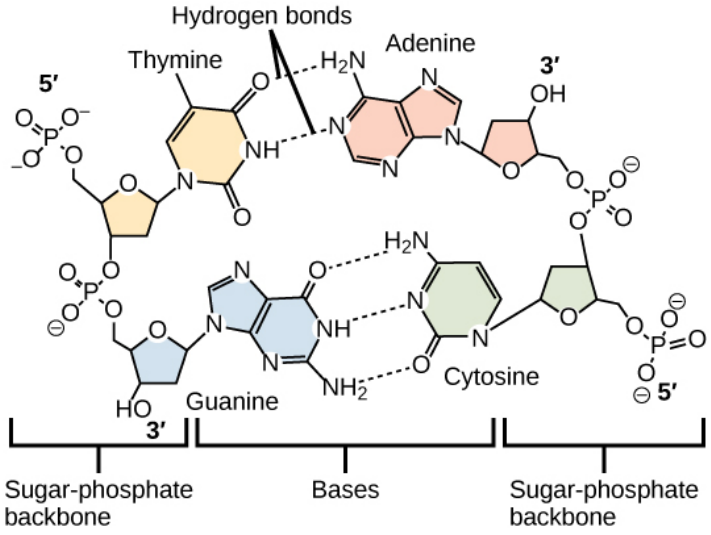

Figure 2.3 – Model of DNA by Watson and Crick with the representation of the hydrogen bonds. Adapted from https://cnx.org/contents/5CvTdmJL@4.4

DNA strands have an antiparallel orientation, which means that the sequence is always written with the 5' end at the left strand and the 3' end at the opposite side (Figure 2.3), and each helical turn has 10.5 base pairs, corresponding to 36 Å (3.6 nm) [3], being the distance between base pairs near 3.4 Å [7] and recently, calculated as 3.3899±0.0002 Å [8]. The stabilization of the double helix is attributed to metal cations, shielding the negative charges of the backbone phosphates [9], and to the base-stacking of the planar purines and pyrimidines. The hydrogen bonding of the complementary bases does not have a significant contribution to this stabilization. Moreover, DNA molecules with a higher rate of G-C are more stable since this bonding is stronger than the connection of the other complementary bases [3], [4], [6].

2.2. Purines and pyrimidines

As already mentioned, the building blocks of the DNA and RNA are nucleotides which are purine and pyrimidine derivatives. Pyrimidines (Figure 2.4), chemical formula $C_4H_4N_2$, are characterized by having a single ring containing four carbon and two nitrogen atoms forming a planar molecule, while purines (Figure 2.4), with chemical formula $C_5H_4N_4$, presents a fusion between the pyrimidine ring and imidazole ring, and assumes a very nearly planar geometry [3], [6]. These structures are aromatic molecules (Figure 2.4), a crucial factor in the structure, electron distribution, and light absorption of nucleic acids. The pyrimidines and purines are weakly basic compounds and this is the reason why they are commonly known as bases. In both types of bases, the rings are planar due to the conjugated double bonds and the fact that these bases are unsaturated.

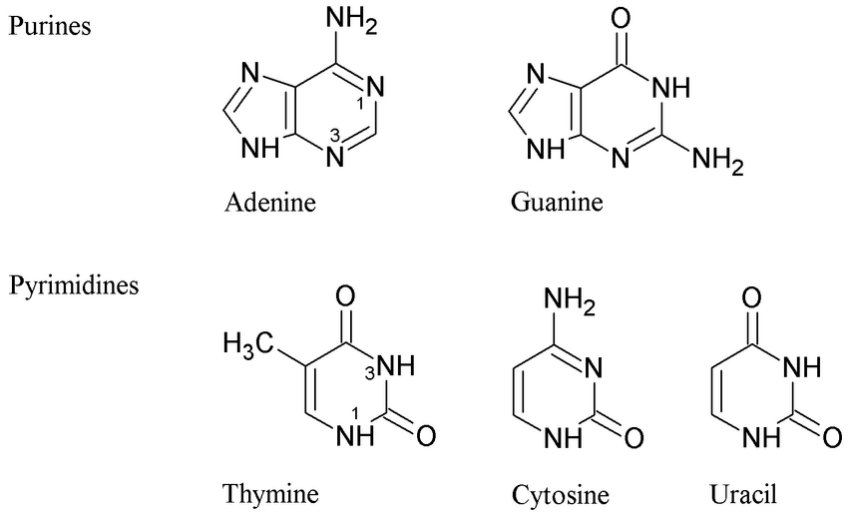

Figure 2.4 – Parent structures of pyrimidine ring and purine bases of nucleotides and nucleic acids, showing the numbering conventions. Adapted from [10].

The geometry of these molecules make them more susceptible of injury from ultraviolet (UV) light since they have the ability of strongly absorb this radiation, showing absorption from 200 to 300 nm, depending on the nucleotide as shown in Figure 2.5 [3], [11]. Concerning the DNA absorption spectrum, it typically presents a peak at 260 nm and a local minimum around 230 nm, which reflects the contribution of the bases that compose the DNA strands. The

absorption spectra of purines and pyrimidines present a peak about 250 to 270 nm and a second one around 180 to 200 nm, both assigned to π-π^* transitions [12].

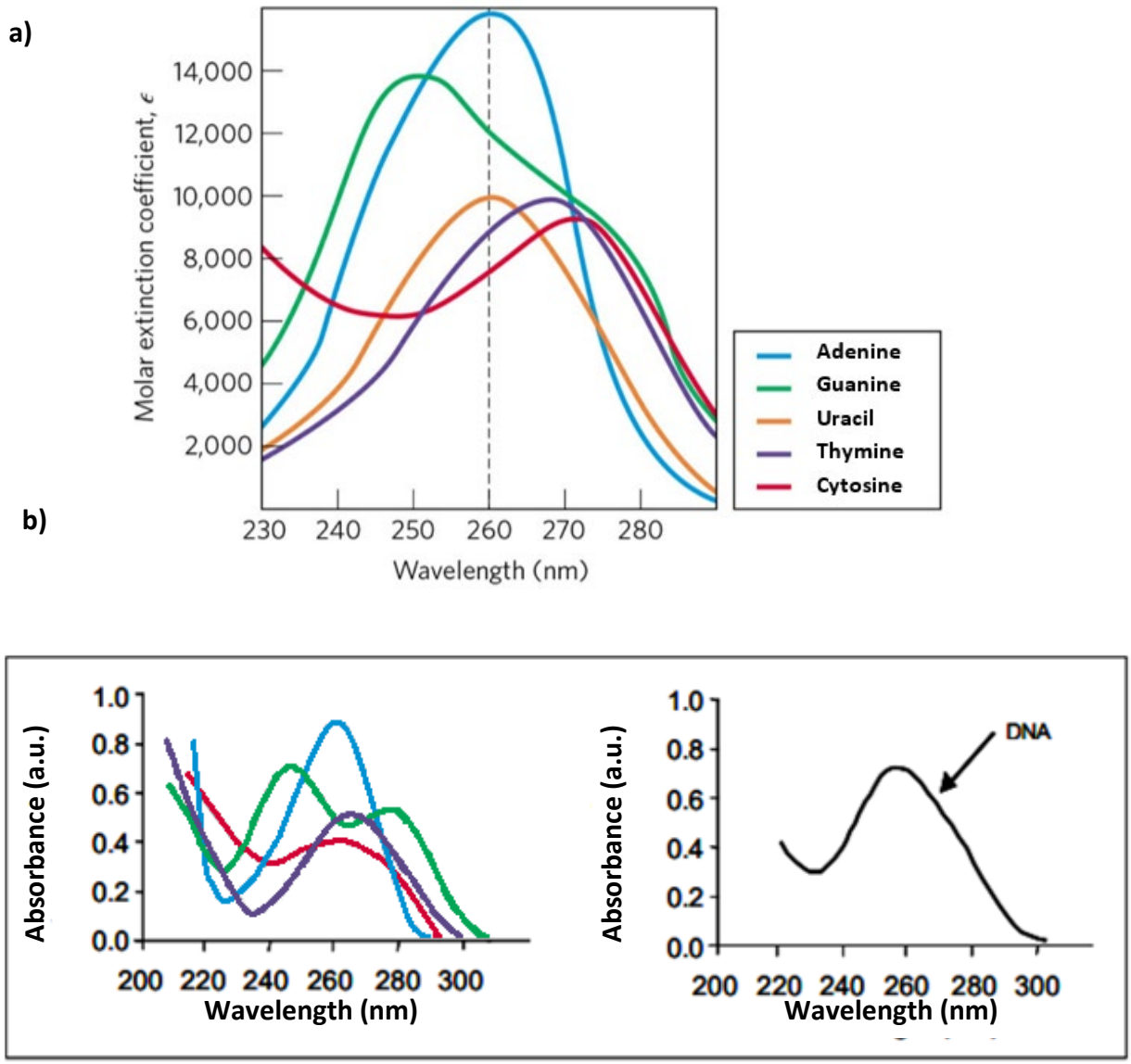

Figure 2.5 – Absorption spectra at pH 7, a) variation of the molar extinction coefficient with the wavelength of individual nucleotides [3] and b) variation of the absorbance with the wavelength for the nucleotides (left) and DNA (right). Adapted from [11].

2.2.1. DNA damage

The damage in DNA molecules can occur in all its parts, although there are some more regions that are more susceptible to damage such as the sugar-phosphate backbone or the single and double-strand breaks (SSB and DSB, respectively). Damage can be caused by several causes, namely ionizing radiation, particles beam [13], UV radiation [8], [9], [14], [15], the action of free radicals and chemical attack [3], [4], [12], [16]. DNA bases can also be severely modified or damaged by oxidation. If such damage occurs during the replication of DNA, errors can ensue such as mispairing, addition of extra bases or, in the other extreme, its omission (Figure 2.6) [16], [17].

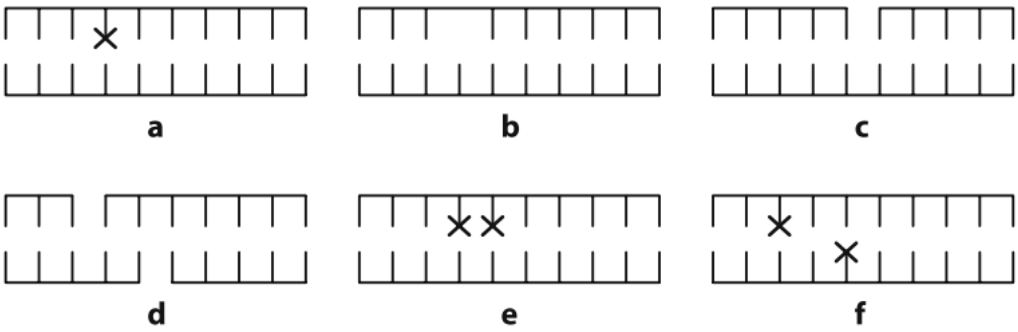

Figure 2.6 – Illustration of several types of DNA damage, namely a) base damage; b) apyrimidinic/apurinic site; c) SSB; d) DSB; e) tandem lesion; f) clustered lesion with two damaged bases on opposite strands. Adapted from [16].

According to Jagger (1967), the parent structure of the pyrimidine bases has a higher susceptibility of being attacked than purines since this group of bases present a simpler structure [18]. The damaged induced in pyrimidines can lead to 1) formation of pyrimidine dimers, 2) production of photo products, 3) protein-DNA cross-links, 4) pyrimidine hydrates, 5) SSB and/or DSB and 6) DNA-DNA cross-links [11]. The analysis of UV damage over the photon range of 3.5 to 8 eV on DNA films has revealed that such irradiation leads to: 1) sugar degradation with CO-based compounds released at energies above 6.9 eV, 2) nitrogen groups which are not involved in hydrogen bonding decrease for energies above 4.2 eV; 3) phosphate groups decrease for energies above 4.2 eV; 4) the damage on bases peripheral nitrogen atoms follows the damage on phosphate groups, this is explained by the ejection of low kinetic energy photoelectrons from the DNA bases, as a result of UV light-induced the

breaking of the phosphate ester groups which forms a transient anion with resonance formation in the nitrogen DNA peripheral groups; and 5) ionized phosphate groups are kept unchanged which is interpreted by the shielding of phosphate groups caused by water molecules hydration near sodium atoms [9].

Regarding DNA damaged molecules in aqueous solution, the damage is typically induced by processes related with reactive oxygen species (ROS) which attack the strands. This effect is closely related to the fact that the DNA molecule is a highly charged polyanion always surrounded by water molecules, even when it is in the dry state (not in solution), containing twelve water molecules per nucleotide subunit [16].

2.2.2. Oxidative stress of DNA

Oxidation, in biological systems, occurs due to the action of free radicals and refers to the removal of one or more electrons from a molecule. Free radicals are chemical species with an unpaired electron, which translates in a large electronic affinity and therefore vast reactivity (Figure 2.7). The formation of free radicals may occur due to endogenous processes, such as biochemical processes associated with metabolism, or via exogenous process, for instance, the metabolic reactions caused by the exposure to external agents [19]–[21].

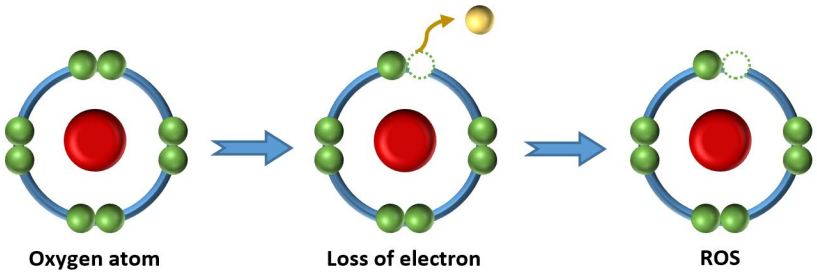

Figure 2.7 – Illustration of reactive oxygen species formation with oxygen as a precursor. The loss of an electron will originate the free radical. Adapted from [22].

A balance between oxidation and reduction is essential in all biological systems and chemical reactions, and when this equilibrium is not present it is called oxidative stress. Oxidative stress results in an intracellular increase of reactive species, namely reactive oxygen species (ROS) and reactive nitrogen species (RNS). As examples of ROS we have hydrogen peroxide (H_2O_2),

singlet oxygen ($^1O_2$), the superoxide anion radical ($O_2^{-\bullet}$), ozone (O_3) and hydroxyl radical ($OH^\bullet$). Peroxynitrite (ONOO-) and nitric oxide ($NO^\bullet$) are examples of RNS [20], [23]. Oxidative damage is the most important source of mutagenic alterations in DNA. DNA damage can result from ROS activity or as a by-product of aerobic metabolism and leading to the oxidation of DNA and strand breaks [3], [22], [24] (Figure 2.8).

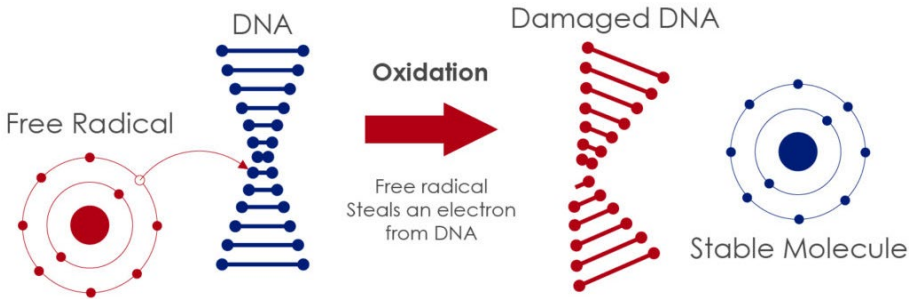

Figure 2.8 – Representation of the indirect effect of DNA damage by free radicals. Adapted from [25].

In general, free radical reactions are divided into three groups: atom abstraction (AB), electron transfer (ET), and radical addition (RA). The products formed during these reactions will interact with biological systems and lead to damage. On other hand, ROS and RNS are commonly divided into two groups, 1) radicals and 2) non-radicals. The main differences between them are that radicals contain at least one unpaired electron and are not capable of independent existence, and the group of the non-radicals is characterised for having all the electrons paired and thus are stable molecules, but they are capable of leading to free radical reactions in the biological medium [23], [24], [26], [27].

Antioxidants may exhibit distinct behaviour when reacting with different free radicals and pro-oxidants. The two main mechanisms of radical inhibition by the action of antioxidants are hydrogen atom transfer and single electron transfer (Figure 2.9), which differ essentially in the kinetics and reaction medium. These mechanisms can occur simultaneously, with the dominant mechanism being determined by the properties, structure and antioxidant solubility and the nature of the reaction system solvent [19], [23], [28]. Electron transfer reactions generally occur slower than hydrogen atom transfer reactions. Moreover, cell functions or cell damage can be altered by the molecular changes mediated in redox steady states, depending on the nature and extent of the effect [28].

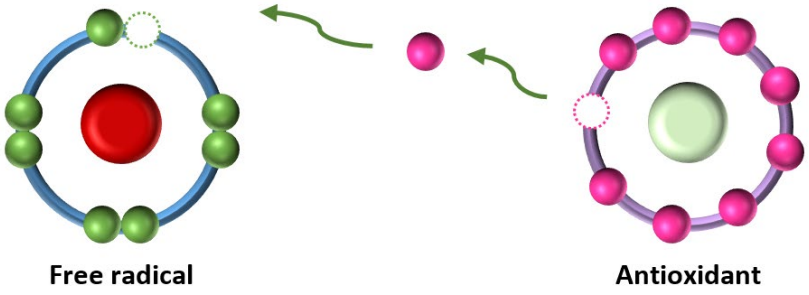

Figure 2.9 – Representation of antioxidant neutralising a free radical by donation of an electron [22].

In the following sections, a detailed description of the ROS species is presented.

2.2.2.1. Hydroxyl radical

The hydroxyl radical ($OH^{\bullet}$; Figure 2.10) is known for being the most reactive species containing oxygen and presents a half-life of about 1 nanosecond (ns), or 10^{-9} second [26], in biological systems [23], [24], [26]. $OH^{\bullet}$ is a very unselective radical, thus its action does not depend on the surrounding molecules. The formation of $OH^{\bullet}$ in biological systems happen by water radiolysis or photolysis. The methods commonly used for the detection of this free radical presence and activity, are based on the fluorescence emitted by a characteristic product of a given probe added to the medium of reaction. This chemical (e.g. coumarin-3-carboxylic acid, phenylalanine or salicylic acid) is feasible for the *in vitro* detection but not for *in vivo*, and the most common reactions related are named aromatic hydroxylation [23], [29], [30].

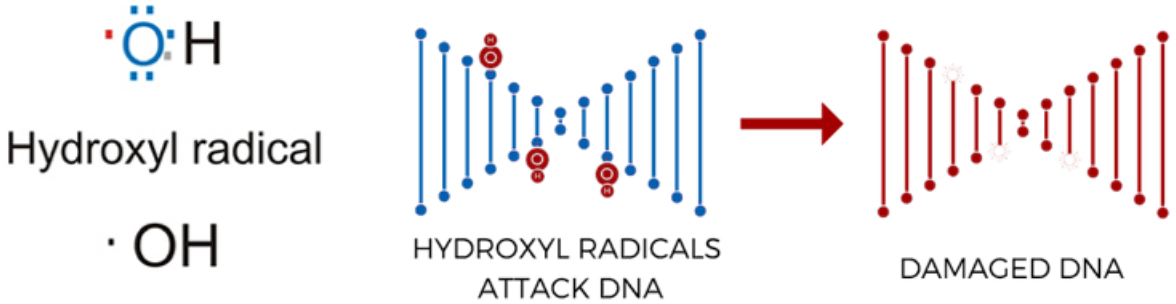

Figure 2.10 – Representation of hydroxyl radical with an unpaired electron in red and the attack of this species to DNA chain. Adapted from [31], [32].

2.2.2.2. Singlet oxygen

Singlet oxygen ($^1O_2$; Figure 2.11) is an oxidant with high impact in tissue and DNA damage, presenting the capacity to react with a wide range of biological molecules. Usually, $^1O_2$ formation is related with the capacity to accept electrons of the medium being exceeded when exposed to intense light [3], [16], [24], [26]. The half-life of singlet oxygen is relatively short, 10^{-6} second [26] and belongs to the class of non-radical species. The *in vivo* production of this molecule is associated with the activation of blood cells or through enzymatic reactions [26].

Figure 2.11 – Representation of singlet oxygen [32].

2.2.2.3. Superoxide anion radical

The most common ROS formed via enzymatic processes is the superoxide anion radical ($O_2^{-\bullet}$; Figure 2.12), which is formed by the reduction of one electron of molecular oxygen. It can also be formed through non-enzymatic electron transfer (ET) reaction where an electron is transferred to molecular oxygen, or as a result of auto-oxidation reaction [16], [24], [26].

$O_2^{-\bullet}$ does not have the ability to easily cross lipid membranes and it has relatively low reactivity with biological molecules. The half-live of this radical is about 10^{-6} seconds, and in the biological environment can act as an oxidizing or a reducing agent [24], [26]. Moreover, $O_2^{-\bullet}$ is known as producing toxic effects on biological molecules via direct reaction or by an indirect effect through the production of other ROS such as hydrogen peroxide [16], [23], [24], [26].

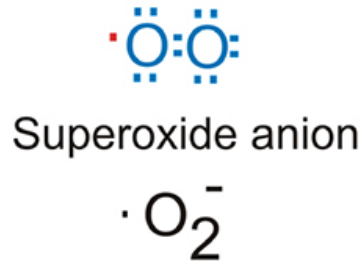

Figure 2.12 – Representation of superoxide radicals with the unpaired electron represented in red [32].

2.2.2.4. Hydrogen peroxide

Hydrogen peroxide (H_2O_2; Figure 2.13**Erro! A origem da referência não foi encontrada.**) is known for being a strong oxidiser, which reacts moderately with biological molecules due to its long half-life (minutes) [23], [26], [33]. One of the main reasons why H_2O_2 is an important molecule to consider in oxidising effects is due to its high capacity to diffuse through hydrophobic cellular membranes, being directly compared to the diffusion rate of water [23], [34]. This molecule is not considered a real oxygen free radical since does not have unpaired electrons but, its ability to penetrate membranes and react with redox-active transition metals increases the yield of ROS to higher levels than the ones observed for $OH^{\bullet}$ [4], [16], [23], [24].

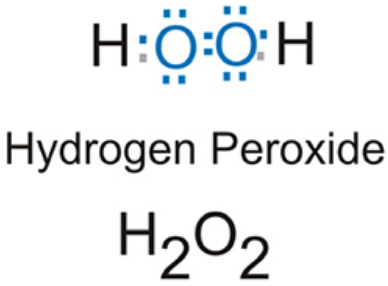

Figure 2.13 – Representation of hydrogen peroxide. Adapted from [32].

2.3. Characteristic Radical Reactions

Free radicals processes are known for their characteristic chain reactions. The basic principle behind the chain reactions of free radicals is that all molecules will try to achieve a stable

state, pairing all electrons. To accomplish the steady-state, species with unpaired electrons will scavenge one or more electron from a stable molecule in the vicinity. This event will trigger a cascade of events, that is a chain reaction, which culminates damaging the biological molecules [16], [26], [27]. These chain reactions are characterized by three distinct events namely initiation, propagation and termination. In the **initiation** reactions, the number of radical species increases and it is defined by equation [2.1] and these reactions can occur via oxidation, reduction or homolytic cleavage of a simple covalent bond (the final products of the reaction share the two electrons of the bond). Initiation reactions are usually catapulted by temperature or radiation agents [16], [23], [24].

$$\boldsymbol{A\,B} \rightarrow \boldsymbol{A^{\bullet}} + \boldsymbol{B^{\bullet}} \qquad [2.1]$$

The second phase of free radicals' reactions is the **propagation** (equation [2.2]) reactions where the number of radicals is kept constant. One molecule interacts with a free radical and originates a radical species and one stable molecule thus, the radical character of a molecule is retained or transferred to the next reaction. Although the number of free radicals remains the same before and after the reaction, it is during this phase that the majority of the free radicals are produced since they are very reactive and they will continue chasing the stable form. Propagation reactions are usually ascribed to hydrogen abstraction or addition of the radicals to double bonds [16], [23], [24].

$$\boldsymbol{AB} + \boldsymbol{A^{\bullet}} \rightarrow \boldsymbol{AA} + \boldsymbol{B^{\bullet}} \qquad [2.2]$$

The cascade reactions are ultimately halted through **termination** reactions described by equation [2.3]. As the name suggests, the number of radical species decreases through the interaction of two free radicals to form a stable molecule. It is the inverse of the initiation phase. A true termination process should be between two radical species. Non-radical ones will just retard the propagation phase since they will form free radicals of much lower reactivity [16], [23], [24].

$$\boldsymbol{A^{\bullet}} + \boldsymbol{A^{\bullet}} \rightarrow \boldsymbol{AA} \qquad [2.3]$$

2.3.1. Roles of radicals in carcinogenesis

When the biological system has an excess of ROS species it will lead to damage of several biomolecules, including proteins, lipids and DNA. The oxidative stress will increase and diseases such as diabetes mellitus, neurodegenerative diseases, rheumatoid arthritis, cataracts, cardiovascular diseases, respiratory and, ultimately, cancer will arise. Aging is also a side effect of the oxidative stress [16], [23], [24], [27], [35]. Although the pathways and molecular mechanisms by which ROS leads to carcinogenesis is still unclear, it is known that they have a role in the formation of this group of diseases. The action of oxidative stress on specific DNA regions may activate oncogenes or inactive tumour suppresser genes [27]. **Initiation** processes are attributed to the presence of free radicals that lead to permanent modification of the DNA through oxidative damage. Regarding **progression** reactions, they are related to ROS activity which stimulates uncontrolled cancer cell growth and proliferation, contributing to the cancer development.

Nonetheless, oxidative stress may also be related to prevention, treatment and recovery of cancer [36], [37]. The **prevention** is mainly due to the action of the antioxidants species as well as the **recovery** stages, and both phases will usually lead to an improvement in the quality of life of the patients. **Treatment** with radical species can occur due to their ability to damage the DNA (e.g. single and double-strand breaks) of cancer cells when combined with anticancer medicines and/or a radiation source. Since free radicals interactions can assume distinctive behaviours, it is important to mention that ROS will act as an anti-tumorigenic agent or promote tumour cell survival depending on their location, concentration, and the types of cell and tissue [36].

2.4. Radiosensitization

There is a long-term effort to improve further the outcome of cancer radiotherapy, increasing the efficacy of radiation delivery onto ailing cells, sparing healthy ones as much as possible.

This had led to the development and study of molecules with radiosensitising properties, which is an agent with the ability to enhance the radiosensitivity of tumour cells. The development of nanotechnologies and with them new nanomaterials has demonstrated that some nanoparticles (NPs) can be used as radiosensitisers [38].

2.5. Noble metal nanoparticles

Noble metal nanoparticles are used in a wide range of applications, from materials science, analytical chemistry, biomedicine and engineering high-speed circuits. The main reason of interest that lead to the increasing demand in the research and applications is related to the unique optical proprieties of metal nanoparticles (NPs) also known as localized surface plasmon resonance (LSPR). LSPR can be described as the oscillation of the conduction electrons that characteristically occurs in the visible to near-IR region of the spectrum which can be easily studied with common laboratory equipment (e.g. UV-Vis spectrophotometer) [39], [40]. Thus, NPs show a broad absorption band in the visible region of the electromagnetic spectrum [41]. The arising interest in nanomaterials among different areas of knowledge, namely in nanoparticles (NPs), is related to their different proprieties and behaviours when exposed to light and radiation [39]. Several studies have shown their unique optical proprieties, leading to an interest in increasing the knowledge in the localized surface plasmon resonance (LSPR). This phenomenon is characterized by the collective oscillation of the transferred electrons that generally occurs in the visible region of the spectrum to near UV [39], [41]. Among the noble metal nanoparticles, the ones produced from gold are most commonly used in different areas such as medicine, physics, chemistry, biology, materials science, cancer therapy, etc.

2.5.1. Gold nanoparticles

The red-purple colour observed in solutions of spherical gold nanoparticles (AuNPs) is attributed to the confinement of the electric field within a small metallic sphere (the radius

of the nanoparticles is much smaller when compared with the wavelength) and the phenomena named LPSR, as described above. It is also known that the colour of the solutions suffers slightly alterations when the AuNPs assume different shapes (Figure 2.14) or the surrounding medium is altered. In both cases, the modification of the colour is due to the optical resonance of the AuNPs. Moreover, when this resonance is excited by light one can observe a strong enhancement of the electric field leading to absorption of part of the energy of the light source and local heating of the NPs, revealing the nonlinear optical proprieties of AuNPs [42]–[44].

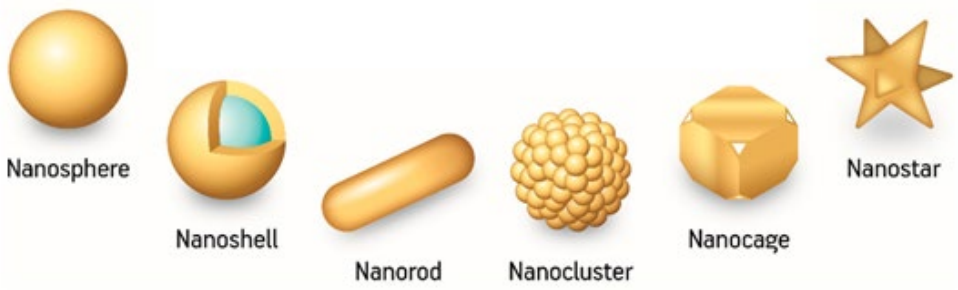

Figure 2.14 – Illustration of the different types of gold nanoparticles assemblies and morphologies used. Adapted from [44].

2.5.2. Surface plasmon resonance

There are two major concepts concerning the optical properties of nanoparticles related to their size, geometry and composition. **LSPR**, describing the oscillation of the conduction electrons in a metallic nanoparticle (Figure 2.15) and the **surface plasmon resonance (SPR)** which corresponds to the resonant oscillation of conduction electrons at the interface between negative and positive permittivity material stimulated by incident radiation or, in other words, when an electromagnetic field is applied with a specific wavelength to the surface of metallic nanoparticles it creates collective oscillations of the electrons present at their surface [44], [45]. In both cases, the magnitude, peak wavelength and spectral bandwidth of the plasmon resonance are dependent on the particle's size, shape, and composition, as well as its local dielectric environment [46].

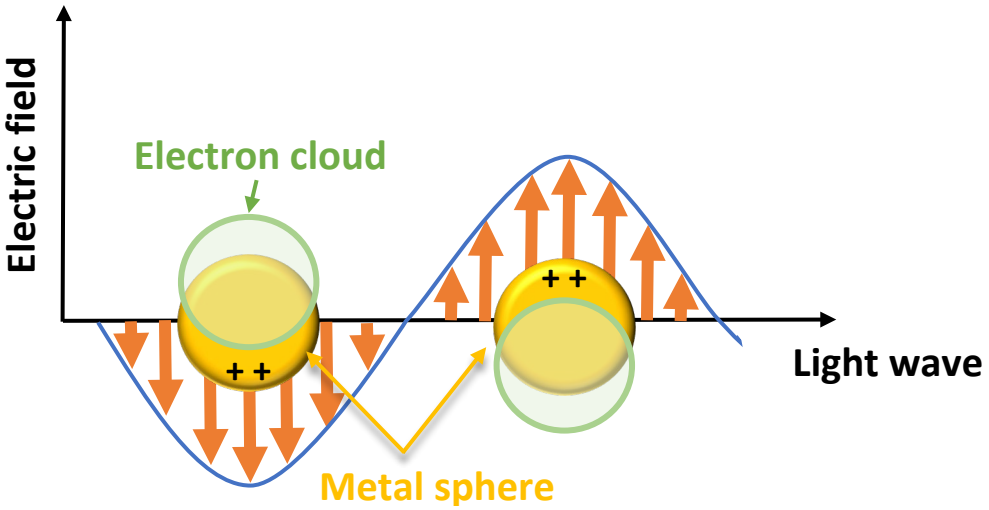

Figure 2.15 – Representation of the excitation of the localized surface plasmon resonance. Adapted from [47].

One of the very interesting characteristics of the AuNPs that is of direct use in medicine is that they behave as nanolenses since one can observe a significant enhancement of the electromagnetic field near the NP surface that rapidly decreases with distance. But it is important to mention that only when the light has the frequency to excite the oscillation of the AuNP the resonance will occur [41], [47]–[49]. Thus, two physical effects help to understand the AuNPs LSPR, one is the nanolenses effect explained above and the other is related to the maximum optical extinction at the SPR frequency, occurring at visible-near infrared wavelengths where the extinction cross-section can be much larger than their geometrical size [49], [50]. As discussed before, the plasmon resonance of metal NPs is dependent on the size, shape and composition and some differences can be observed in Figure 2.16. Silver nanoparticles exhibit a plasmon resonance around 400 nm whereas spherical AuNPs have their resonance around 520 nm. Special shaped AuNPs exhibit plasmon resonance at longer wavelengths. A higher LSPR factor representing a sharper resonance is often desirable as it leads to higher optical extinction and stronger local-field enhancement [51], [52].

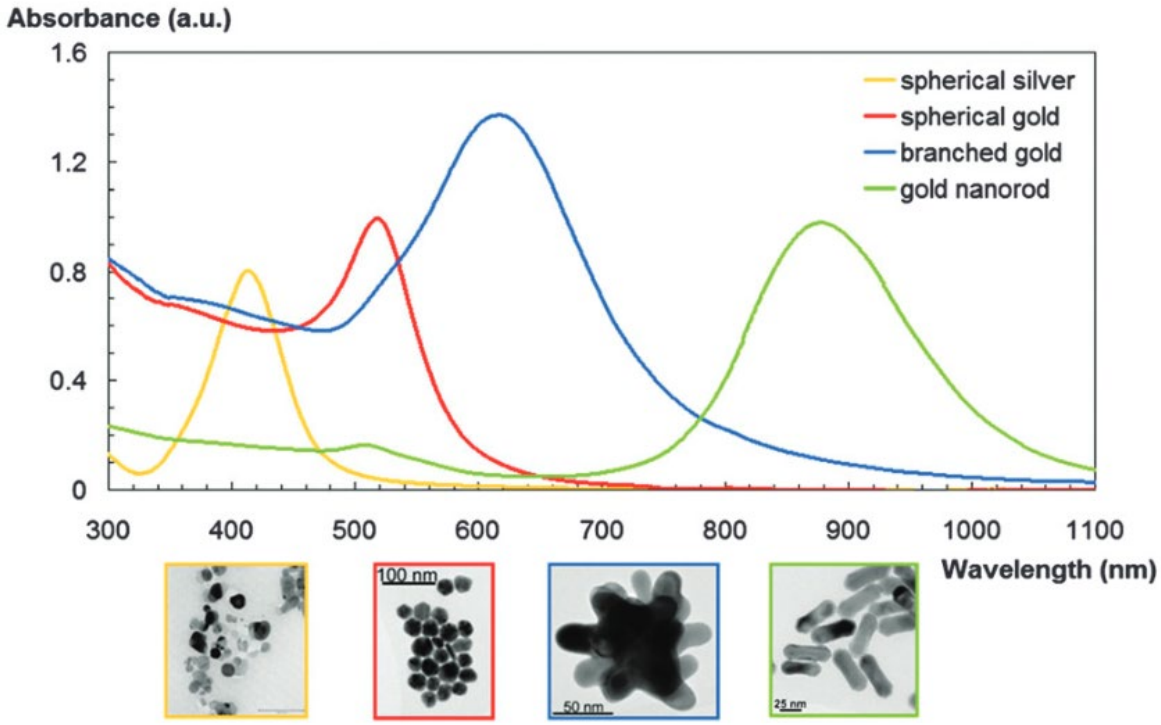

Figure 2.16 – Gold nanoparticle shape dependent LSPR as indicated by the visual appearance and UV-Vis spectra of spherical, branched and rod silver and gold nanoparticles. Adopted from [51].

One other aspect extremely important in defining the properties of NPs is the capping agent and the surrounding environment of the NPs, which can change the LSPR of the metal [50], [52]. Small AuNPs present higher absorbance cross-sections (larger NPs reveal higher scattering) leading to an increase in their efficiency when acting as nano-heaters, in other words, increasing the temperature in the vicinity of the illuminated AuNPs due to their strong optical absorption and subsequent non-radiative energy dissipation. This capability has been exploited in the application of AuNPs for plasmonic photothermal therapy [52].

2.5.3. Nanoparticle heating

Temperature is one of the characteristics that allowed the success of the use of nanoparticles in photothermal therapy. During their exposure to light, metals can convert the energy of the photons absorbed into heat, which will lead to damage in the nearby tissue. The heating

ability of the AuNPs improves the chance of success in photothermal therapy since it allows AuNPs to be heated *in vivo* [52]. The efficiency of the heating is related to the irradiation source and conditions [53], [54].

It is possible to quantify the heat generated by the nanoparticles through the calculation of the heat generated by all the NPs in the solution (equation [2.4]), and this concept is described as specific absorption rate (SAR, $W.m^{-3}$):

$$SAR = N.C_{abs}.I \quad [2.4]$$

The C_{abs} (from the optical properties) depends on the nanoparticle shape and the laser fluence I ($W.m^{-2}$) can be calculated from the laser specifications, such as the beam diameter and the power of the pulses. N represents the number of AuNPs present in the solution/tissue [54].

2.6. Photothermal therapy

The eradication of tumour cells by increasing its temperature is a technique applied for at least a century. The novelty of the photothermal therapy relies on raising the temperature only where the tumour is placed, preventing the damage of the surrounding healthy tissues. To achieve this goal, nanoparticles, namely AuNPs, have been used to help to deliver energy to targeted tumours on a very short time scale [52]. AuNPs, independent of the shape and size chosen for the success of a treatment, present characteristics that favour their application such as: easy preparation; tunable optical properties; ready multi-functionalization; solutions ready to use in an aqueous medium (avoiding the problems with organic solvents in the patient) and gold is more chemically inert when compared with other metals, which increases the biocompatibility of AuNPs. Studies of short-term exposure suggest AuNPs are non-cytotoxic at clinically relevant concentrations. It is important to mention that in some tumours the photothermal treatment is conjugated with conventional cancer treatments to enhance the destruction of the tumour cells [50], [52], [55], [56].

2.7. Dissociative electron attachment

Dissociative electron attachment (DEA) is a resonant process by which low-energy electrons (LEEs), colliding with a molecule, lead to the dissociation of the molecule producing a neutral and an anionic fragment. DEA is a low energy process, constrained to electron energies below 15 eV, and occurs in LEEs collisions with most common biological molecules including the nucleobases and amino acids [57]–[61]. Sanche and co-workers in 2000 demonstrated how DEA of the constituent molecules of DNA can lead to rupture of DNA itself [62], revolutionizing our understanding of the role of low energy, secondary electrons produced by ionizing radiation in DNA damage. DEA has very specific dissociation pathways which may allow site specific fragmentation, a phenomena that can be utilised cancer therapy [59], [63]. For example several radiosensitisers can be utilised in cancer therapy, such as 5-bromouracil and 5-fluorouracil, have high DEA cross sections and thus may enhance DNA damage if they are present in an irradiated tumour cell. Recently gold nanoparticles have been suggested, and trialled, to enhance tumour cell death, with the knowledge they are a good source of secondary electrons during irradiation with the capability to induce damage of the tumour cell DNA [59], [61], [63].

2.8. Final remarks

In this chapter, the main concepts necessary to understand the relevance of this study were presented as well as an explanation for the adoption of NPs in the development of new technologies for cancer treatment associated. In Chapter 3, the methods used in this study to better understand the effects of the laser illumination in the AuNPs and DNA response will be presented.

2.9. References

[1] J. Watson and F. Crick, “Molecular structure of deoxypentose,” *Nature*, vol. 171, pp. 738–740, 1953.

[2] S. Carter and L. Lumen, “Introduction to Nucleic Acids,” *Lumen Learning*. [Online]. Available: https://courses.lumenlearning.com/wmopen-nmbiology1/chapter/nucleic-acids/. [Accessed: 10-May-2020].

[3] R. Mintel and A. L. Lehninger, *Updated Biochemistry Text Recommended*, 7th ed., vol. 33, no. 8. 1983.

[4] M. M. Greenberg, “Reactivity of Nucleic Acid Radicals,” *Adv. Phys. Org. Chem.*, vol. 50, pp. 119–202, 2016.

[5] F. H. Stephenson, “Nucleic Acid Quantification,” in *Calculations for Molecular Biology and Biotechnology*, Elsevier, 2016, pp. 97–129.

[6] F. Pu, J. Ren, and X. Qu, “Nucleobases, nucleosides, and nucleotides: Versatile biomolecules for generating functional nanomaterials,” *Chemical Society Reviews*, vol. 47, no. 4. Royal Society of Chemistry, pp. 1285–1306, 21-Feb-2018.

[7] R. G. Endres, D. L. Cox, and R. R. P. Singh, “Colloquium: The quest for high-conductance DNA,” *Reviews of Modern Physics*, vol. 76, no. 1. American Physical Society, pp. 195–214, 12-Jan-2004.

[8] P. J. Gomes, M. Coelho, M. Dionísio, P. António Ribeiro, and M. Raposo, “Probing radiation damage by alternated current conductivity as a method to characterize electron hopping conduction in DNA molecules,” *Appl. Phys. Lett.*, vol. 101, no. 12, 2012.

[9] P. J. Gomes, A. M. Ferraria, A. M. Botelho Do Rego, S. V. Hoffmann, P. A. Ribeiro, and M. Raposo, “Energy thresholds of DNA damage induced by UV radiation: An XPS study,” *J. Phys. Chem. B*, vol. 119, no. 17, pp. 5404–5411, Apr. 2015.

[10] Z. Francis and A. Stypczynska, “Clustering algorithms in radiobiology and DNA damage quantification Geant4-DNA View project,” 2013.

[11] J. Jagger, *Introduction to Research in Ultraviolet Photobiology*. New Jersey, United States: Prentice Hall, 1967.

[12] M. Barbatti, A. J. A. Aquino, and H. Lischka, “The UV absorption of nucleobases: Semi-classical ab initio spectra simulations,” *Phys. Chem. Chem. Phys.*, vol. 12, no. 19, pp. 4959–4967, 2010.

[13] M. Raposo *et al.*, “DNA damage induced by carbon ions (C3+) beam accessed by independent component analysis of infrared spectra,” *Int. J. Radiat. Biol.*, vol. 90, no. 5, pp. 344–350, 2014.

[14] P. J. Gomes, P. A. Ribeiro, D. Shaw, N. J. Mason, and M. Raposo, “UV degradation of deoxyribonucleic acid,” *Polym. Degrad. Stab.*, vol. 94, no. 12, pp. 2134–2141, 2009.

[15] P. J. Gomes, A. M. P. S. Gonçalves Da Silva, P. A. Ribeiro, O. N. Oliveira, and M. Raposo, “Radiation damage on Langmuir monolayers of the anionic 1.2-dipalmitoyl-sn-glycero-3-[phospho-rac-(1-glycerol)] (sodium salt)(DPPG) phospholipid at the air-DNA solution interface,” *Mater. Sci. Eng. C*, vol. 58, pp. 576–579, Jan. 2016.

[16] C. von Sonntag, *Free-Radical-Induced DNA Damage and Its Repair*. 2006.

[17] Y. Polosina, “DNA Repair,” in *Reference Module in Biomedical Sciences*, Elsevier, 2014.

[18] T. M. da F. Cunha, “Negative ion formation in alkali-atom-molecule collisions,” Faculdade de Ciências e Tecnologia, Universidade Nova de Lisboa, 2018.

[19] E. I. Obeagu, “A Review on Free Radicals and Antioxidants,” *Int. J. Curr. Res. Med. Sci.*, vol. 4, no. 2, pp. 123–133, 2018.

[20] V. I. Lushchak, “FREE RADICALS, REACTIVE OXYGEN SPECIES, OXIDATIVE STRESSES AND THEIR CLASSIFICATIONS.,” *Ukr. Biochem. J.*, 2010.

[21] K. S. Gates, “The Chemical Reactions of DNA Damage and Degradation,” in *Reviews of*

Reactive Intermediate Chemistry, R. A. M. Matthew S. Platz and J. Maitland Jones, Eds. John Wiley & Sons, Inc., 2007.

[22] R. Augustine, A. P. Mathew, and A. Sosnik, "Metal Oxide Nanoparticles as Versatile Therapeutic Agents Modulating Cell Signaling Pathways: Linking Nanotechnology with Molecular Medicine," *Applied Materials Today*, vol. 7. Elsevier Ltd, pp. 91–103, 01-Jun-2017.

[23] J. P. Kehrer and L. O. Klotz, "Free radicals and related reactive species as mediators of tissue injury and disease: Implications for Health," *Crit. Rev. Toxicol.*, vol. 45, no. 9, pp. 765–798, Oct. 2015.

[24] V. M. Tandon, B. M. M. Gupta, and R. M. Tandon, "Free Radicals/Reactive Oxygen Species," *JK-Practitioner*, vol. 12, no. 3, pp. 143–148, 2005.

[25] M. Trinh, "Space, and Man's Biggest Obstacle from Exploring It." [Online]. Available: https://medium.com/@trinh.orszag/space-and-mans-biggest-obstacle-from-exploring-it-34294acb0469. [Accessed: 13-Dec-2019].

[26] A. Phaniendra, D. B. Jestadi, and L. Periyasamy, "Free Radicals: Properties, Sources, Targets, and Their Implication in Various Diseases," *Indian J. Clin. Biochem.*, vol. 30, no. 1, pp. 11–26, Jan. 2015.

[27] J. P. Kehrer, J. D. Robertson, and C. V. Smith, "Free radicals and reactive oxygen species," in *Comprehensive Toxicology: Second Edition*, vol. 1–14, Elsevier Inc., 2010, pp. 277–307.

[28] M. Dizdaroglu and P. Jaruga, "Mechanisms of free radical-induced damage to DNA," *Free Radic. Res.*, vol. 46, no. 4, pp. 382–419, Apr. 2012.

[29] L. Capaldo and D. Ravelli, "Hydrogen Atom Transfer (HAT): A Versatile Strategy for Substrate Activation in Photocatalyzed Organic Synthesis," *European J. Org. Chem.*, vol. 2017, no. 15, pp. 2056–2071, Apr. 2017.

[30] G. Louit *et al.*, "The reaction of coumarin with the OH radical revisited: hydroxylation

product analysis determined by fluorescence and chromatography," *Radiat. Phys. Chem.*, vol. 72, no. 2–3, pp. 119–124, Feb. 2005.

[31] H. Ariga and S. M. M. Iguchi-Ariga, Eds., *Advances in Experimental Medicine and Biology*, vol. 1037. Singapore: Springer Singapore, 2017.

[32] Philip Lee Miller, "Iron Therapy and Oxidative Free Radicals - Part III," 2018. [Online]. Available: https://blog.antiaging.com/iron-oxygenation-free-radicals/. [Accessed: 13-Dec-2019].

[33] D. R. de Andrade Jr, R. Becco de Souza, S. Alves Dos Santos, and D. R. de Andrade, "Oxygen free radicals and pulmonary disease," *J Bras Pneumol*, vol. 31, no. 1, pp. 60–68, 2005.

[34] C. A. McQueen and D. L. Eaton, Eds., *Comprehensive Toxicology - General Principles*, Third. Tuscon: Elsevier, 2017.

[35] A. G. Siraki, L.-O. Klotz, and J. P. Kehrer, "Free Radicals and Reactive Oxygen Species," in *Comprehensive Toxicology*, Elsevier, 2018, pp. 262–294.

[36] A. Shrivastava, L. Mohan Aggarwal, S. Pratap Mishra, H. Dev Khanna, U. Pratap Shahi, and S. Pradhan, "Free radicals and antioxidants in normal versus cancerous cells-An overview," 2019.

[37] M. R. Clemens, "Free radicals in chemical carcinogenesis," *Klin. Wochenschr.*, vol. 69, no. 21–23, pp. 1123–1134, Dec. 1991.

[38] H. Wang, X. Mu, H. He, and X.-D. Zhang, "Cancer Radiosensitizers," *Trends Pharmacol. Sci.*, vol. 39, no. 1, pp. 24–48, 2018.

[39] G. V. Hartland, "Optical studies of dynamics in noble metal nanostructures," *Chemical Reviews*, vol. 111, no. 6. pp. 3858–3887, 08-Jun-2011.

[40] I. Capek, "Noble Metal Nanoparticles," 2017, pp. 125–210.

[41] I. Khan, K. Saeed, and I. Khan, "Nanoparticles: Properties, applications and toxicities,"

Arabian Journal of Chemistry, vol. 12, no. 7. Elsevier B.V., pp. 908–931, 01-Nov-2019.

[42] E. C. Dreaden, A. M. Alkilany, X. Huang, C. J. Murphy, and M. A. El-Sayed, "The golden age: Gold nanoparticles for biomedicine," *Chemical Society Reviews*, vol. 41, no. 7. pp. 2740–2779, 07-Apr-2012.

[43] C. Louis and O. Pluchery, *Gold Nanoparticles for Physics, Chemistry and Biology*. 2012.

[44] L. Freitas de Freitas, G. Varca, J. dos Santos Batista, and A. Benévolo Lugão, "An Overview of the Synthesis of Gold Nanoparticles Using Radiation Technologies," *Nanomaterials*, vol. 8, no. 11, p. 939, Nov. 2018.

[45] Y. Chen *et al.*, "Two-Dimensional Metal Nanomaterials: Synthesis, Properties, and Applications," *Chemical Reviews*, vol. 118, no. 13. American Chemical Society, pp. 6409–6455, 11-Jul-2018.

[46] X. Guo, "Surface plasmon resonance based biosensor technique: A review," *J. Biophotonics*, vol. 5, no. 7, pp. 483–501, 2012.

[47] J. Jana, M. Ganguly, and T. Pal, "Enlightening surface plasmon resonance effect of metal nanoparticles for practical spectroscopic application," *RSC Advances*, vol. 6, no. 89. Royal Society of Chemistry, pp. 86174–86211, 08-Sep-2016.

[48] "Gold Nanoparticle Properties - Cytodiagnostics." [Online]. Available: http://www.cytodiagnostics.com/store/pc/viewcontent.asp?idpage=2. [Accessed: 16-Dec-2019].

[49] V. Amendola, R. Pilot, M. Frasconi, O. M. Maragò, and M. A. Iatì, "Surface plasmon resonance in gold nanoparticles: A review," *Journal of Physics Condensed Matter*, vol. 29, no. 20. Institute of Physics Publishing, 20-Apr-2017.

[50] K. Kołątaj, J. Krajczewski, and A. Kudelski, "Plasmonic nanoparticles for environmental analysis," *Environmental Chemistry Letters*, vol. 18, no. 3. Springer, pp. 529–542, 01-May-2020.

[51] H. Jans and Q. Huo, “Gold nanoparticle-enabled biological and chemical detection and analysis,” *Chem. Soc. Rev.*, vol. 41, no. 7, pp. 2849–2866, Mar. 2012.

[52] N. S. Abadeer and C. J. Murphy, “Recent progress in cancer thermal therapy using gold nanoparticles,” *J. Phys. Chem. C*, vol. 120, no. 9. American Chemical Society, pp. 4691–4716, 10-Mar-2016.

[53] L. De Sio *et al.*, “Photo-thermal effects in gold nanorods/DNA complexes,” *Micro Nano Syst. Lett.*, vol. 3, no. 1, pp. 0–8, 2015.

[54] Z. Qin and J. C. Bischof, “Thermophysical and biological responses of gold nanoparticle laser heating,” *Chem. Soc.*, vol. 41, no. 3. pp. 1191–1217, 07-Feb-2012.

[55] X. Huang, P. K. Jain, I. H. El-Sayed, and M. A. El-Sayed, “Plasmonic photothermal therapy (PPTT) using gold nanoparticles,” *Lasers Med. Sci.*, vol. 23, no. 3, pp. 217–228, 2008.

[56] J. Nam, S. Son, L. J. Ochyl, R. Kuai, A. Schwendeman, and J. J. Moon, “Chemo-photothermal therapy combination elicits anti-tumor immunity against advanced metastatic cancer,” *Nat. Commun.*, vol. 9, no. 1, pp. 1–13, Dec. 2018.

[57] I. I. Fabrikant, “Theory of dissociative electron attachment: Biomolecules and clusters,” *EPJ Web Conf.*, vol. 84, Jan. 2015.

[58] H. Yadav, M. Vinodkumar, and C. Limbachiya, “A dissociative electron attachment cross-section estimator Related content Study of electron impact inelastic scattering of chlorine molecule (Cl 2),” *J. Phys. Conf. Ser*, vol. 388, p. 12013, 2012.

[59] I. I. Fabrikant, S. Eden, N. J. Mason, and J. Fedor, “Recent Progress in Dissociative Electron Attachment: From Diatomics to Biomolecules,” *Adv. At. Mol. Opt. Phys.*, vol. 66, pp. 545–657, Jan. 2017.

[60] S. Ptasińska and L. Sanche, “Dissociative electron attachment to hydrated single DNA strands,” *Phys. Rev. E*, vol. 75, no. 3, p. 031915, Mar. 2007.

[61] M. A. Śmiałek, “Evaluating experimental molecular physics studies of radiation damage

in DNA" *Eur. Phys. J. D*, vol. 70, no. 11, 2016.

[62] B. Boudaïffa, P. Cloutier, D. Hunting, M. A. Huels, and L. Sanche, "Resonant formation of DNA strand breaks by low-energy (3 to 20 eV) electrons," *Science (80)*, vol. 287, no. 5458, pp. 1658–1660, Mar. 2000.

[63] S. E. Huber, M. A. Śmiałek, K. Tanzer, and S. Denifl, "Dissociative electron attachment to the radiosensitizing chemotherapeutic agent hydroxyurea," *J. Chem. Phys.*, vol. 144, no. 22, Jun. 2016.

Chapter 3

Materials and Methods

Materials and Methods

This chapter describes the experimental procedures used to analyse the effect of radiation on deoxyribonucleic acid (DNA) and nucleobases and the techniques employed to characterize these samples.

3.1. Experimental setup

In the present study we have used two different sources of irradiation, an ultra-violet (UV) lamp and a Neodymium-doped Yttrium Aluminium Garnet (Nd:YAG) pulsed laser, these are each described below.

3.1.1. Ultra-Violet irradiation

Calf thymus DNA solutions (section 3.4) were irradiated for different periods of time by means of a 254 nm UVC germicide lamp, model TUV PL-L 55W/4P HF 1CT from Philips®, at an irradiance of 1.9W/m^2, in a ventilated chamber at room conditions.

3.1.2. Laser irradiation

Nanosecond (ns) pulses generated with a Minilite I Nd:YAG laser from Continuum were used to irradiate samples of the nucleobases (section 3.3), and the solutions of DNA (section 3.4). Aqueous samples with the analytes in study were irradiated in the presence and absence of AuNPs. The second harmonic of the laser was used with a wavelength of 532 nm, with a pulse length ranging from 3 to 5 ns. The energy was tuned to 16 mJ per pulse. The repetition rate chosen was 15 Hz and in Table 3.1 we present the diameter of the focused laser beam at

different distances from the focal lens to the irradiated solution. The fluence was determined using $\boldsymbol{Fluence}$=$\boldsymbol{Energy}$ per pulseBeam area × pulse length (W/m^2)

[**3.1**]:

$$\boldsymbol{Fluence} = \frac{\boldsymbol{Energy\ per\ pulse}}{\boldsymbol{Beam\ area \times pulse\ length}}\ (\boldsymbol{W/m^2}) \qquad [3.1]$$

where the measured energy per pulse was ≈0.240 W and the pulse length used was 5 ns. The size of the focused laser beam was determined with a Vernier calliper and from photographic paper irradiated with a single laser shot.

Table 3.1 – List of laser beam diameter and fluence varying with focal distance.

Focus distance (mm)	Beam diameter (mm)	Laser fluence (W/m^2)
0	0.35	4.99×10^{14}
1	0.49	2.55×10^{14}
2	0.58	1.82×10^{14}
3.5	0.78	1.00×10^{14}
5	0.96	6.63×10^{13}
8	1.61	2.36×10^{13}
10	1.98	1.56×10^{13}

The experimental setup used in this work is presented in Figure 3.1 and was assembled according to the setup reported by Ilko Bald and co-workers [1] allowing direct comparison of results. The laser beam is widened to the point where it reaches the sample by a set of two lenses from a diameter of 3 mm to 9 mm. Subsequently the beam is guided by a dichroic mirror to a further lens (*f = 5 cm*) and focused into a 3.5 mL quartz cuvette slightly above the surface of the solution in study. The cuvette, filled with 2 mL of solution, is placed on a stirring plate to continuously stir the solution during the irradiation. The distance of the laser focus to the surface of the irradiated solution was varied using a mechanical stage, in order to adjust the beam diameter size and in consequence the altered the laser fluence (see Table 3.1) of the divergent beam on the surface. The laser fluence, given in Table 3.1, refers to the maximum laser fluence at the surface without correction for the beam widening as it passes the cuvette towards the bottom. All samples were irradiated with the procedure described above.

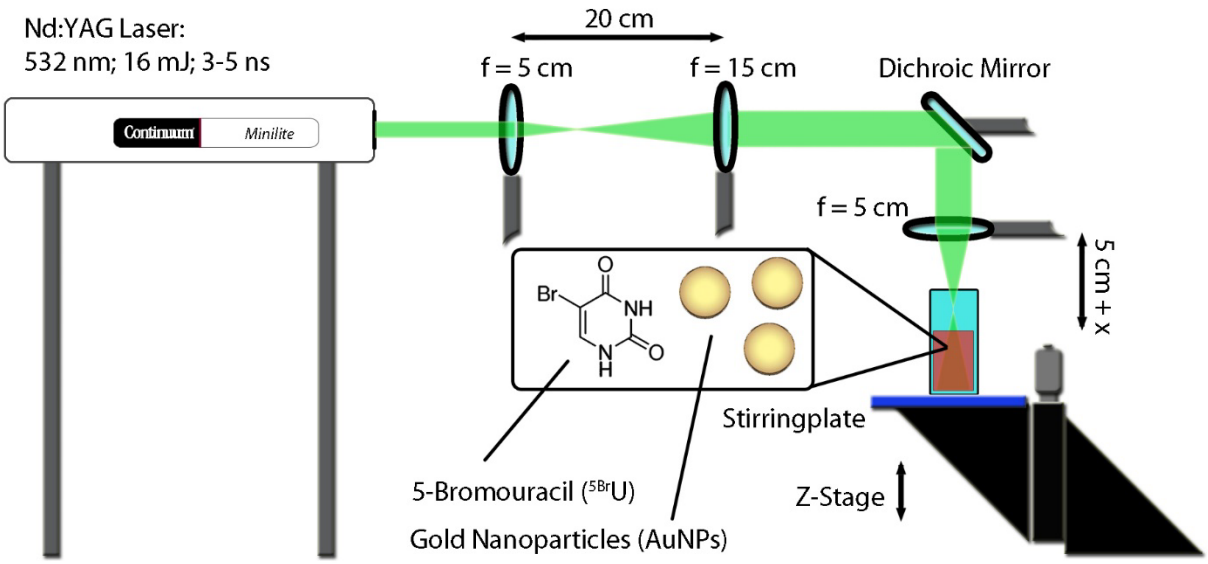

Figure 3.1 – Schematic representation of the experimental setup.

3.2. Sample preparation

The protocol for the preparation of the samples was based on the dilution of the analyte in ultra-high purity water (UHPW). Different concentrations were used for each compound and are presented in the chapters 4, 5, 6 and 7, where we discuss the results. The final volume of the solutions prepared was always 2 mL placed in a cuvette of high performance quartz glass from Hellma®. In the solutions irradiated in the presence of gold nanoparticles (AuNPs), the aqueous solutions were prepared with UHPW, in the concentration of the analyte desired for the experiment, and the AuNPs were added in the final molar concentration of 47 pM.

The preparation and concentration of the different nucleobases and DNA solutions are explained in detail in the corresponding section.

3.3. Nucleobases

The nucleobases used in this work were uracil (U; cas 66-22-8), 5-bromouracil (^{5Br}U; cas 51-20-7) and 5-fluorouracil (^{5F}U; cas 51-21-8) and their chemical structure is presented in Figure 3.2.

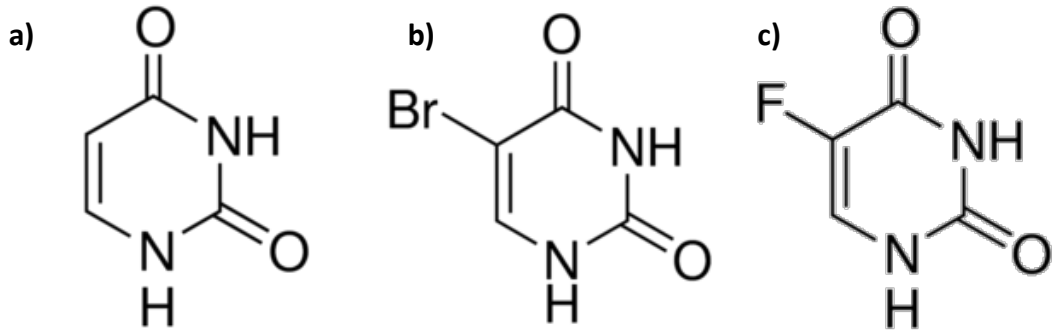

Figure 3.2 – Chemical structures of the nucleobases used in this work, a) Uracil, b) 5-Bromouracil and c) 5-Fluorouracil.

Uracil (Figure 3.2a)) presents a maximum absorption spectra at 258 nm, corresponding to the π-π^* transition [2]. In this work, we have also studied the interaction of a pulsed laser with a brominated derivative of uracil, 5-bromouracil (5BrU) with chemical formula $C_4H_3BrN_2O_2$ (Figure 3.2b)). 5BrU acts as a base analogue, replacing thymine in DNA without substantially altering the biological activity and it is known to act has a radiosensitizer which induces DNA damage due to its high reactivity with electrons at very low energies [3]–[5]. In the absorption spectra its maximum absorption is at 277 nm [2].

The last uracil derivate used in this work was 5-fluorouracil (5FU), with chemical formula $C_4H_3FN_2O_2$ (Figure 3.2c)). 5FU is a commonly drug used in the treatment of solid cancers, such as breast, head, skin, colon, stomach and head, and is an analogue of pyrimidine (uracil) [6]–[8]. Its absorption spectra shows a maximum at 266 nm. All the nucleobases solutions used in this work were prepared with UHPW and with a final concentration of 25 µM.

3.4. DNA

In the present work, two different types of DNA, calf thymus DNA and plasmid DNA have been used. The description of these molecules and proprieties are described in the following sub-sections.

3.4.1. Calf Thymus DNA

DNA extracted from the thymus of a calf, also called calf thymus DNA, is usually used as substrate for DNA polymerase assays, in the amplification of very long fragments and as a carrier DNA for precipitations. Additionally, calf thymus DNA is frequently used in studies on DNA binding and to explore damage caused by external agents. One of the main reasons for the use of this DNA type by so many researchers is the fact that it closely resembles the mammalian DNA structure. In this work, we have used calf thymus DNA (Sigma-Aldrich®) with a final concentration of 0.025 mg/mL dissolved in UHPW.

3.4.2. Plasmid DNA

By definition, a plasmid is a small DNA molecule, circular and double-stranded, with the ability of replicate autonomously in a host cell, usually from bacteria, controlling the copy number and ensuring that the genomic information is not misplaced during cell division [9], [10]. The length of a plasmid can vary from a few to several hundred of kilo base pairs (kbp) containing the genomic information essential for plasmid maintenance functions [10].

In this work, we have used plasmid DNA obtained after growing specific bacteria cultures followed by extraction and purification. The protocol involves several steps that are described in detail below. The plasmid used for the study of the effect of irradiation with a Nd:YAG pulsed laser was pBV-Luc/Del 6 (Plasmid #14969, Addgene®). The size of this plasmid is 4900 base pairs (bp), and the depositing laboratory was Joan Massague lab. pBV-Luc/Del 6 is an circular and double stranded plasmid where the c-myc promoter was inserted between the

cloning sites XhoI (which was destroyed) and PvuII (Figure 3.3). The working solutions used in this work had a final concentration of 25 mg/mL prepared with UHPW.

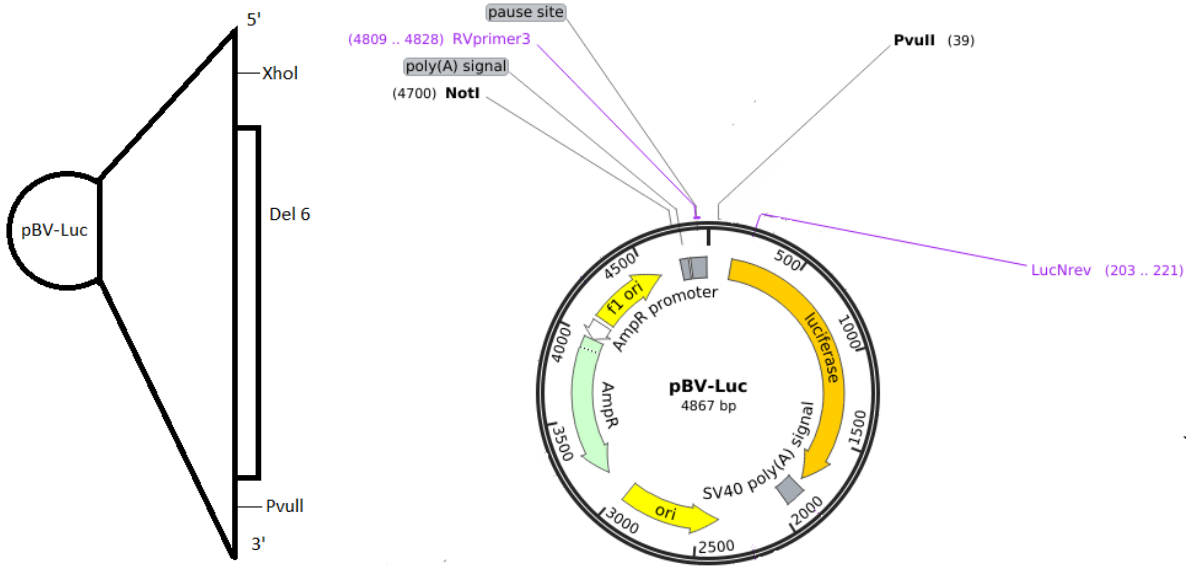

Figure 3.3 – pBV-Luc/Del 6 plasmid map representation and schematic view of the insertion Del 6 [11].

3.5. Gold nanoparticles

Gold nanoparticles (AuNPs) were used as bought from BBI Solutions (United Kingdom), and were in a suspension consisting of sub-micron AuNPs suspended in water, with citrate as capping agent to maintain the stability of the AuNPs and avoid their coalescence. BBI's measurements show that the mean diameter of the AuNPs is between 37.0 and 43.0 nm with a number of odd shapes per 100 particles ≤ 5, with a coefficient of variation ≤ 8% regarding the size and shape of the nanoparticles (NPs). The diameter assumed in all the experiments was 40 nm. The solution was bought as a concentration of 9.00×10^{10} particles/mL and a molar concentration of $2.96 \times 10^{-4}\, mol\ of\ gold/L$. After dilution with UHPW, the final molar concentration of AuNPs in the solutions to be used in the irradiation experiments was 47 pM.

3.6. Fluorescent Probes

By definition, free radicals are atoms or molecules with a short life time, unstable and highly reactive since they contain unpaired electrons in the valence shell or in the outer orbit, and they can cause damage to proteins, DNA and cell membranes by subtracting their electrons through an oxidation process [12], [13]. The molecule that suffers the attack itself becomes a free radical leading to a chain reaction cascade that ends damaging the molecule or cell. The free radical presents the ability of existing independently and the simplest free radical is an atom of hydrogen, with one proton and a single electron represented by $H^{\bullet}$ [13], [14]. In the present study, free radicals are formed during water radiolysis and play an important role in DNA damage processes. These processes are part of the indirect effects of radiation in the biological damage of DNA.

3.6.1. Coumarin-3-carboxylic acid

Coumarin-3-carboxylic acid (3-CCA) is an aromatic organic chemical compound produced in plants and it is non-fluorescent in water [15]. The 3-CCA method was developed based on the hydroxylation of this compound by $OH^{\bullet}$, were the reaction produces 7-hydroxycoumarin-3-carboxylic acid (7-OHCCA, see Figure 3.4) that presents high fluorescent and the intensity of fluorescence is proportional to the number of 7-OHCCA molecules in the solution [16].

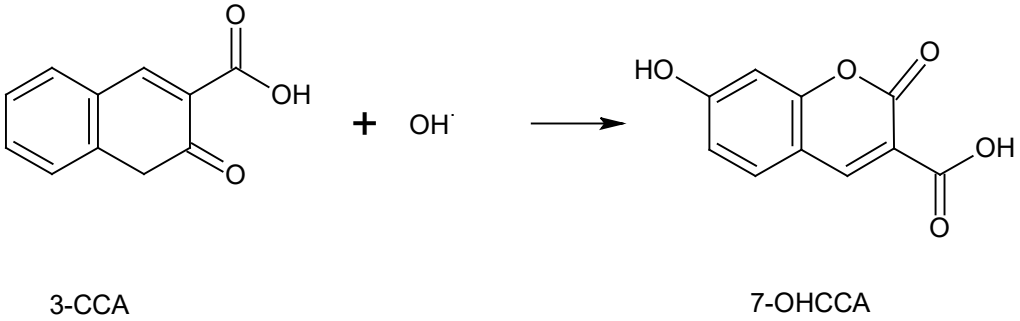

Figure 3.4 – Representation of 3-CCA hydroxylation and the major fluorescent product 7-OHCCA.

7-OHCCA has excitation bands at 320-370 nm and 380-400 nm and emission with maximum at 450 nm. The $OH^{\bullet}$ attacks the aromatic ring of the coumarin after the exposure to a radiation

source and the resulting molecule 7-OHCCA remains in the reaction mixture following stabilisation of the chemical system, making its analysis and detection easier [15]–[18]. Yamashita and co-workers (2012) have reported that 3-CCA is suitable for measuring $OH^{\bullet}$ yields from water radiolysis and it is generally accepted that hydroxyl radicals are one of the main species produced during these processes.

A stock solution of 3-CCA (Sigma Aldrich®) 5 mM was prepared in 3% phosphate-buffered saline (PBS) at room temperature until the 3-CCA was fully dissolved. The pH was then adjusted to 7.4 with a solution of hydrochloric acid (HCl 1 M). A calibration curve was prepared with several dilutions, in PBS, of the stock solution with steps of 0.05, 0.25, 0.5, 1.25, 2.5 and 5 mM and the fluorescence intensity was measured, in quadruplicate, with a FLUOstar OPTIMA FL - Microplate Reader from BMG LABTECH, using the emission wavelength of 450 nm, excitation of 390 nm and a gain of 1500. After deriving the calibration curve, the solutions were measured in presence and absence of AuNPs and with 3-CCA with a final concentration of 2.5 mM. The samples were irradiated with Nd:YAG pulsed laser up to 30 minutes and fluorescence intensity was measured in quadruplicate for each exposure time. Control samples were carried out in presence and absence of AuNPs.

3.6.2. Dihydrorhodamine-123

To quantify the amount of H_2O_2 (hydrogen peroxide) and its effect on DNA damage in our experiments we have chosen the probe dihydrorhodamine-123 (DHR-123) that is known to oxidise in presence of this free radical [19]. DHR-123, as 3-CCA, is a non-fluorescent compound that after oxidation originate a chemical highly fluorescent, rhodamine-123, a cationic red fluorescent dye (Figure 3.5) [20]. Rhodamine-123 presents an excitation band at 500 nm and emission wavelength at 536 nm. Although DHR-123 is oxidised by H_2O_2, it also can be oxidised by other free radicals, thus one of its disadvantages is the low specificity [20], [21].

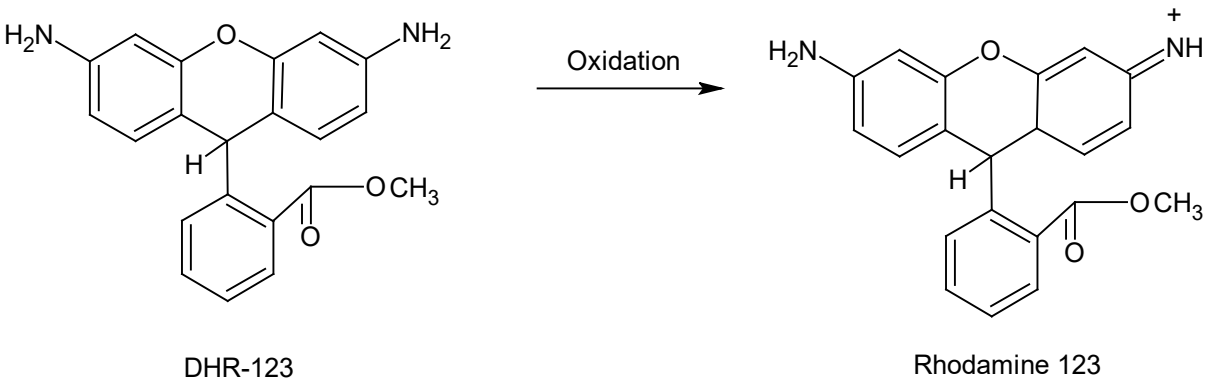

Figure 3.5 – Representation of the oxidation of dihydrorhodamine-123 and the resulting fluorescent product rhodamine-123.

According to Imbeault & Gris, 2013, one of the most accurate and reproducible methods to evaluate oxidative activity is using DHR-123 since this chemical has a low cost, large commercial availability and a high quantum yield allowing non-invasive detection and low interference with underlying metabolic processes [22]. However, it is important to recognise that above 5 mM (aqueous solution) the fluorescence deviates from linearity, and the intensity decreases at higher concentrations [22].

Stock solutions of DHR-123 (5 mM, Sigma Aldrich®) were prepared in 3% PBS at room temperature. The pH was then adjusted to 7.4 with a solution of hydrochloric acid (HCl 1 M). The fluorescence intensity was measured for the samples in both the presence and absence of AuNPs and with 2.5 mM DHR-123 (final concentration). The samples were irradiated using a Nd:YAG pulsed laser for up to 30 minutes and fluorescence intensity was measured, in quadruplicate, with a FLUOstar OPTIMA FL - Microplate Reader from BMG LABTECH, using the emission wavelength of 544 nm, excitation of 485 nm and a gain of 1500, for each exposure time. Control samples were carried-out.

3.6.3. Hydroxyl scavenger – Ethanol

Ethanol was chosen to evaluate the effect of hydroxyl radicals, as an $OH^{\bullet}$ scavenger, and the effects on the DNA molecules after laser exposure were studied. A small volume of pure ethanol was added to the irradiated solutions with AuNPs to achieve the final concentration of 5 % ethanol. After the different periods of laser light exposure (up to 30 minutes), aliquots

were placed into a 96 wells plate and the fluorescence was measured with the same equipment described above. All measurements were performed in quadruplicate and a control sample was measured too. A volume of 4 µL (plasmid solutions with EtOH) of all the periods of irradiation was loaded on a agarose gel and the bands were revealed with a UV gel doc system (G:BOX Chemi XX9 from Syngene). The results where compared with control samples irradiated for the same periods in order to evaluate the role of the $OH^{\bullet}$ radicals in the solutions.

3.7. Plasmid DNA production

For this work, batches of plasmid DNA were produced following the protocol described below.

3.7.1. Protocol for bacteria growth

Plasmid samples were prepared for irradiation with Nd:YAG pulsed laser in both the presence and absence of AuNPs. For the incubation of the bacteria, two solutions of Luria-Bertani broth (LB Broth, Sigma, L3022 - concentration of 20 g/L) were prepared. To one of the bottles 7.5 g/L of agar was added in order to have solid medium. Both solutions were autoclaved (Meadowrose scientific LTD®, serial n°1316). After sterilisation, ampicillin (Sigma, A9518, 50 µg/mL solution in UHPW) was added to the medium at a temperature below 36 °C and poured into sterile Petri dish (Cellstar, Greiner Bio-One®) to set at room temperature. It is important to note that the antibiotic was previously sterilized, passing the solution through a Terumo® syringe without needle (Terumo, SS+01T1) with a 0.45 µm pore size filter (Millex®HA, SLHA033SS) coupled. This step is very important to avoid the growth of undesired colonies. Finally, a loop of the bacteria pBV-Luc/Del6 stock solution was streaked onto plates and incubated overnight at 37 °C. The procedure described was carried in a vertical laminar airflow cabinet to avoid cross contamination.

3.7.2. Incubation, extraction and purification of DNA

Next day, single colonies of bacteria were picked for amplification. Each colony was inoculated in LB medium, containing ampicillin, for 4h at 37 °C while shaking at 100 rpm. After this time lapse, 1 mL of this solution was added to 100 mL of LB medium and incubated for 14h at 37 °C while shaking at 100 rpm, to amplify the bacteria present in the medium. The solution was then centrifuged at 6000 x g, 4 °C for 30 min. The pellet resulting from this step was air dried for at least 1 h. To extract the plasmid to make working solutions, we used the Qiagen plasmid maxi kit (Qiagen®) and followed the provided protocol [23] without further modifications. The pellet of plasmid extracted was dissolved in a small volume of nuclease-free water (Invitrogen, Thermo Scientific™) and the concentration and purity of the DNA was measured with a NanoDrop™ One Microvolume UV-Vis Spectrophotometer (Thermo Scientific™).

3.8. Characterization of DNA damage techniques

The damage caused in the DNA after laser illumination was characterized using both spectrophotometric and gel electrophoresis techniques described below.

3.8.1. Spectrophotometric measurements

Spectrophotometric measurements allow one to measure the amount of light absorbed by a substance by determining the intensity of light as a beam of light passes through sample solution. The principle is based on the fact that each compound absorbs or transmits light over a certain range of wavelength. From this method is possible to quantify the amount of a known substance.

3.8.1.1. UV-Vis absorption spectroscopy

Ultra-Violet Visible (UV-Vis) spectroscopic measurements were performed using a Thermo Scientific Evolution 201 (United Kingdom) spectrometer operating over the spectral range of 190 to 800 nm, scan speed of 200 nm/min, with a bandwidth of 1 nm and data intervals of 0.2 nm and using quartz cuvettes with a 1 cm light path. The spectra were normalized by subtracting a so-called blank sample containing the solute. All the spectra were acquired after irradiation with ns pulsed laser. UV-Vis spectra were recorded after specific illumination periods in order to determine the localized surface plasmons resonance (LSPR) of the AuNPs and the π- π* resonance of the analytes.

UV-Vis spectroscopy is also a technique used to determine DNA purity. The concentration of DNA on a sample is determined from $C = CF \times Abs_{260}$, with the conversion factor (CF) of 50 ng/µL for double-strand DNA (dsDNA), when absorbance is equal to 1 and the optical path length is 1 cm. It is also possible to determine the concentration of RNA and single-strand DNA (ssDNA) using the CF of 40 ng/µL and 33 ng/µL, respectively. This equation derives from a transformation of the Lambert-Beer law, $A = \varepsilon \times C \times l$ [24], [25]. Considering that the maximum absorption of the nucleotides, RNA, ssDNA and dsDNA is in the vicinity of 260 nm, all these molecules will contribute to the total absorbance on this region and thus mask the quantity and quality of the DNA present [25]–[27]. Therefore, ratios for the absorbance measured at 230, 260 and 280 nm are calculated. The ratio of absorption A_{260}/A_{280} is used to assess the purity of DNA or RNA and is usually accepted that values higher than 1.8 indicate pure DNA [24], [25]. As the commonly contaminants of DNA samples (for instance protein, carbohydrates or certain salts) absorb in the vicinity of 280 nm, a decrease of this ratio signals the above mentioned contamination (for values lower than 1.8) [24], [25], [27]. On the other hand, A_{260}/A_{230} ratio is a sensitive indicator of other contaminants, such as phenol, chaotropic salts and non-ionic detergents that absorb at 230 nm. Hence, values expected for this ratio are in the range of 2.3-2.4 for pure DNA with values below this range indicating sample contamination [24], [25], [27].

In this study, the concentration and purity of the extracted plasmid DNA were assessed with a Nanodrop spectrophotometer. Table 3.2 presents the measured values of the absorbance at 260 nm, 280 nm and 230 nm and the calculated DNA concentration and purity ratios. The

extraction led to pure DNA since the A_{260}/A_{280} and A_{260}/A_{230} ratios were 1.9 and 2.3, respectively, which is considered to be pure DNA and suitable for use in most downstream applications [24], [25].

Table 3.2 – Concentration and ratios obtained for the plasmid DNA extracted.

	Nucleic Acid (ng/µL)	**A_{260}/A_{280}**	**A_{260}/A_{230}**	**A_{260}**	**A_{280}**	**A_{230}**
Plasmid DNA	415	1.9	2.3	8.3	4.4	3.6

3.8.1.2. Fluorescence spectroscopy

Fluorescence is the phenomena of light emission from a molecule after its excitation with light energy or photons. Photoabsorption will raise an electron to an excited state that undergoes rapid thermal energy loss to the environment through vibrations, with a photon being emitted from the lowest-lying singlet excited state. Fluorescence typically occurs from aromatic molecules. In this study, we have investigated the fluorescence intensity of fluorogenic probes mentioned in section 3.6. after exposition to laser light up to 30 minutes, in both presence and absence of AuNPs. The equipment used for these measures was a microplate reader (BMG Labtech®, FLUOstar Optima) and the wavelengths of excitation and emission for each probe are mentioned in section 3.6, and Figure 3.6 presents the schematic operation of the spectrophotometric fluorescence equipment.

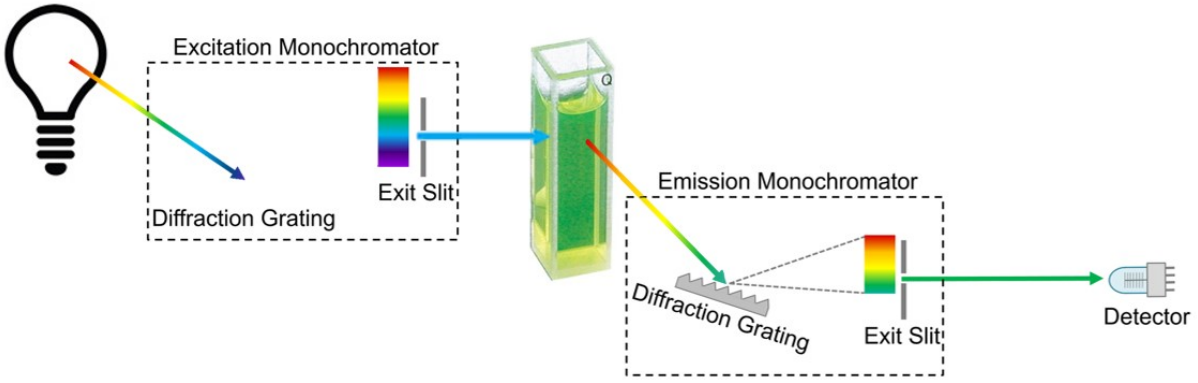

Figure 3.6 – Schematic of the measurement of fluorescence intensity. Adapted from [28]

3.8.2. Plasmid DNA in electrophoresis

The separation, identification and purification of DNA, nucleic acids or proteins can be achieved using a simple standard method of electrophoresis through agarose or polyacrylamide gels. Both types of gels are porous, the size of the pores depending on the concentration of the polymeric matrices. It is important to choose the type of electrophoresis to analyse the samples carefully considering the initial size, fragments size and type of sample in study (DNA, proteins, cells, among others). During electrophoresis, the sample is submitted to an electrical voltage, which moves the negatively charged ions towards the positive electrode and vice-versa. The separation of the analytes can be achieved since different ions migrate at different rates.

In the present work we have used agarose gel electrophoresis (AGE) to separate and analyse DNA fragments produced by Nd:YAG ns pulsed laser and the samples migrated from the negative towards the positive electrode since DNA is negatively charged due to its backbone phosphates.

3.8.2.1. Agarose Gel Electrophoresis

AGE is one of several physical methods for determining the size of DNA and the most effective method for separating the fragments with sizes ranging from 100 bp to 25 kbp. Agarose is a polysaccharide isolated from the seaweed genera *Gelidium* and *Gracilaria*, and consists of repeated agarobiose (L- and D-galactose) subunits. The molecular separation properties are determined during the gelation of the agarose where the polymers associate non-covalently and form a network of bundles leading to the formation of different pores sizes depending on agarose concentration. In this method, DNA is forced to migrate through a highly cross-linked agarose matrix in response to an electric voltage. In solution, the phosphates of the DNA are negatively charged, and the molecule will therefore migrate to the positive pole. The rate of migration of a DNA molecule through a gel is determined by the following: 1) the size of DNA molecule; 2) the agarose concentration; 3) the conformation of the DNA; 4) the

voltage applied, 5) the presence of ethidium bromide, 6) the type of agarose and 7) the electrophoresis running buffer. The scheme of typical system for AGE is shown in Figure 3.7.

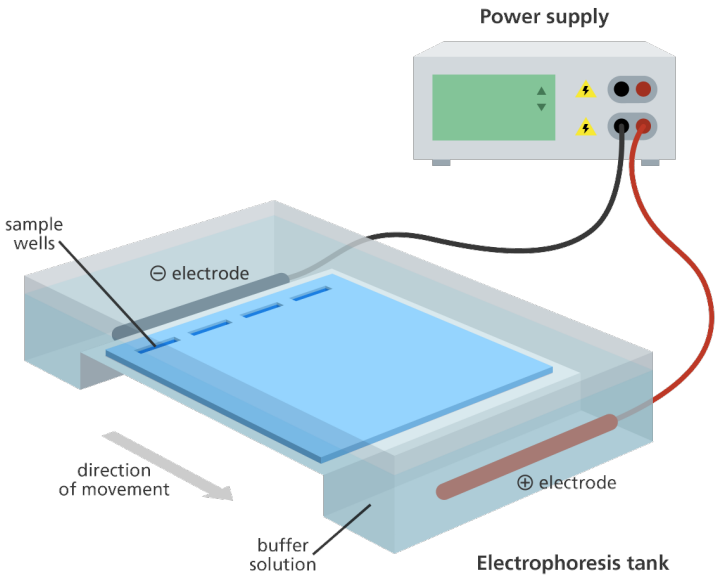

Figure 3.7 – Agarose electrophoresis system [29].

Regarding the protocol for using AGE, first the agarose gel is placed into an electrophoresis tank (wells will be on the negative part of the tank) filled with the buffer solution chosen. The second step is to load the DNA samples with the loading buffer (which ensure the sample will "sit" on the well and allow visual monitoring of the bands running) into the pre-cast wells. After this step, one should programme the power supply with the voltage required and start the run. After separation, the DNA molecules can be visualized under UV light after staining with an appropriate dye.

The AGE method has the following advantages: 1) it is simple and rapid to cast; 2) the gel medium is nontoxic; 3) it is good for separating large DNA molecules; and 4) it is possible to recover the samples. The disadvantages of this technique are: 1) the high cost of the agarose; 2) the bands can appear fuzzy and/or spread apart; and 3) for low molecular weight samples the separation yield is low [30]–[32].

3.8.2.2. Migration of plasmid DNA in agarose

Plasmid DNA usually has two or three forms when it runs on agarose gel and the fragments will migrate according to their conformation, which will correspond to the bands revealed in the gel. The first is the supercoiled form (Figure 3.8), the native conformation of DNA found *in vivo* which occurs when the double helix strand has extra twists that introduce tension to the strands. Supercoiled forms are the ones that migrate faster in the gel due to its conformation since fragments become smaller in size and hence experience less frictional resistance from the gel. It corresponds to one of the forms that we need always to visualize on the control sample in the gel, since it shows that plasmid purification was successful. The second conformation always present on the control sample after DNA extraction is the relaxed or nicked form (Figure 3.8) and it is the slowest migrating on AGE since it is a large relaxed circle, increasing the size of the fragment and frictional resistance from the gel. This relaxed conformation is formed during DNA replication. The access to the supercoiled forms for replication is not easy and the enzymes (topoisomerases) will cut one strand of the DNA helix and relax the superhelical tension. The third most common conformation of plasmid DNA is the linear (Figure 3.8) one, which appears between the two previous. Linear DNA results from the cut in both strands at the same place and it is usually related with DNA damaged, contamination or harsh treatment during the purification process [33].

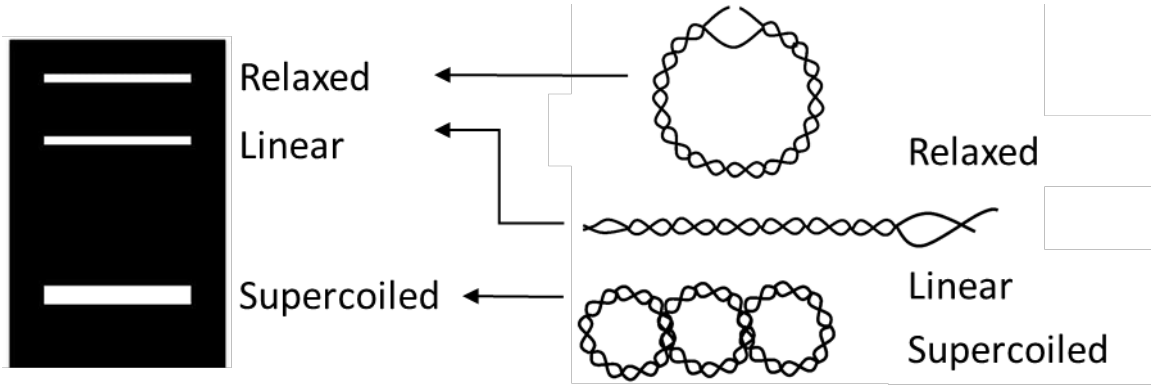

Figure 3.8 – Plasmid DNA conformations and migrations on agarose gel electrophoresis [34]–[36].

Just one break in one of the strands of DNA double helix, called as single-strand break (SSB), converts a supercoiled molecule into a relaxed one. A supercoiled (form I) DNA molecule is

converted into a relaxed circle (form II) as soon as one of the polynucleotide chains is nicked. When both strands are broken, i.e. double-strand break (DSB), the molecule becomes linear in shape (form III) [37].

3.8.2.3. Gel concentration and buffer solution

As stated above, the concentration of the polymer will determine the size of the pores in the gel. This is governed primarily by the amount of total agarose used per unit volume and the degree of cross-linkage. The latter is determined by the relative percentage of agarose used. The percentage of agarose used depends on the size of fragments to be resolved. The concentration of agarose is referred to as a percentage of agarose to volume of buffer (w/v), and agarose gels are normally in the range of 0.2% to 3% [38]. The higher the concentration of agarose, the slower the DNA fragments migrate, thus when one wants to resolve smaller DNA fragments a high concentration of agarose should be used. It is very important to optimize the gel concentration in order to separate the DNA bands in study. The concentration of agarose according with the DNA size in base pairs (bp) is presented in Table 3.3.

Table 3.3 – Agarose gel concentration for resolving DNA molecules.

Concentration of agarose (%)	DNA size range (bp)
0.2	5000 – 40000
0.4	5000 – 30000
0.6	3000 – 10000
0.8	1000 – 7000
1	500 – 5000
1.5	300 – 3000
2	200 – 1500
3	100 – 1000

Another important factor to consider for an effective separation of the nucleic acids is the buffer solution selection for the assay. It is important to keep the pH of the system constant as well as the ionic strength (salt content), since without salt, the electrical conductance is marginal and the DNA barely moves [39]. Buffers not only establish a pH but also provide ions

to support conductivity. Several different buffers have been recommended for electrophoresis of DNA, however the most commonly used for DNA are TAE (Tris-acetate EDTA) and TBE (Tris-borate-EDTA). DNA fragments migrate with different rates in these two buffers due to differences in ionic strength.

3.8.2.4. Ethidium bromide staining

One of the most commonly used dyes to reveal DNA bands on an AGE is ethidium bromide (EB). EB is a fluorescent dye that intercalates between bases of nucleic acids and allows very convenient detection of DNA fragments in gels. The localization of DNA within the agarose gel can be determined directly by staining with low concentrations of EB and, after the electrophoretic running, the bands are revealed under UV light. The EB can be incorporated into agarose gels or included on the gel and buffer solution or the gel can be stained after DNA separation or added to samples of DNA before loading to enable visualization of the fragments within the gel. It is important to note that EB is a potent mutagen and moderately toxic after an acute exposure. Therefore, it is highly recommended to handle it with considerable caution.

In these studies, EB was added directly to the agarose gel, when its temperature was below 50 °C to avoid spillage and minimize exposure to this hazard.

3.9. AuNPs size distribution techniques

The effect of the Nd:YAG pulsed laser on the size of the AuNPs was evaluated with two different techniques described below.

3.9.1. Dynamic Light Scattering

Dynamic light scattering (DLS) analysis of AuNPs irradiated was performed using a Nanotrac® Flex 180° backscattering DLS system (Microtrac, UK) equipped with a red laser (780 nm, 5 mW) and a photodetector. This system measures the AuNPs size distribution of the samples in the range of 0.8 nm to 6.5 µm due to the applied heterodyne 180 ° back scattering principle. Heterodyning can be described as a signal processing technique that by combining two frequencies is able to originate a new frequency, being highly selective in the nano-range. The measuring is based on the focusing of the laser, through an optical fiber, and a sapphire window that will reflect a part of the incoming light (Figure 3.9). The diode detector will measure the scattered and reflected laser light and the fluctuating part of the signal is modulated by the Brownian diffusion of the particles and transformed into a power spectrum, which is referenced by the laser frequency. The size distribution of the particles in the sample results from the power spectrum, without assumption of any distribution model [40].

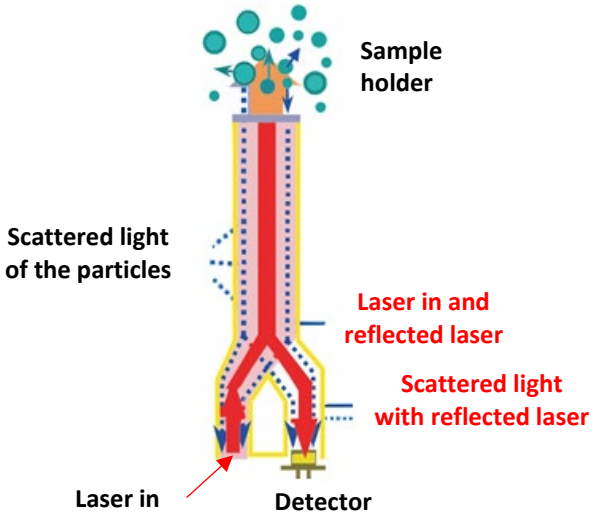

Figure 3.9 – Scheme of the 180° DLS-method [41].

For measuring the hydrodynamic size of the gold nanoparticles and their modifications with the increase of laser light exposure, 10 µl of AuNPs solutions were placed on the sample holder and were analysed in triplicate. Each measurement had an average of 30 seconds runs.

3.9.2. Transmission Electron Microscopy

Transmission Electron Microscopy (TEM) technique is based on the irradiation of the samples placed in the specimen holder with an electron beam and the diffracted electrons are converged by the objective lens to form a focused diffraction pattern or a diffraction spot at the back-focal plane of the objective lens (Figure 3.10). A phosphor screen is used to observe the images. The basic structure of the TEM consists of an electron gun, magnetic lens, image forming lens system with an objective, intermediate and projection lens, a phosphor screen placed under the projection lens (Figure 3.10).

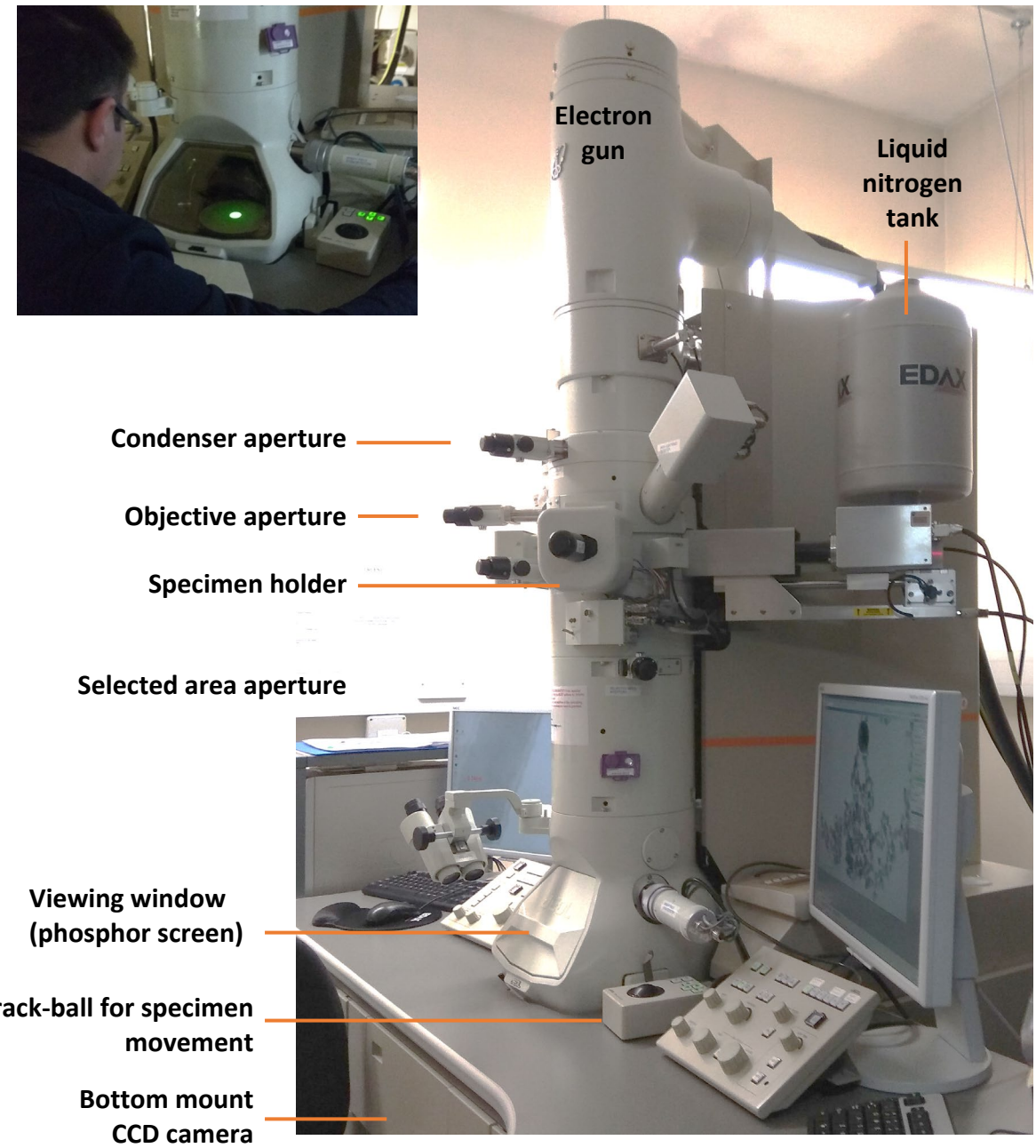

Figure 3.10 – TEM in at The Open University. Photograph taken by author of this thesis.

The AuNPs size distribution was measured by TEM imaging using a JEM-2100 TEM microscope (JEOL®, USA) at an accelerating voltage of 100 kV and a magnification from x50000 to x200000. 2 µl of AuNPs solution was air-dried overnight on an electrostatically discharged carbon mesh grid before electron microscopy. The nanoparticle's size was measured from thresholded TEM images using ImageJ® software, with area of the AuNPs being obtained. The AuNPs diameter was calculated from the area values from the 2D images, assuming that each AuNPs shape is a sphere, with projected area.

3.10. Chemicals

The chemicals and deoxyribonucleic acid (DNA) used in this work are listed in Table 3.4 and were used without further purifications. The aqueous solutions used in the present study were prepared with UHPW with quality of 18.2 MΩ.cm.

Table 3.4 – List of chemicals

Compound	Manufacture	Purity (%)	CAS/Catalogue number
U	Sigma-Aldrich	≥99.0%	66-22-8
^{5Br}U	Sigma-Aldrich	98%	51-20-7
^{5F}U	Sigma-Aldrich	≥99%	51-21-8
DNA sodium salt from calf thymus	Fluka	-	73049-39-5
pBV-Luc/Del-6	Addegene	-	14969
Ethanol	Sigma-Aldrich	≥99.8%	64-17-5
SeaKem® LE Agarose	Lonza	-	50004
Gold nanoparticles 40nm	BBI Solutions	-	EM.GC40
Coumarin-3-carboxylic acid	Sigma-Aldrich	99%	531-81-7
Dihydrorhodamine-123	Sigma-Aldrich	≥95%	109244-58-8
Phosphate-buffered saline	Sigma-Aldrich	-	MFCD00131855
Trizma® base	Sigma-Aldrich	≥99.0	77-86-1
Boric acid	Sigma-Aldrich	≥99.5%	10043-35-3
Ethylenediaminetetraacetic acid	Sigma-Aldrich	≥99%	6381-92-6

3.11. References

[1] R. Schürmann and I. Bald, “Decomposition of DNA Nucleobases by Laser Irradiation of Gold Nanoparticles Monitored by Surface-Enhanced Raman Scattering,” *J. Phys. Chem. C*, vol. 120, no. 5, pp. 3001–3009, 2016, doi: 10.1021/acs.jpcc.5b10564.

[2] T. S. Marques *et al.*, “Kinetics of Molecular Decomposition Under Irradiation of Gold Nanoparticles with Nanosecond Laser Pulses – A 5-Bromouracil Case Study,” *J. Chem. Phys.*, 2019.

[3] J. M. Campbell, C. von Sonntag, and D. Schulte-Frohlinde, “Photolysis of 5 -Bromouracil and Some Related Compounds in Solution,” *Z. Naturforsch*, vol. 29 b, pp. 750–757, 1974.

[4] H. Abdoul-Carime, M. A. Huels, F. Brüning, E. Illenberger, and L. Sanche, “Dissociative electron attachment to gas-phase 5-bromouracil,” *J. Chem. Phys.*, vol. 113, no. 7, pp. 2517–2521, 2000, doi: 10.1063/1.1306654.

[5] R. Schürmann and I. Bald, “Decomposition of DNA Nucleobases by Laser Irradiation of Gold Nanoparticles Monitored by Surface-Enhanced Raman Scattering,” *J. Phys. Chem. C*, vol. 120, no. 5, pp. 3001–3009, 2016, doi: 10.1021/acs.jpcc.5b10564.

[6] G. A. Kumar and J. Pid, “COMPARATIVE ANALYSIS OF IN VITRO ANTIMICROBIAL ACTIVITY OF 5-FLUOROURACIL AND 5-BROMOURACIL.”

[7] S. Christensen *et al.*, “5-Fluorouracil treatment induces characteristic T>G mutations in human cancer,” *bioRxiv*, p. 681262, 2019, doi: 10.1101/681262.

[8] J. D. Sara *et al.*, “5-fluorouracil and cardiotoxicity: a review,” *Ther. Adv. Med. Oncol.*, vol. 10, p. 175883591878014, 2018, doi: 10.1177/1758835918780140.

[9] A. Carattoli, “Plasmids in Gram negatives: Molecular typing of resistance plasmids,” *International Journal of Medical Microbiology*, vol. 301, no. 8. pp. 654–658, 2011, doi: 10.1016/j.ijmm.2011.09.003.

[10] M. Couturier, F. Bex, P. L. Bergquist, and W. K. Maas, “Identification and classification of bacterial plasmids,” *Microbiological Reviews*, vol. 52, no. 3. pp. 375–395, 1988.

[11] “Addgene: pBV-Luc/Del-6.” [Online]. Available: https://www.addgene.org/14969/. [Accessed: 20-Nov-2019].

[12] M. Dizdaroglu and P. Jaruga, “Mechanisms of free radical-induced damage to DNA,” *Free Radic. Res.*, vol. 46, no. 4, pp. 382–419, 2012, doi: 10.3109/10715762.2011.653969.

[13] A. Phaniendra, D. B. Jestadi, and L. Periyasamy, “Free Radicals: Properties, Sources, Targets, and Their Implication in Various Diseases,” *Indian J. Clin. Biochem.*, vol. 30, no.

1, pp. 11–26, 2015, doi: 10.1007/s12291-014-0446-0.

[14] V. M. Tandon, B. M. M. Gupta, and R. M. Tandon, “Free Radicals/Reactive Oxygen Species,” *JK-Practitioner*, vol. 12, no. 3, pp. 143–148, 2005.

[15] M.-A. Park, S. C. Moore, N. Limpa-Amara, Z. Kang, and G. M. Makrigiorgos, “Performance of a coumarin-based liquid dosimeter for phantom evaluations of internal dosimetry,” *Nucl. Instruments Methods Phys. Res. Sect. A Accel. Spectrometers, Detect. Assoc. Equip.*, vol. 569, no. 2, pp. 543–547, 2006, doi: 10.1016/J.NIMA.2006.08.090.

[16] K. Tornberg and S. Olsson, “Detection of hydroxyl radicals produced by wood-decomposing fungi,” *FEMS Microbiol. Ecol.*, vol. 40, no. 1, pp. 13–20, 2002, doi: 10.1016/S0168-6496(02)00200-3.

[17] S. Yamashita *et al.*, “Mechanism of radiation-induced reactions in aqueous solution of coumarin-3-carboxylic acid: Effects of concentration, gas and additive on fluorescent product yield,” *Free Radic. Res.*, vol. 46, no. 7, pp. 861–871, 2012, doi: 10.3109/10715762.2012.684879.

[18] G. Baldacchino *et al.*, “Determination of the time-dependent OH-yield by using a fluorescent probe. Application to heavy ion irradiation,” *Chem. Phys. Lett.*, vol. 468, no. 4–6, pp. 275–279, 2009, doi: 10.1016/J.CPLETT.2008.12.006.

[19] J. P. Crow, “Dichlorodihydrofluorescein and Dihydrorhodamine 123 Are Sensitive Indicators of Peroxynitritein Vitro:Implications for Intracellular Measurement of Reactive Nitrogen and Oxygen Species,” *Nitric Oxide*, vol. 1, no. 2, pp. 145–157, 1997, doi: 10.1006/NIOX.1996.0113.

[20] S. T. Wang *et al.*, “Sensitivity of activatable reactive oxygen species probes by fluorescence spectroelectrochemistry,” *Analyst*, vol. 138, no. 15, pp. 4363–4369, 2013, doi: 10.1039/c3an00459g.

[21] A. Gomes, E. Fernandes, and J. L. F. C. Lima, “Fluorescence probes used for detection of reactive oxygen species,” *J. Biochem. Biophys. Methods*, vol. 65, no. 2–3, pp. 45–80, 2005, doi: 10.1016/J.JBBM.2005.10.003.

[22] S. Forster, A. E. Thumser, S. R. Hood, and N. Plant, “Characterization of rhodamine-123 as a tracer dye for use in in vitro drug transport assays,” *PLoS One*, vol. 7, no. 3, 2012, doi: 10.1371/journal.pone.0033253.

[23] Qiagen, *QIAGEN ® Plasmid Purification Handbook Sample & Assay Technologies QIAGEN Sample and Assay Technologies*. 2012.

[24] M. Armbrecht, “Detection of contamination in DNA and protein samples by photometric measurements,” *Appl. Note 279*, no. 279, pp. 1–6, 2013.

[25] G. Koetsier, E. Cantor, and E. Biolabs, “A Practical Guide to Analyzing Nucleic Acid

Concentration and Purity with Microvolume Spectrophotometers."

[26] R. J. Steffan,' Jostein Goks0yr *et al.*, "Recovery of DNA from Soils and Sediments."

[27] NanoDrop Technologies, "NanoDrop and design are registered trademarks of NanoDrop Technologies 260/280 and 260/230 Ratios NanoDrop ® ND-1000 and ND-8000 8-Sample Spectrophotometers," 2007.

[28] E. Instrument, "What are Absorption, Excitation and Emission Spectra?" [Online]. Available: https://www.edinst.com/blog/what-are-absorption-excitation-and-emission-spectra/. [Accessed: 03-Jul-2021].

[29] "What is gel electrophoresis? | Facts | yourgenome.org." [Online]. Available: https://www.yourgenome.org/facts/what-is-gel-electrophoresis. [Accessed: 20-Nov-2019].

[30] K. Strutz and N. C. Stellwagen, "Do DNA gel electrophoretic mobilities extrapolate to the free-solution mobility of DNA at zero gel concentration?," *Electrophoresis*, vol. 19, no. 5, pp. 635–642, 1998, doi: 10.1002/elps.1150190504.

[31] S. Magdeldin, Ed., *Gel Electrophoresis - Principles and Basics*. Croatia: InTech, 2012.

[32] H. S. Chawla, "Basic Techniques," in *Introduction to Plant Biotechnology*, CRC Press, 2011, pp. 197–212.

[33] J. R. Brody and S. E. Kern, "History and principles of conductive media for standard DNA electrophoresis," *Analytical Biochemistry*, vol. 333, no. 1. pp. 1–13, 2004, doi: 10.1016/j.ab.2004.05.054.

[34] Z. Li and K. B. Grant, "DNA photo-cleaving agents in the far-red to near-infrared range - A review," *RSC Advances*, vol. 6, no. 29. Royal Society of Chemistry, pp. 24617–24634, 2016, doi: 10.1039/c5ra28102d.

[35] Rebecca Tirabassi, "How to Identify Supercoils, Nicks and Circles in Plasmid Preps - Bitesize Bio," 2017. [Online]. Available: https://bitesizebio.com/13524/how-to-identify-supercoils-nicks-and-circles-in-plasmid-preps/. [Accessed: 30-Oct-2019].

[36] M. A. Smialek, "Evaluating experimental molecular physics studies of radiation damage in DNA," 2016, doi: 10.1140/epjd/e2016-70390-3.

[37] C. Hamelin, "Production of single- and double-strand breaks in plasmid dna by ozone," *Int. J. Radiat. Oncol.*, vol. 11, no. 2, pp. 253–257, 1985, doi: 10.1016/0360-3016(85)90146-4.

[38] D. R. Smith, "Agarose Gel Electrophoresis," in *Transgenesis Techniques*, New Jersey: Humana Press, 1993, pp. 433–438.

[39] M. Somma and M. Querci, *Agarose Gel Electrophoresis (Session 5) - The Analysis of*

Food Samples for the Presence of Genetically Modified Organisms. European Commission DG-JRC, 2006.

[40] E. H. M. Sakho, E. Allahyari, O. S. Oluwafemi, S. Thomas, and N. Kalarikkal, “Dynamic Light Scattering (DLS),” in *Thermal and Rheological Measurement Techniques for Nanomaterials Characterization*, vol. 3, Elsevier, 2017, pp. 37–49.

[41] Microtrac, “Stabino® & NANO-flex System for Analysis of Charge Characteristics and Size Distribution of Nano-particles.” [Online]. Available: https://linden.ufsc.br/files/2013/11/Microtrac-Stabino-Nanoflex.pdf. [Accessed: 29-Oct-2019].

Chapter 4

Development of a DNA Biodosimeter for UV radiation

Development of a DNA Biodosimeter for UV radiation[1]

4.1. Abstract

Ultraviolet (UV) radiation has a strong influence in the damage of deoxyribonucleic acid (DNA). In this work, the possibility of a DNA UV radiation dosimeter is evaluated. For that, calf thymus DNA samples, thin films and aqueous solutions, were irradiated with 254 nm wavelength light during different periods of time, being the damage caused by the irradiation analysed by both UV-visible and infrared spectroscopies. As the DNA is a polyelectrolyte, the pH of the DNA samples was also considered as a variable. Results demonstrated that damage in DNA takes place in both thin films and solutions when irradiated at 254 nm, as revealed by a consistent decay in measured absorbance values. However, DNA solutions were seen to give more reliable results as the induced damage is easily measured. For this case, the absorbance at 260 nm was seen to exponentially decrease with the irradiation time as a result of radiation damage with the kinetics damage strongly dependent of pH. Consequently, the lifetime of such dosimeter device can be chosen by changing the pH of aqueous solutions.

This chapter is based on the following publication:

Marques, T.S., Pires, F., Magalhães-Mota, G., Ribeiro, P.A., Raposo, M., Mason, Nigel (2018) Development of a DNA Biodosimeter for UV radiation. Proceedings of the 6th International Conference on Photonics, Optics and Laser Technology. 1. pp. 328-333. SCITEPRESS. ISBN 978-989-758-286-8; DOI: 10.5220/0006732003280333.

4.2. Introduction

The use of radiation for medical procedures, in particular for diagnostic and therapy purposes, has dramatically increased over the years [1]. Mechanisms of justification of procedures and management of the patient dose are employed to avoid unnecessary or unproductive radiation exposure in diagnostic and interventional procedures. Dose constrains are appropriated to comforters and carers, and volunteers in biomedical research but regarding the therapeutic applications, it is not considered appropriate to apply dose limits or dose constraints, because such limits would often do more harm than good [2].

The effects induced on biological systems by electromagnetic radiation are due to the energy transfer into the medium with absorption of the radiation [3]–[5], and are characterized by a series of events which differ (and are classified) according to their reaction time scale, leading ultimately to biological damage [3]. These events can thus be divided into three groups: 1) Physical –interactions between the charged particles and the tissues atomic structures, which leads to ionization and concomitant formation of ionic radicals, in an extremely short time frame (around 10^{-18} s); 2) Chemical **–** formation of ion pairs through an ionization process, which leads to formation of free radicals and chemical bonds rupture (around 10^{-6} s); and 3) Biological – follows from bond rupture and is characterized by altering the proper physiology of cells or even cells death [5] the time that biological damage takes place after chemical bonds rupture is usually long, ranging from a few hours to several days, weeks, months, or even years.

When a cell is irradiated there are two types of changes which can occur, directly on the cellular component molecules or indirectly on water molecules, causing water-derived radicals. Radicals react with nearby molecules in a very short time, resulting in breakage of chemical bonds or oxidation of the affected molecules. The major effect in cells is DNA breaks [6]–[10]. Ionizing radiation can also lead to structural changes in several macromolecules present in cells. In nucleic acids, changes are essentially loss or damage of bases, thymine dimmers formation, single or double strand breaks and also DNA-protein dimmers formation [11], [12].

DNA is featured an interesting anionic polyelectrolyte having a unique double helix structure [13] that can be used for many purposes. For example, on the basis of hydrogen bonding properties of DNA base pairs, oligonucleotide probes have been recently designed to detect tumour gene and various biosensors were also proposed [14], [15]. Also, DNA aqueous solutions are of special interest, mainly in the development of biological sensors [7], [10].

Moreover, the DNA sequence defines the genetic information that commands the development of any living being and its main vital functions [6], [16], [17]. Since DNA plays an important role in the maintenance of the genetic information, any modification in this macromolecule has significant effects at the cellular level [18], [19]. Thus many efforts have been taken to delineate the mechanisms of formation and the chemical structures of the DNA modifications produced by genotoxic compounds, including also ionizing (X, gamma, heavy ions) and non-ionizing (ultraviolet (UV) and visible light) radiations [20].

The effects of ionizing radiation on DNA have been investigated in detail during the last three decades but one of the most common environmental health hazards that cause highly toxic effects is the UV radiation [1], [11], [12]. It should be referred here that UV radiation is classified as UVA (315-400 nm), UVB (290-315 nm), and UVC (280-100 nm). Most UVC is absorbed by the ozone layer, and only UVA and UVB compose ground level UV radiation [14], [21]. This is because, firstly, certain biomolecules such as proteins and nucleic acids have chromophores that absorb in the UV region of the spectrum. Under high UV fluxes, these molecules are photo-chemically degraded or transformed, resulting in impairment or even complete loss of biological function. The magnitude of damage caused by these so-called direct or primary mechanisms is determined by the amount of radiation absorbed (absorbance cross-section) and the quantum yield of photo-damage (molecules damaged per photon absorbed).

One class of UV toxicity effects is caused by a series of indirect mechanisms. UV is absorbed by some intermediate compound (photosensitising agent) either inside or outside the cell to produce reactive oxygen species (ROS) [22]. The resulting high energy oxidants such as hydrogen peroxide, superoxide or hydroxyl radicals can then diffuse and react with other cellular components with sites of damage that can be well away from the site of photo-production. Regarding genetic damage, nucleic acid bases absorb maximally in the UVC range,

with peak absorbance around 260 nm, and exhibit a tail that extends well into the UVB [22]. This absorbed energy results in the first excited singlet state, with a lifetime of only a few picoseconds. Most of this energy is dissipated by radiation less processes inside the molecule, but a small fraction is available for a variety of chemical reactions. This can result in the photo-damage of nucleotides [22], with a two- to four-fold greater effect on pyrimidines (thymine and cytosine) relative to purines (adenine and guanine). In addition, three principal photoproducts are formed by the UV-induced reactions: (a) 5,6-dipyrimidines, which are cyclobutane-type dimers, generally referred to simply as pyrimidine dimers; (b) photohydrates; and (c) pyrimidine (6—4) pyrimidones, often referred to as (6—4) photoproduct [22]. For example, skin aging, eye damage, and skin cancer are some of the most harmful effects known. This is because of increased production of cellular reactive oxygen species and by direct DNA damage, and if the DNA damage is not properly repaired, will lead to mutations and interferes with many cellular mechanisms (e.g. replication, transcription, and the cell cycle) [1].

If one intends to develop a device which allows the measurement of light dose based on biological materials, it should be chear that there are three kinds of biologic markers: exposure (dose), effect and susceptibility markers. Biologic markers of effect record biologic responses in individuals who have been exposed to a genotoxic agent, but markers of dose do not necessarily indicate effects. Superimposed on this are susceptibility markers; those that could be used to identify persons who are at increased risk of developing a disease that could be triggered by a radiation exposure. Included here might be organisms whose ability to repair DNA damage is limited [23].

Biological dosimetry does not measure the exposure in real time but the biological changes induced by radiation. There are both indicators of exposure or effects. Often the two aspects overlap as in the case of deterministic effects induced by high-doses, as for the acute radiation syndrome clinic that is characterized by damages in skin, haematopoietic, gastrointestinal, and cerebrovascular systems. In the case of stochastic effects, induced by low doses, the biomarkers used to measure the absorbed dose, not always imply a clear detriment of health. It has been, however, often demonstrated that an increase in the frequency of these indicators is associated with an increased risk of radiation-induced cancer and may be

indicative of radio-sensitivity [2]. According to [2], for a biodosimeter to be effective the following features are determinant: 1) measurement on tissues or fluids easily obtainable; 2) the effect must be specific of radiation; 3) response should vary directly depending on the dose; 4) it has to measure also chronic or repeated exposure; 5) it must be possible to measure retrospectively exposure also after years and 6) the measurement must be simple, fast or automated.

A simple method of analyse the effect of UV radiation on DNA is the measurement of AC electrical conductivity of DNA thin films [24]. Such study revealed that electrical conduction arises from DNA chain electron hopping between base-pairs and phosphate groups being the hopping distance a value of 3.3899±0.0002 Å which coincides with the distance between DNA base-pairs. Moreover, the loss of conductivity of DNA samples follow the decrease in phosphates groups with irradiation time, suggesting the use of DNA based films for UV radiation sensors [24]. Based in these achievements, in this paper, a new biological dosimeter-based radiation-induced lesions in DNA is proposed, where the damage caused by radiation is obtained by UV-visible (UV-Vis) and infrared spectroscopies and related to radiation exposure.

4.3. Materials and methods

Ultra-pure water and DNA hydrophilized in sodium salt form (DNA sodium salt from calf thymus, CAS 73049-39-5, acquired from Fluka®) was used for the preparation of DNA aqueous solutions. Its dissolution is favoured by the presence of sodium ion (counter-ion), allowing the preparation of aqueous solutions with anionic character. The concentration of the DNA solutions was 0.025 mg/mL DNA. The pH value of the DNA aqueous solution was 6, these solutions are also designated as natural solutions or pHN. In order to obtain DNA solutions with pH=9 and pH=3, the pH was adjusted to basic or acid with NaOH (1M) and HCl (1M), respectively.

Cast films were obtained by the drop casting method, i.e., depositing some drops of the DNA aqueous solutions with different pHs onto calcium fluoride (CaF_2) solid supports. These samples were placed in a desiccator during several hours to dry.

Solutions and cast films were irradiated for different periods of time by means of a 254 nm UVC germicide lamp, model TUV PL-L 55W/4P HF 1CT from Philips®, at an irradiance of 1.9 W/m^2, in a ventilated chamber at room conditions.

The DNA damage was monitored in aqueous solutions by measurements of UV-Vis spectra after each irradiation period in a spectrometer (UV 2101PC, Shimadzu®) while the thin films were characterized with a Fourier-transform infrared (FTIR) spectrometer Thermo Scientific Nicolet-model 530 (Waltham, MA, USA).

4.4. Results and discussion

According to [25], to develop a reliable system for measure the UV light dose, one have to search for material that would present the most adequate features: (i) high transmittance to UVB and UVA wavelengths; (ii) resistance to environmental adversities; (iii) possibility of framing the shape of the template according to the aim of the experiment; and (iv) low cost. Having into account such advices and the conclusions achieved by [24], it seemed that the use of DNA thin films should be interesting for the development of a UV dosimeter. Consequently, DNA cast films deposited onto CaF_2 and quartz were prepared from DNA aqueous solutions with pH 3, 6 (N) and 9. These films were irradiated with 254 nm UV radiation for different periods of time and the UV-vis and infrared spectra were measured for the different irradiation times. As expected, in the absence of water, the changes caused by radiation are minimal as can be inferred from the infrared spectra of the DNA cast films prepared from DNA aqueous solutions (pHN) before and after UV irradiation for 15 h, displayed in Figure 4.1. The observed peaks in the spectra are in accordance with [26] where the infrared absorbance peaks were systematically assigned to the respective DNA groups. Accordingly the range of wavenumbers contained between 1250 and 900 cm^{-1} are associated with the phosphate backbone region while 1500–1250 cm^{-1} and 1800–1500 cm^{-1}

wavenumber regions are associated to DNA bases vibrations influenced by the sugar component and to DNA bases, respectively [26].

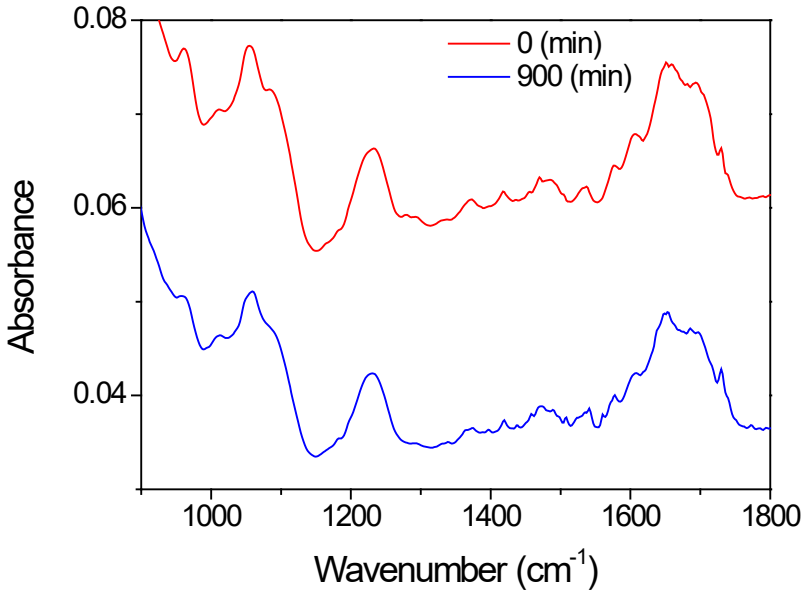

Figure 4.1 – FTIR spectra of DNA casted films prepared from solutions at natural pH (pH 6) conditions before and after irradiation with UV-light at 254nm wavelength during 900 min (15 h).

Since UV radiation has effect on DNA phosphates groups as demonstrated by Gomes et al [27], the values of absorbance at 1097 cm^{-1}, assigned to the presence of symmetric PO_2^- stretching of backbone in the DNA molecules [26], were plotted in Figure 4.2 as a function of the irradiation time for samples prepared from DNA aqueous having different pH. Generally, an absorbance decay is observed. However, these measurements are always tricky due to baseline fluctuations and also if the molecules concentration seen by the beam is not identical–leading to absorbance deviations. To circumvent this drawback, the analysis of the effect of UV radiation at 254 nm was carried out on DNA aqueous solutions prepared at different pHs.

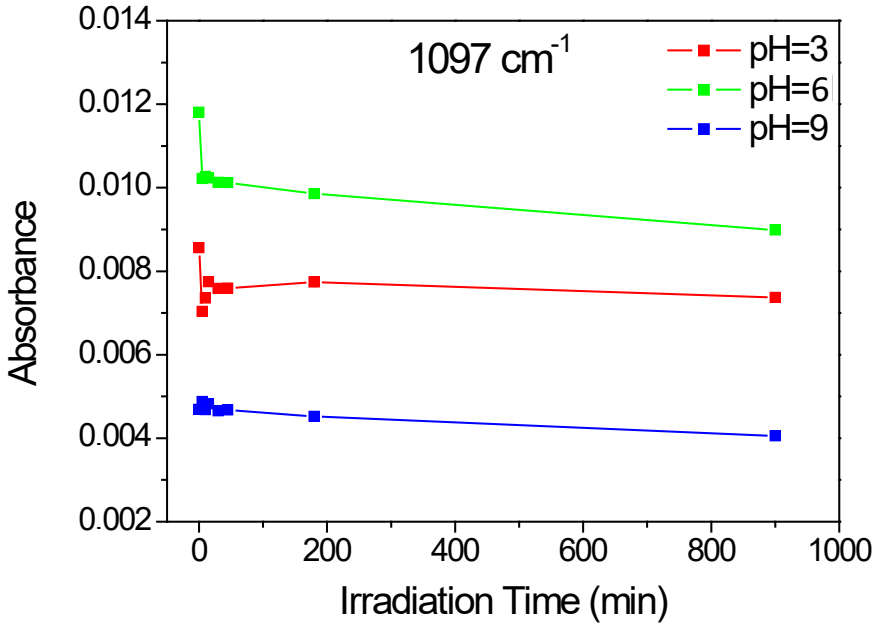

Figure 4.2 – Absorbance at 1097 cm^{-1} after baseline subtraction *versus* irradiation time for the different DNA cast films prepared from aqueous solutions with different pHs.

Figure 4.3a), b) and c) present the UV-vis spectra obtained for the DNA aqueous solutions with pH=3, pH=6 and pH=9, respectively, irradiated during different periods of time. The obtained results point out that the DNA solutions with pH=3 (Figure 4.3a) tend to be more sensitive to higher times of UV light exposure since the absorbance at 260 nm for 900 minutes of irradiation was the lowest value found for the different DNA solutions studied. The baselines changes can be due to the light scattering of smaller molecules, originated by the cleavage of DNA molecule during the irradiation, as demonstrated by [24].

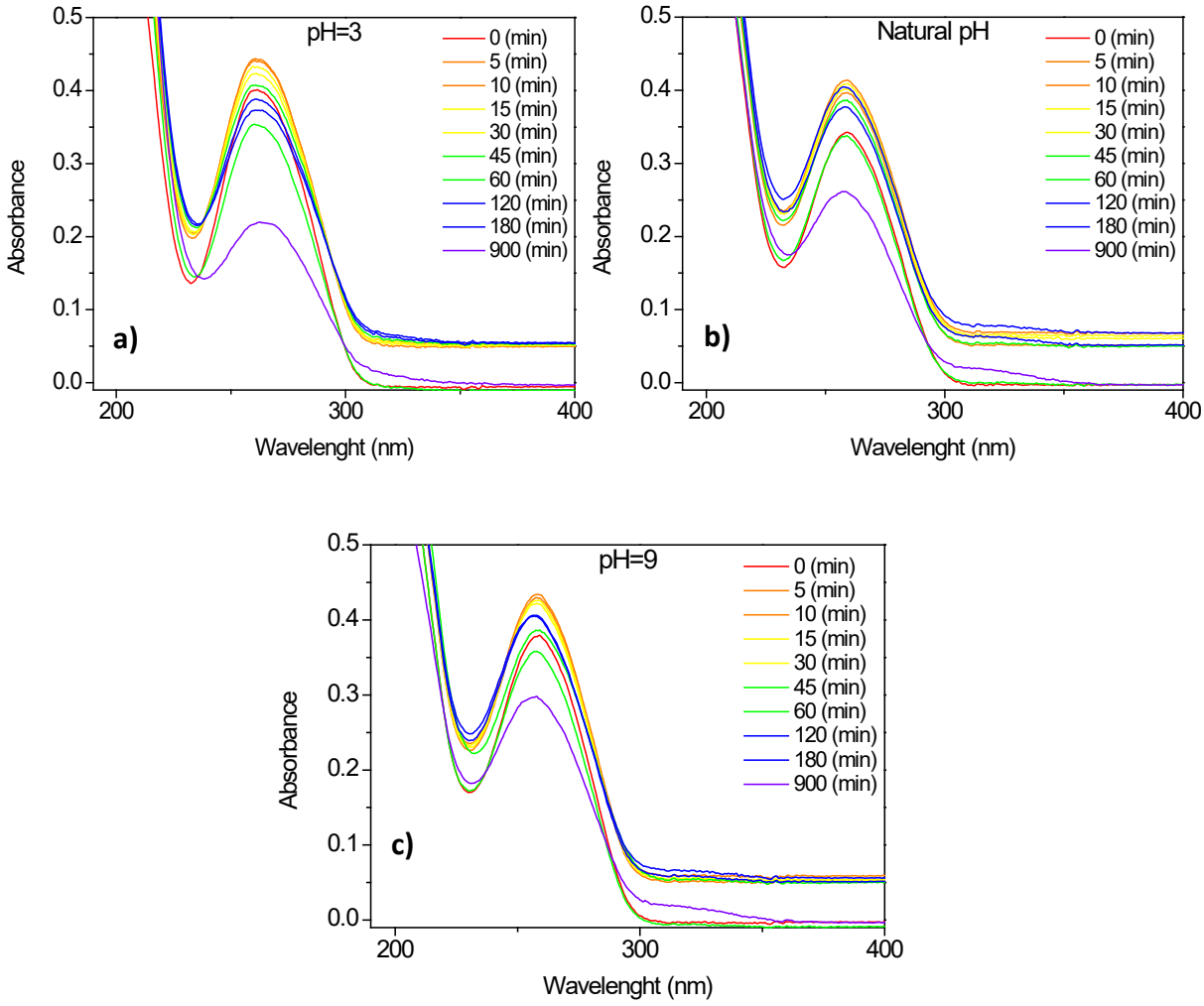

Figure 4.3 – Absorption spectra of DNA solutions with: a) pH=3; b) pH=6 (natural) and c) pH=9; irradiated with 254 nm wavelength light for different periods of time.

The obtained results are in accordance with literature as similar behaviours and patterns are observed by [28], where the disinfection of water was studied and they present the effect of UV radiation on the spores.

For a better comparison, the absorbance values at 260 nm, after removing the baseline (i.e. subtracting the value of the absorbance at 350 nm), were normalized, for each pH, and plotted as a function of the irradiation time in Figure 4.4. Several attempts have been done to find the best equation to model the experimental data. The normalized experimental data $(NAbs)$ was found to be best fitted by an exponential like expression as follows:

$$NAbs = \frac{Abs_{260nm}}{Abs0_{260nm}} = exp\left(-\left(\frac{t}{\tau}\right)^{n}\right) \quad [4.1]$$

in which Abs_{260nm} is the absorbance at 260 nm, $Abs0_{260nm}$ corresponds to the initial (at the beginning of the experiments) absorbance at 260 nm, t the time in minutes, τ is the characteristic time or time constant and *n* is a constant which can be related with the order of the kinetics process [29] with respect to radiation damage.

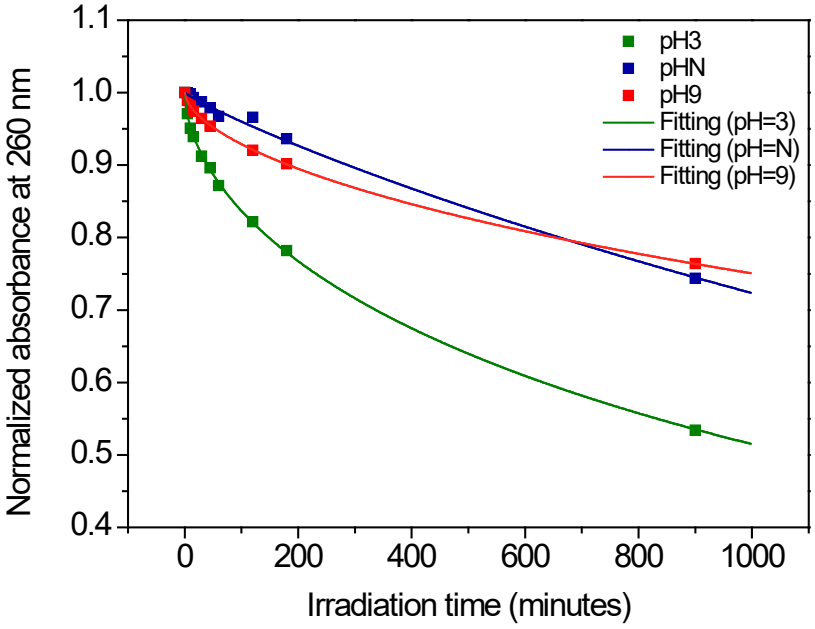

Figure 4.4 – Normalized absorbance at 260 nm after removing the baseline *versus* irradiation time for the different solutions. The lines correspond to the fitting with equation [4.1].

Figure 4.5 shows the plot of the time constants in minutes for each pH. The results show that DNA solutions at higher pH (more basic) can be exposed to UV light during more time. Moreover, from equation [4.1] one can propose an expression for the dose level to which the sample has been subjected, as follows:

$$D = -\frac{C_D}{n} ln \frac{Abs_{260nm}}{Abs0_{260nm}} \quad [4.2]$$

in which *D* is the dose calculated by multiplying the irradiance by the irradiation time, C_D is the characteristic dose constant and *n* is the order parameter of the damage kinetics.

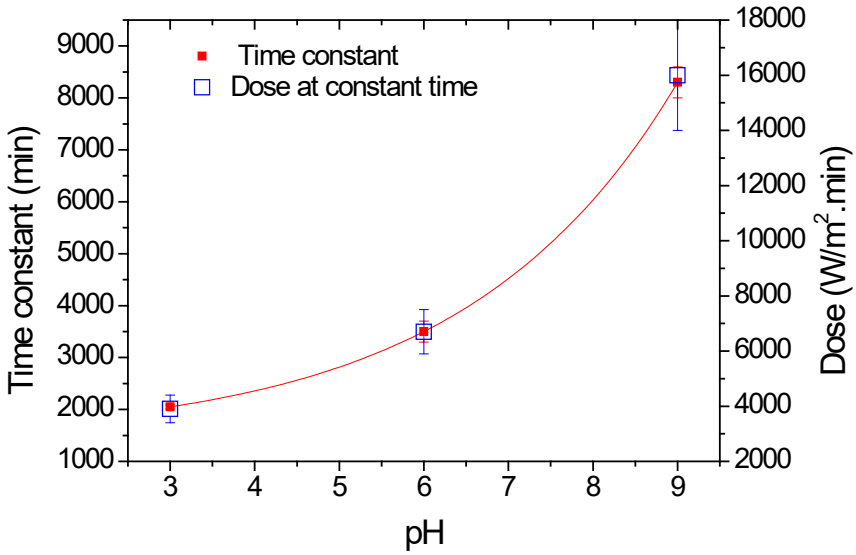

Figure 4.5 – Time constant obtained by equation [4.2] *versus* pH of the solutions irradiated and estimated dose for the constant time for the solutions irradiated.

These parameters as well as the characteristic time constants are presented in Table 4.1 for each pH investigated. From the obtained results, one can conclude that DNA solutions can be suitable for the measurement of 254 nm wavelength light dose, being the lifetime of such dosimeter device dependent of solution pH. To develop a DNA based dosimeter device to cover also UV A and UV B region, DNA damage has also to be investigated in these UV regions. According with previous results [27], damage is expected also take place with 300 nm wavelength light in such a way that the same procedure described here should be used to analyse the DNA damage when the solutions are irradiated with higher wavelength light.

Table 4.1 – Coefficients determined to each pH of DNA solution irradiated.

pH	τ (min)	C_D ($Wm^{-2}.min$)	n
3	2050±40	3890±70	0.571±0.005
6	3500±200	6700±300	0.90±0.03
9	8300±300	15800±600	0.590±0.007

4.5. Conclusions

In this work it was demonstrated that aqueous DNA solutions can be used to probe UV radiation at 254 nm and to evaluate the radiation dose at 254 nm, through absorbance measurements. The absorbance was seen to exponentially decrease with irradiation time being the damage kinetics parameter dependent of pH DNA aqueous solutions. This work also evidenced that the lifetime of such DNA dosimeter device can be chosen changing the pH of those solutions. In the future we intent to 1) irradiate the samples with a fixed wavelength of 300 nm in order to check the new kinetics damage; 2) check if there is a linear correspondence to the irradiation power; and 3) study the sensibility of the potential sensor.

4.6. Acknowledgements

The authors acknowledge the financial support from FEDER, through Programa Operacional Factores de Competitividade—COMPETE and Fundação para a Ciência e a Tecnologia—FCT, by the project PTDC/FIS-NAN/0909/2014 and for the Portuguese research Grants No. PEst-OE/FIS/UI0068/2011 and UID/FIS/00068/2013. Telma Marques and Filipa Pires acknowledge the fellowships SFRH/BD/106032/2015 and PD/BD/106036/2015, respectively from RABBIT Doctoral Programme (RaBBiT, PD/00193/2012), Portugal.

4.7. References

[1] S. L. Yu and S. K. Lee, “Ultraviolet radiation: DNA damage, repair, and human disorders,” *Molecular and Cellular Toxicology*, vol. 13, no. 1. Springer Verlag, pp. 21–28, 01-Mar-2017.

[2] A. Giovanetti, A. Sgura, and G. Aversa, *Biological dosimetry : how to measure the absorbed dose in different scenarios*. ENEA, 2012.

[3] J. H. Bernhardt, “Non-ionizing radiation safety: Radiofrequency radiation, electric and

magnetic fields," *Physics in Medicine and Biology*, vol. 37, no. 4. pp. 807–844, 1992.

[4] J. D. Bronzino, *The Biomedical Engineering Handbook: Four Volume Set - CRC Press Book*, 2nd ed. CRC Press & IEEE Press, 1995.

[5] J. E. Moulder, *Power Lines and Cancer FAQs*. Medical College of Wisconsin, 2007.

[6] P. J. P. Gomes, "Characterization of Molecular Damage Induced by UV Photons and Carbon Ions on Biomimetic Heterostructures. PhD Dissertation," no. December 2014, 2014.

[7] X. H. Xu and A. J. Bard, "Immobilization and Hybridization of DNA on an Aluminum(III) Alkanebisphosphonate Thin Film with Electrogenerated Chemiluminescent Detection," *J. Am. Chem. Soc.*, vol. 117, no. 9, pp. 2627–2631, 1995.

[8] J. J. Storhoff and C. A. Mirkin, "Programmed Materials Synthesis with DNA," *Chem. Rev.*, vol. 99, no. 7, pp. 1849–1862, 1999.

[9] E. B. Podgorsak, *Radiation Physics for Medical Physicists*, Second. Springer, 2010.

[10] H. Su, K. M. R. Kallury, M. Thompson, and A. Roach, "Interfacial Nucleic Acid Hybridization Studied by Random Primer 32P Labeling and Liquid-Phase Acoustic Network Analysis," *Anal. Chem.*, vol. 66, no. 6, pp. 769–777, Mar. 1994.

[11] C. Kielbassa, L. Roza, and B. Epe, "Wavelength dependence of oxidative DNA damage induced by UV and visible light," *Carcinogenesis*, vol. 18, no. 4, pp. 811–816, Apr. 1997.

[12] J.-L. Ravanat, T. Douki, and J. Cadet, "Direct and indirect effects of UV radiation on DNA and its components," *J. Photochem. Photobiol. B Biol.*, vol. 63, no. 1–3, pp. 88–102, Oct. 2001.

[13] D. Freifelder, *Molecular biology*. Narosa, 2005.

[14] F. Caruso and H. Möhwald, "Protein multilayer formation on colloids through a stepwise self- assembly technique," *J. Am. Chem. Soc.*, vol. 121, no. 25, pp. 6039–6046, Jun. 1999.

[15] Y. Lvov, G. Decher, and G. Sukhorukov, “Assembly of Thin Films by Means of Successive Deposition of Alternate Layers of DNA and Poly(allylamine),” *Macromolecules*, vol. 26, no. 20, pp. 5396–5399, 1993.

[16] M. H. Wilkins, A. R. Stokes, and H. R. Wilson, “Molecular Structure of Nucleic Acids: Molecular Structure of Deoxypentose Nucleic Acids,” *Nature*, 1953.

[17] R. E. Franklin and R. G. Gosling, “Evidence for 2-chain Helix in crystalline structure of sodium deoxyribonucleate,” *Nature*, vol. 172, no. 4369, pp. 156–157, 1953.

[18] T. Lindahl, “Instability and decay of the primary structure of DNA,” *Nature*, vol. 362, no. 6422. pp. 709–715, 1993.

[19] K. B. BECKMAN and B. N. AMES, “The Free Radical Theory of Aging Matures,” *Physiol. Rev.*, vol. 78, no. 2, pp. 547–581, Apr. 1998.

[20] J. L. Ravanat and T. Douki, “UV and ionizing radiations induced DNA damage, differences and similarities,” *Radiat. Phys. Chem.*, vol. 128, pp. 92–102, Nov. 2016.

[21] J. Kalinowski, “Electroluminescence in organics,” *J. Phys. D. Appl. Phys.*, vol. 32, no. 24, Dec. 1999.

[22] W. F. Vincent and P. J. Neale, “Mechanisms of UV damage to aquatic organisms,” in *The effects of UV radiation in the marine environment*, Cambridge University Press, 2000, pp. 149–176.

[23] National Research Council, *Biologic Dosimetry and Biologic Markers: Radiation Dose Reconstruction for Epidemiologic Uses*. The National Academies Press, 1995.

[24] P. J. Gomes, M. Coelho, M. Dionísio, P. António Ribeiro, and M. Raposo, “Probing radiation damage by alternated current conductivity as a method to characterize electron hopping conduction in DNA molecules,” *Appl. Phys. Lett.*, vol. 101, no. 12, 2012.

[25] A. P. Schuch, C. C. M. Garcia, K. Makita, and C. F. M. Menck, “DNA damage as a

biological sensor for environmental sunlight," *Photochemical and Photobiological Sciences*, vol. 12, no. 8. pp. 1259–1272, Aug-2013.

[26] P. J. Gomes, P. A. Ribeiro, D. Shaw, N. J. Mason, and M. Raposo, "UV degradation of deoxyribonucleic acid," *Polym. Degrad. Stab.*, vol. 94, no. 12, pp. 2134–2141, 2009.

[27] I. Abril *et al.*, "SKIN CANCER:AN OVERVIEW OF EPIDEMIOLOGY AND RISK FACTORS," *Semin. Oncol. Nurs.*, vol. 29, no. 1, pp. 1–5, 2015.

[28] R. Z. Chen, S. A. Craik, and J. R. Bolton, "Comparison of the action spectra and relative DNA absorbance spectra of microorganisms: Information important for the determination of germicidal fluence (UV dose) in an ultraviolet disinfection of water," *Water Res.*, vol. 43, no. 20, pp. 5087–5096, Dec. 2009.

[29] M. Raposo, R. S. Pontes, L. H. C. Mattoso, and O. N. Oliveira, "Kinetics of adsorption of poly(o-methoxyaniline) self-assembled films," *Macromolecules*, vol. 30, no. 20, pp. 6095–6101, Oct. 1997.

Chapter 5

Kinetics of Molecular Decomposition under Irradiation of Gold Nanoparticles with nanosecond Laser Pulses – A 5-Bromouracil case study

Decomposition of 5-Bromouracil[1]

5.1. Abstract

Laser illuminated gold nanoparticles (AuNPs) efficiently absorb light and heat up the surrounding medium, leading to versatile applications ranging from plasmonic catalysis to cancer photothermal therapy. Therefore, an in-depth understanding of the thermal, optical, and electron induced reaction pathways is required. Here, the electrophilic DNA nucleobase analog 5-Bromouracil (5BrU) has been used as a model compound to study its decomposition in the vicinity of AuNPs illuminated with intense ns laser pulses under various conditions. The plasmonic response of the AuNPs and the concentration of 5BrU and resulting photoproducts have been tracked by ultraviolet and visible (UV–Vis) spectroscopy as a function of the irradiation time. A kinetic model has been developed to determine the reaction rates of two parallel fragmentation pathways of 5BrU, and their dependency on laser fluence and adsorption on the AuNP have been evaluated. In addition, the size and the electric field enhancement of the decomposed AuNPs have been determined by atomic force microscopy and finite domain time difference calculations, respectively. A minor influence of the direct photoreaction and a strong effect of the heating of the AuNPs have been revealed. However, due to the size reduction of the irradiated AuNPs, a trade-off between laser fluence and plasmonic response of the AuNPs has been observed. Hence, the decomposition of the AuNPs might be limiting the achievable temperatures under irradiation with several laser pulses. These findings need to be considered for an efficient design of catalytic plasmonic systems.

[1]This chapter is based on the following publication:

Telma S. Marques, Robin Schürmann, Kenny Ebel, Christian Heck, Małgorzata A. Śmiałek, Sam Eden, Nigel Mason and Ilko Bald. Kinetics of Molecular Decomposition under Irradiation of Gold Nanoparticles with nanosecond Laser Pulses – A 5-Bromouracil case study. The Journal of Chemical Physics, 152, 124712 (2020); doi: 10.1063/1.5137898.

5.2. Introduction

Gold nanoparticles (AuNPs) provide versatile applications in the fields of sensing [1], [2], catalysis [3] and cancer therapy [4], [5]. Localized surface plasmons (LSPs, collective oscillations of the conduction band electrons) are responsible for the outstanding optical properties of AuNPs and can be excited by the alternating electric field of incident light [6]. LSPs strongly enhance the electric field around the nanoparticle, especially when the frequency of the light matches the eigenfrequency of the LSP resonance (LSPR). LSPs can decay in a non-radiative pathway by forming electron-hole pairs, which is typically the initial step in plasmon mediated catalysis [3], [7], [8]. Since the energy of these plasmonically generated electrons exceeds the thermal equilibrium of the electron gas, they rapidly distribute their energy via electron-electron scattering in the electron gas and subsequently heat up the lattice of the NPs and the surrounding medium [9], [10]. Under irradiation with intense ns laser pulses, the temperature of the AuNPs can be easily increased to some 1000 K [11], which causes surface evaporation and fragmentation of the AuNPs [12], even under irradiation with a single laser shot [13]. In this process, the morphology of the transformed AuNPs crucially depends on the irradiation parameters [14]. Furthermore, a high temperature and pressure region is generated around the AuNPs if the laser intensity is sufficiently high [15]. The properties of these nanobubbles are highly dependent on the size of the nanoparticles and the properties of the laser pulse [16], [17]. Under illumination of AuNPs with focused laser pulses, the generation of reactive secondary species such as singlet oxygen [18] and low energy electrons has been observed [19]. As high temperatures are required for the thermionic emission process [20], a threshold for the efficient generation of electrons is expected, which depends on the size of the AuNPs. Biomolecules, such as DNA [21]–[23] or proteins [24]–[26], located in a nanoscopic volume around such irradiated AuNPs are efficiently decomposed under laser illumination. In that context, the adsorption of the molecules to the AuNPs surface strongly influences the decomposition process. This is due to two effects: (1) the number of molecules in the high energy in the pressure region is increased and (2) the aggregation process of the AuNPs determining the size and, consequently, the plasmonic response is guided by the capping molecules [22], [27]. The decomposition of DNA is of particular interest for future applications in cancer photothermal therapy, where cancer cells are killed by an increase of temperature mediated by incorporated laser illuminated

AuNPs [4], [28]. The irradiation of biological tissue with intensive laser pulses leads to an efficient damage, as beyond the Joule heating, various nanoscopic effects around the AuNPs enhance the cellular damage [29]. Even though the effects occurring in the vicinity of AuNPs illuminated with ns-laser pulses have been widely studied, their influence on biomolecules in the surrounding medium on the molecular scale is not yet fully understood. The DNA nucleobase analog 5-Bromouracil (5BrU) has been proposed as a potential DNA radiosensitizer in cancer radiation therapy [30], and consequently, its reactions have been extensively studied previously [31], [32]. For this purpose, 5BrU has been used as a model compound to study the reactions in the vicinity of AuNPs under pulsed laser irradiation. Brominated nucleobases are known to be highly reactive with low energy electrons [31], [33]–[35]. The attachment of an electron with a kinetic energy close to 0 eV resonantly cleaves the carbon bromide bond of the nucleobases [33], [35]. This reaction has been observed recently on the surface of noble metal NPs triggered by plasmonically generated electrons [34]. However, this electron induced reaction occurs close to the surface of the NPs where the highest temperatures occur, and consequently, the desorption of the reaction products without further decomposition is very unlikely.

In order to obtain an in-depth understanding of the molecular decomposition processes in the surrounding of laser illuminated AuNPs, the kinetics of different reaction pathways of 5BrU are studied as a function of irradiation related parameters within the present work. By monitoring the photoproducts of irradiated 5BrU in parallel with optical and morphological properties of the irradiated AuNPs the tunability of the plasmon catalyzed system can be evaluated.

5.3. Experimental details

5.3.1. Chemicals

AuNPs with 40 nm average diameter have been purchased from BBI solutions. 5BrU has been purchased from Sigma Aldrich and was dissolved in ultrapure water obtained with a Milli-Q water purification system.

5.3.2. Laser Irradiation

A scheme of the experimental setup is shown in **Figure 5.1**. Ns Laser pulses have been generated using the second harmonic of a Minilite I (Continuum) Nd:YAG laser at 532 nm with an energy of 16 mJ per pulse and a pulse width of 3-5 ns. Unless stated otherwise, a repetition rate of 15 Hz has been used. The laser beam has been widened by using a set of two lenses from a diameter of 3 mm to 9 mm. Subsequently, the beam has been guided by a dichroic mirror to a further lens (f = 5 cm) and focused on a 3.5 ml quartz cuvette (Hellma®) slightly above the surface of the AuNP solution. The cuvette is filled with 2 ml of solution, typically containing 45 pM AuNPs and 40 µM 5BrU, and placed on a stirring plate to stir the solution during the irradiation. Using a mechanical stage, the distance of the laser focus to the surface of the AuNP solution has been varied to adjust the spot size and, in consequence, the laser fluence of the divergent beam on the surface. The laser fluences given below refer to the maximum laser fluence at the surface, without considering the widening of the beam inside the cuvette. The size of the focused laser beam has been determined using an optical microscope and a blackened photographic paper irradiated with a single laser shot.

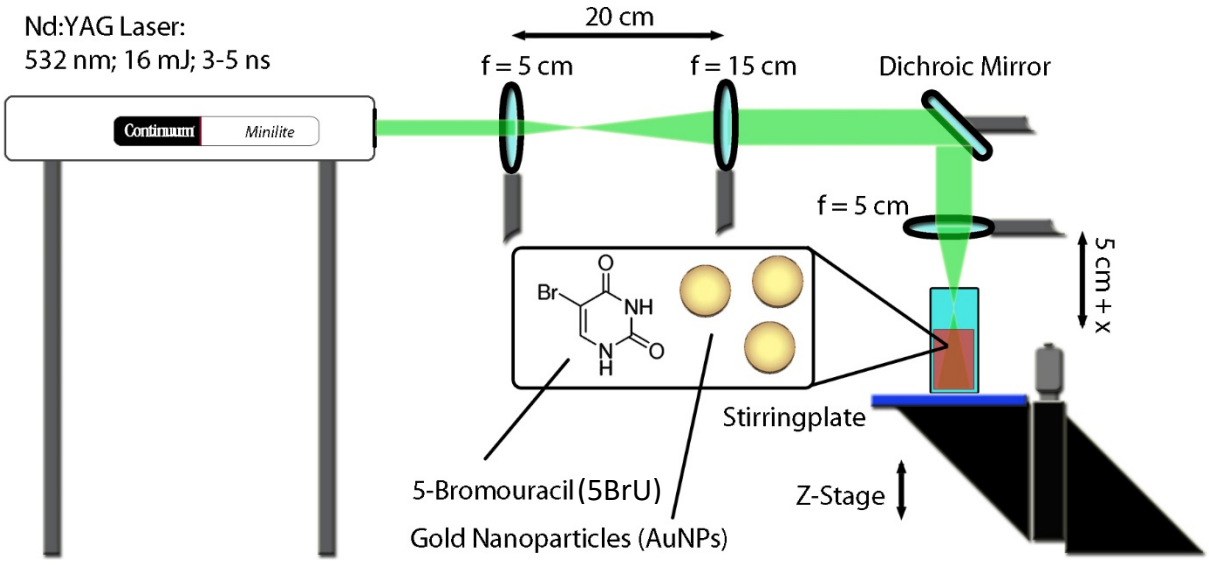

Figure 5.1 – Schematic representation of the experimental setup.

5.3.3. Analytical methods

Ultraviolet and visible (UV–Vis) extinction spectra were recorded with a Jasco 650 spectrophotometer. Dried AuNPs have been imaged with an Agilent 5500 atomic force microscope (AFM) using a Tap 150 cantilever in the tapping mode. For the sample preparation, a 2 µl droplet of the irradiated AuNP solution has been dried on a freshly cleaved mica substrate. The size distribution of the AuNPs on the substrate has been determined from the height of the AuNPs in the AFM images by using the software Gwyddion 2.48.

5.3.4. FDTD calculations

Finite domain time difference (FDTD) calculations of the electric field enhancement of AuNPs in an aqueous medium have been carried out with the software Lumerical FDTD Solutions 8.6.3, using a mesh size of 0.1 nm in the plotted areas. The excitation wavelength was set to 532 nm.

5.4. Results and discussions

Using the experimental setup presented in Figure 5.1, a mixture of AuNPs and 5BrU has been irradiated with ns laser pulses. UV-Vis spectra have been recorded after specific illumination times in order to determine the LSPR of the AuNPs and the π-π* resonance of 5BrU. In Figure 5.2a), a typical dataset is presented showing that the LSPR, which is initially located at 528 nm, is decreased and blue shifted with ongoing irradiation. This change of the LSPR is caused by the decomposition of the AuNPs into smaller fragments. Already after 5 min of irradiation, only small changes in the LSPR are observable, which indicates only slight changes in the size distribution, and thus, approximately constant reaction conditions for the molecular decomposition can be assumed. Moreover, also the intensity of the π–π∗ transition of 5BrU, located at 277 nm [36], is reduced and shifted to lower wavelength during the irradiation. The decrease in the π-π* resonance is attributed to a cleavage of the aromatic ring structure,

whereas the shift of the resonance maximum indicates a chemical modification of the 5BrU, most likely the cleavage of the C-Br bond leaving the residual molecule intact [21].

In order to further analyse the π-π* transition, all additional contributions of the solution to the extinction in this wavelength regime need to be determined to correct the background of the 5BrU spectra (see Figure 5.2b)). Therefore, AuNPs have been irradiated in absence of 5BrU under the same experimental conditions, as the absorption of AuNPs in the UV caused by interband transitions depends significantly on the particle size (see S.I. 5.9.2).

The spectra of the irradiated AuNP solution have been subtracted from the spectra of the irradiated AuNP/5BrU solution for each irradiation time. In addition, the absorption band located below 210 nm has been fitted with a Gaussian peak and subtracted from the AuNP/5BrU spectra, since there are slight contributions of these signals to the π-π* peak. To determine the contributions of the π-π* transitions of 5BrU and U, the background corrected AuNP/5BrU spectra of the π-π* transition, shown in Figure 5.2c), have been fitted with two Gaussian peaks centered at 277 nm and 258 nm [37], respectively. In this way, the concentration 5BrU *[BrU]* and of U *[U]* can be monitored as a function of the irradiation time.

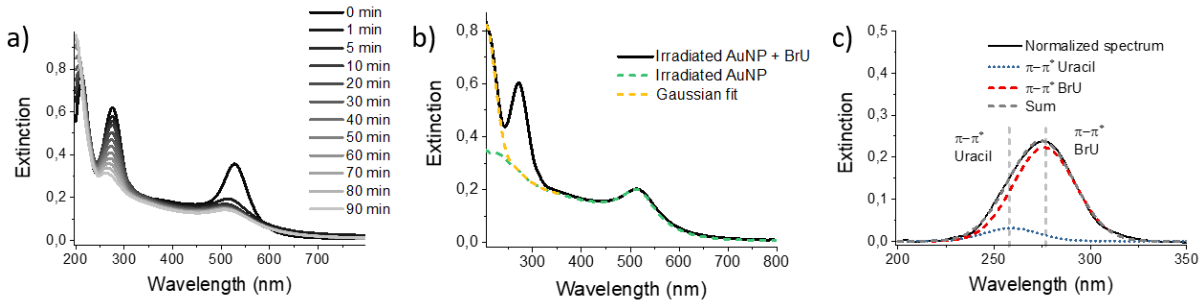

Figure 5.2 – (a) UV–Vis spectra of the AuNP/5BrU solution irradiated with focused 532 nm ns laser pulses with a repetition rate of 15 Hz and a maximum laser fluence of 3.4 × 1012 W/m2. (b) UV–Vis spectra of the irradiated AuNP/5BrU solution (black), a spectrum of illuminated AuNPs under the same conditions (green, dashed), and a Gaussian fit of the peak centered below 210 nm (yellow, dashed). (c) π–π∗ signal (black) corrected by the contributions marked in (b). The Gaussian fit of the contributions of U (blue) and 5BrU (red) and their sum (grey) are plotted with dotted lines.

In order to explain the shift and the decrease of the π-π* signal, two reaction pathways are assumed: the fragmentation of the molecular ring leading to a decrease in the π-π* resonance,

$$BrU \overset{k1}{\rightarrow} small\ fragments, \quad [5.1]$$

and the cleavage of the C-Br bond resulting in the formation of Uracil (U),

$$BrU \overset{k2}{\rightarrow} U, \quad [5.2]$$

where k_1 and k_2 denote the reaction rates for the fragmentation of the ring and the cleavage of the C-Br bond, respectively. In addition, also a third reaction with a reaction rate k_3 needs to be considered, since the generated U will also be decomposed under laser irradiation in the presence of AuNPs into smaller fragments.

$$U \overset{k3}{\rightarrow} small\ fragments, \quad [5.3]$$

Based on equation [5.1] and [5.2], the decomposition of 5BrU follows a (pseudo-)first order reaction that can be described by the following equation:

$$\frac{d[5BrU]}{dt} = -k_1[BrU] - k_2[BrU]. \quad [5.4]$$

According to equation [5.2] and [5.3], the generation and decomposition of U can be described by:

$$\frac{d[U]}{dt} = -k_3[U] + k_2[BrU]. \quad [5.5]$$

From equation [5.4], we obtain for the concentration of 5BrU, *[BrU]*, after an irradiation time t,

$$[BrU] = [BrU]_0 e^{-(k_1+k_2)t}, \quad [5.6]$$

Where $[BrU]_0$ is the initial concentration of BrU before the irradiation. Since there has been initially no U in the solution, we set $[U_0] = 0$ and obtain [U] (see the S.I. 5.9.1),

$$[U] = \frac{k_2[BrU]_0}{k_3 - k_1 - k_2}\left(e^{-(k_1+k_2)t} - e^{-k_3 t}\right). \quad [5.7]$$

Consequently, the ratio of *[U]* and *[BrU]* can be determined using equation [5.6] and [5.7],

$$\frac{[U]}{[BrU]} = \frac{k_2}{k_3 - k_1 - k_2}\left(1 - e^{-(k_3-k_1-k_2)t}\right). \quad [5.8]$$

By using the Taylor expansion $e^x \approx 1 + x$, we can simplify the expression for short illumination times *t* to

$$\frac{[U]}{[BrU]} \approx k_2 t. \quad [5.9]$$

With this equation, the reaction rate k_2 can be determined from the ratio of the concentrations *[BrU]* and *[U],* which can be determined from the π-π* resonances at 258 nm and 277 nm in the UV-Vis spectra as a function of the irradiation time *t* (see Figure 5.3a)). Error bars have been determined from the background subtraction of the AuNP signal in the absence of 5BrU, and the fits are presented in Figure 5.2b) and Figure 5.2c). Due to the strong changes in the AuNP size after the influence of first laser pulses (see text below and Figure 5.6) on the reaction conditions, the data points after 0 min and 1 min irradiation time have not been taken into account in the analysis. The determined ratio of *[BrU]* and *[U]* typically follows the expected linear trend after the particle size remains constant.

In Figure 5.3b), *[BrU]* is plotted as a function of *t* and fitted with an exponential decay; hence, the sum of the reaction rates k_1 and k_2 can be determined from the fit by using equation [5.6]. However, for short and very long irradiations times, the exponential correlation is only valid in a first approximation due to the reduced signal to background ratio of the π-π* resonance for long illumination times. Therefore, based on the experimental data, it cannot be finally excluded that the reaction might also follow a zeroth or some more complex reaction order.

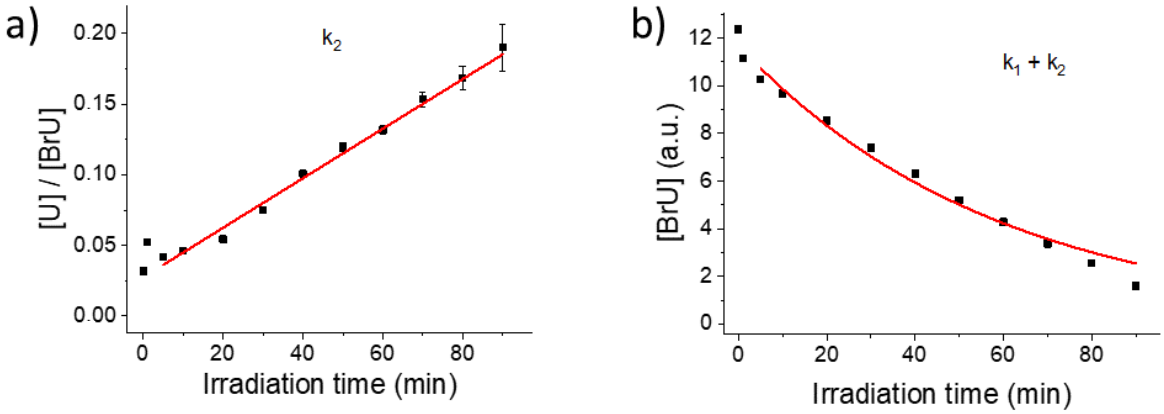

Figure 5.3 – (a) Ratio of the concentrations *[U]* and *[BrU]* plotted against the irradiation time *t* fit linearly to determine k_2 from the slope. (b) Concentration *[BrU]* plotted as a function of the irradiation time *t* and fit with an exponential decay curve to determine k_1 and k_2 from the decay constant.

The reaction rates k_1 and k_2 have been determined at a fixed laser fluence for different repetition rates of the laser. The error bars of the reaction rates *k1* and *k2* originate from the fit presented in Figure 5.3 (see Figure 5.4). The reaction rate k_1 decreases significantly with higher laser repetition rates. At higher laser repetition rates, the time between two subsequent pulses is shorter. In consequence, there is less time following a laser pulse in which the 5BrU can adsorb on the cleaned surface before the AuNP is illuminated again. Therefore, the coverage of 5BrU on the AuNP surface during the pulse is lower at higher laser repetition rates as the adsorption time for 5BrU is shortened. Lower concentrations of 5BrU on the AuNPs, i.e. in the areas of the highest temperatures, result in decreasing reaction rates for k_1. This trend is in accordance with results published previously [21]. Nevertheless, for k_2, no dependency on the repetition rate has been observed. k_2 represents the C-Br bond cleavage leaving the U ring intact. The C-Br bond of 5BrU is a predetermined breaking point of the molecule and can be efficiently cleaved by the dissociative attachment of low energy electrons, and it is the first bond to break at elevated temperatures [38]. However, both processes might occur as well in the vicinity of the AuNP surface and do not require adsorption of the molecules. Furthermore, the conditions directly on the AuNP surface are extreme in terms of temperature and pressure. Hence, it is unlikely that in adsorbed 5BrU molecules, only the C-Br bond will be cleaved under laser irradiation prior desorption leaving the U ring intact.

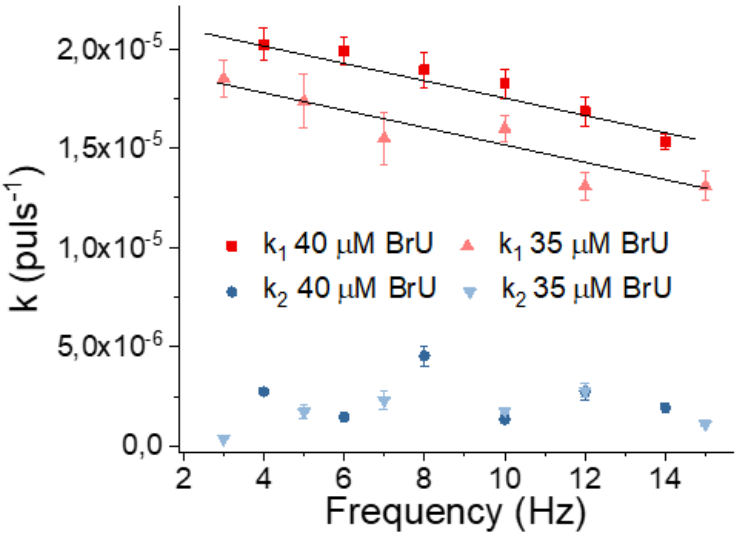

Figure 5.4 – Reaction rates *k1* (red) and *k2* (blue) of 5BrU as a function of the laser repetition rate for two different initial concentrations of 5BrU (dark and light symbols, respectively). Black lines are plotted as guides for the eye.

Moreover, the reaction rates have been determined as a function of the maximum laser fluence (see Figure 5.5a)). For this purpose, the distance of the surface of the AuNP/5BrU solution to the focus of the laser beam was varied using a mechanical stage. Due to this setup, the photon fluence can be varied while keeping the power of the laser pulses constant. Even though the laser pulses have a Gaussian shape and the divergent laser beam widens during the passage through the AuNP/5BrU solution leading to a spatially inhomogeneously distributed fluence, the maximum laser fluence is proportional to the average fluence in the solution. The reaction rates k_1 and k_2 show the same behaviour as a function of the laser fluence, whereas k_1 is typically almost one order of magnitude higher than k_2. Up to a laser fluence of around 10^{13} W/m^2, the reaction rates increase with the laser fluence; however, for higher fluences (> 10^{13} W/m^2), the reaction rates decrease. A threshold, where k_2 is significantly increased with respect to k_1 due to an enhanced generation of thermionic electrons as predicted previously by Pyatenko et al., has not been observed [20]. In the predictions of the threshold, nanoparticles of constant size have been assumed; however, the size of the generated nanoparticle fragments significantly depends on the laser fluences. The size of the nanoparticles influences strongly the absorption of the AuNPs at 532 nm due to

the LSPR. In Figure 5.5b), the absorbance at a wavelength of 532 nm has been plotted against the laser power, showing a decrease in the absorbance with an increase in the laser fluence reaching a minimum at ~10^{13} W/m^2 as well. In general, small AuNPs exhibit LSPRs with lower intensities, which are centered at comparably lower wavelength. The decrease of the LSPRs as a function of the laser power indicates a stronger fragmentation of the AuNPs at higher laser powers. Nevertheless, the resulting decreased absorption at 532 nm results in a lower energy absorption by the AuNP solution, limiting the heating of the AuNPs and leading to stagnating or even reduction of the reaction rates at high fluences. At high laser fluences, especially for the irradiation of larger AuNPs, the ignition of plasmas has been observed [39]. Since the plasmas occur statistically, their role in the decomposition of the AuNPs and the molecules could not be evaluated.

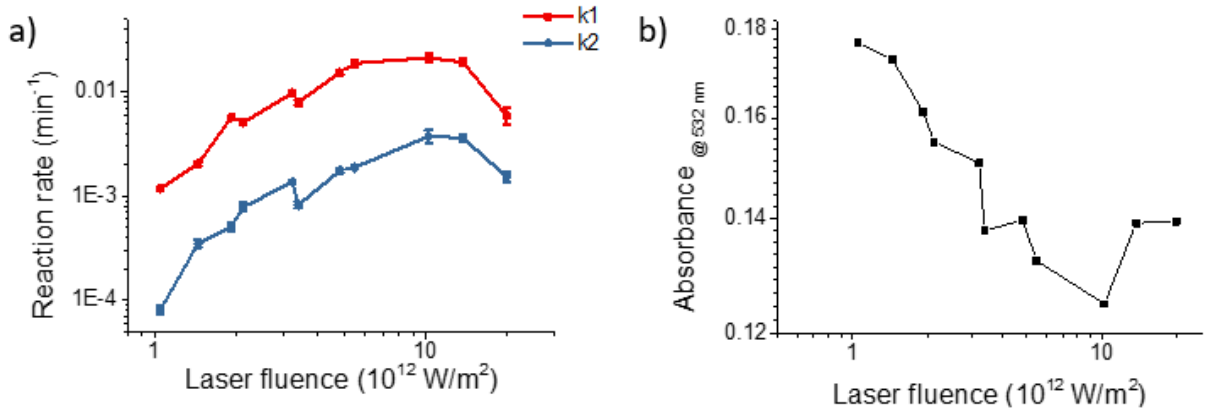

Figure 5.5 – (a) Reaction rates *k1* and *k2* plotted as a function of the laser fluence. (b) Absorbance of *AuNP/5BrU* solution at 532 nm after 20 min irradiation plotted against the laser fluence.

Although the LSPR absorption decreases with higher laser fluence, the reaction rates increase up to a maximum fluence of 10^{13} W/m^2. This might be explained by an increased surface area of the smaller AuNPs, since the number of gold atoms in the solution remains constant under the irradiation. It is also possible that higher temperature around the AuNPs might be responsible for the higher reaction rates. In order to determine the surface area A_S of the AuNPs, the size distribution of the AuNPs after an irradiation for 20 min has been determined by AFM for six different laser fluences. Figure 5.6a) and Figure 5.6b) show typical AFM images of the AuNPs after irradiation. The diameter of the AuNPs has been determined from the

height of the AuNPs, and the normalized size distributions of the AuNPs are shown in Figure 5.6c). 500–3000 AuNPs have been analyzed at each of the laser fluences studied. In all cases, the size of the AuNPs after the irradiation was reduced from 40 nm to below 10 nm. With the knowledge of the normalized size distribution of the AuNPs, the overall surface area of the AuNPs in the solution can be calculated using the following equation:

$$A_S = \frac{V_{gold}}{\sum P(r) \cdot V(r)} \cdot 4\pi \cdot \sum P(r) \cdot r^2 \qquad [5.10]$$

where V_{gold} is the total volume of the AuNPs in the solution, r is the radius of the AuNPs, $P(r)$ is the percentage of AuNPs with a radius r in the solution determined from the histograms shown in Figure 5.6c) and SI 3 and $V(r)$ is the volume of an AuNP with a radius r. In Figure 5.6d), the surface area is plotted as a function of the laser fluence revealing an increase in the surface area with the laser fluence. The presented error bars originate from the statistical error of the AuNP counting (see the S.I. 5.9.3).

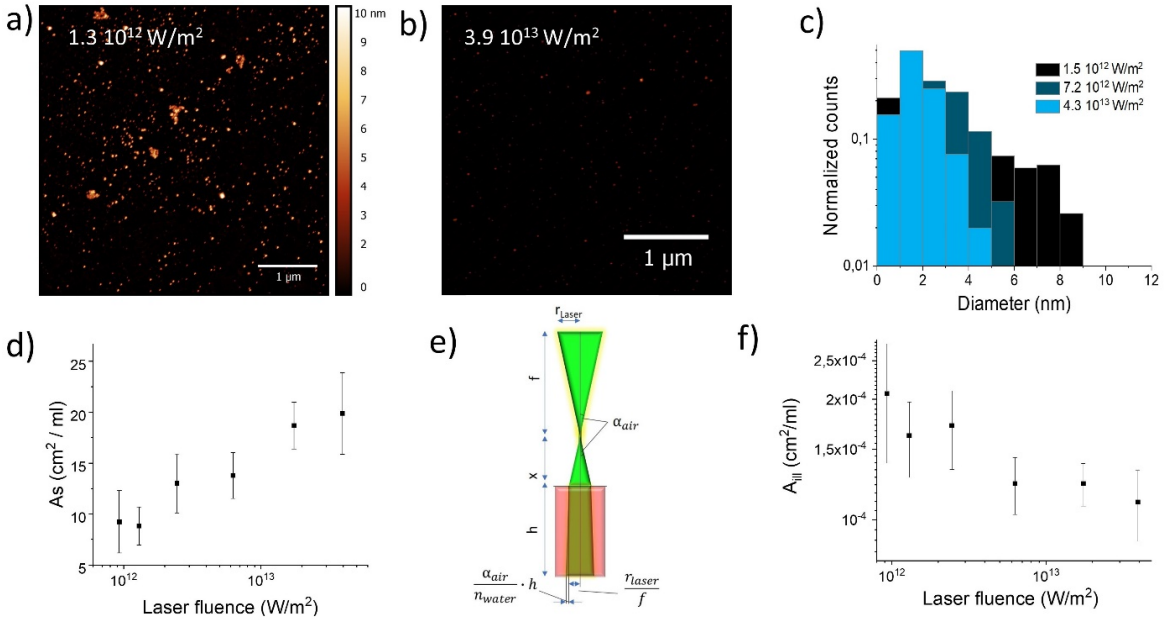

Figure 5.6 – AFM image of AuNPs dried on a mica substrate illuminated for 20 min with a maximum laser fluence of (a) 1.3 x 10^{12} W/m^2 and (b) 3.9 x 10^{13} W/m^2. (c) Normalized size distribution of AuNPs irradiated using different laser fluences. All histograms are presented individually in S.I. 5.9.2. (d) Surface area of the irradiated AuNPs determined using equation [5.10] as a function of the laser fluence. (e) Sketch of the laser beam propagation after passing the focusing lens according to geometrical optics. (f) Illuminated surface area during one laser pulse as a function of the laser fluence after irradiation for 20 min.

It should be noted that at higher laser fluences, a smaller fraction of the solution is illuminated. In consequence, the illuminated surface area A_{ill} of the AuNPs needs to be determined to evaluate the effect of the surface area on the reaction rates. For this purpose, the illuminated volume V_{ill} for certain laser fluences has been calculated using basic geometrical optics assuming a simplified model of the laser beam path. The beam path in the solution has a truncated cone shape. A sketch of the beam propagation after passing the final focusing lens is presented in Figure 5.6e). The illuminated volume can be calculated by:

$$V_{ill} = \frac{\pi \cdot h}{3}\left[\left(\frac{x}{f}\cdot r_{Laser}\right)^2 + \left(\frac{x}{f}\cdot r_{Laser}\right)\left(\frac{r_{Laser}}{f\cdot n_{water}}\cdot h + \frac{x}{f}\cdot r_{Laser}\right) + \left(\frac{r_{Laser}}{f\cdot n_{water}}\cdot h + \frac{x}{f}\cdot r_{Laser}\right)^2\right] \quad [5.11]$$

From the ratio of V_{ill} to the total volume of the solution V_{total}, the illuminated area A_{ill} can be calculated by using equation [5.12],

$$A_{ill} = \frac{V_{ill}}{V_{total}} \cdot A_S \quad [5.12]$$

In Figure 5.6f), A_{ill} is plotted as a function of the laser fluence, revealing a decrease in A_{ill} with the fluence, although the relative error of the calculation is large. Hence, the increased reaction rates at higher laser fluences might not be solely explained by an increased surface area of the illuminated AuNPs.

Therefore, the absorbed heat Q_{abs} of an individual AuNP during a laser pulse has been calculated from the absorption cross section σ_{abs} of the irradiated AuNPs and the laser fluence I,

$$Q_{abs} = \sigma_{abs} \cdot I \quad [5.13]$$

For small nanoparticles, mainly the absorption is contributing to the extinction and the scattering can be neglected. Thus, the UV-Vis data presented in Figure 5.5b) have been used to estimate the absorption cross section σ_{abs} of the irradiated AuNP solution by using the Lambert-Beer law,

$$Abs = l \cdot \sigma_{abs} \cdot N_{AuNP} \quad [5.14]$$

The number of AuNPs per unit volume N_{AuNP} of the irradiated AuNP solution has been determined by:

$$N_{AuNP} = \frac{V_{AuNP\ 40\ nm}}{\sum P(r) \cdot V(r)} \cdot N_{AuNP\ 40nm} \quad [5.15]$$

where $V_{AuNP\ 40\ nm}$ is the volume of an AuNP with a diameter of 40 nm and $N_{AuNP\ 40\ nm}$ is the initial number of 40 nm AuNPs per unit volume in the solution prior to irradiation.

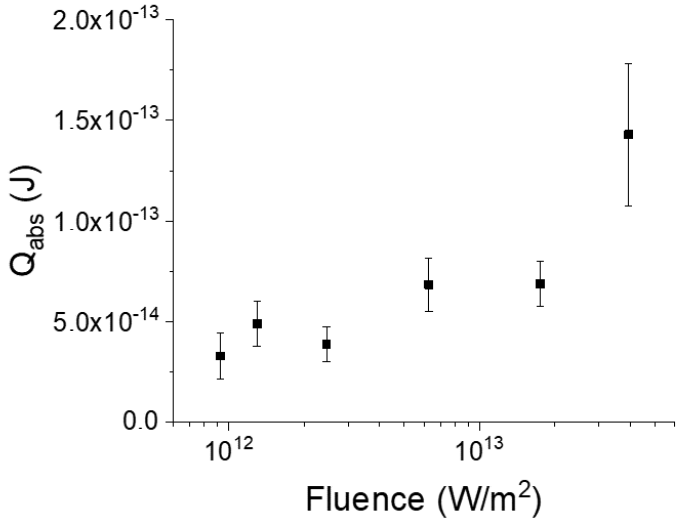

Figure 5.7 – Heat absorbed by a single AuNP in one 16 mJ laser pulse plotted as a function of the laser fluence.

In Figure 5.7, Q_{abs} is plotted as a function of the laser fluence revealing an increase of Q_{abs} with the laser fluence leading to a higher temperature of the individual AuNPs. Hence, the increase in the reaction rates with the laser fluence might be caused by an increased temperature around the AuNPs and possibly by an increased generation of reactive species, such as low energy electrons, even though the total absorption of light in the solution (see Figure 5.5b)) and the illuminated surface area (see Figure 5.6f)) are smaller. However, the time between two laser pulses illuminating the same AuNP is longer for a smaller illuminated area, and furthermore, the temperature gradient leads to migration of molecules toward the AuNP surface [40], thus, the effect of adsorption on the decomposition rate cannot be neglected in this context.

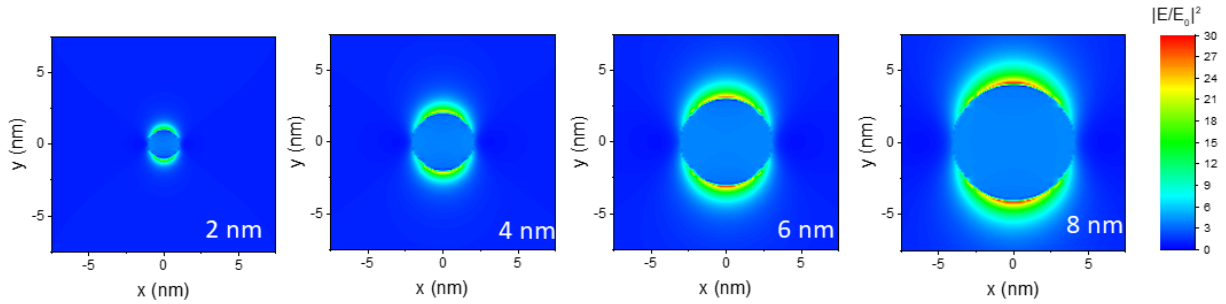

Figure 5.8 – FDTD-calculation of the electrical field enhancement $|\boldsymbol{E/E_0}|^2$ of AuNPs with a size of 2 nm, 4 nm, 6 nm and 8 nm, respectively, in an aqueous medium at a wavelength of 532 nm.

In order to evaluate the possible impact of multi-photon processes, the enhancement of the electrical field $|E/E_0|^2$ around the AuNPs has been determined by FDTD simulations. The simulations have been performed for spherical AuNPs with a diameter between 2 nm and 8 nm, which are typically generated under the present experimental conditions. In Figure 5.8, $|E/E_0|^2$ is plotted in the x–y plane crossing the center of the particle. For AuNPs with a diameter of 2 nm, the intensity enhancement is comparably small, not exceeding a factor of ~15 at the spots with the highest enhancement. Furthermore, the spots with a high enhancement are highly localized close to the particle surface. At a distance of around 1 nm from the surface, a significant enhancement of $|E/E_0|^2$ is no longer observable. With an increase in the diameter of the AuNPs, the intensity enhancement in the vicinity of the particles is increased. However, even for AuNPs with a diameter of 8 nm, the maximum intensity enhancement does not exceed a factor of 30. Irradiation of a 5BrU solution for several hours at high laser fluences in the absence of AuNPs did not lead to a change in the π-π* resonance (see SI 1). For uracil and thymine, a threshold multiphoton excitation leading to the fragmentation of the molecules has been observed at energies involving at least three 532 nm (2.33 eV) photons [41], [42]. In consequence, it is very unlikely to observe a significant contribution of multiphoton effects due to the laser irradiation in the present experiments, as the volumes with a comparably high enhancement are very localized and correlate with the volumes where the highest temperatures will also occur; thus, a thermal decay of possible photoproducts is likely.

5.5. Conclusion

In summary, the kinetics of two decomposition pathways of 5BrU adsorbed on AuNPs induced by pulsed laser illumination have been tracked by UV–Vis spectroscopy and reaction rates have been determined using a kinetic model. The decomposition rates for the fragmentation of the 5BrU ring structure depend on the fluence, the repetition rate of the laser, and the starting concentration of 5BrU. At higher laser fluences, the AuNPs are decomposed and the surface area is increased, also leading to higher temperatures. However, on the other hand, the irradiated volume is decreased and the plasmonic response is significantly lowered. Hence, these opposing effects lead to a trade-off limiting the decomposition rates. The cleavage of the C–Br bond leaving the residual molecule intact is most likely independent of the adsorption of the molecules on the AuNPs. This process is probably electron or thermally induced, and multiphoton excitation processes are very unlikely. As the irradiation parameters are interlinked with the optical and thermal properties of the generated AuNP substrates, the tunability of the reaction kinetics of the system is only limited.

5.6. Author's contributions

T.S.M. and R.S., first authors, contributed equally.

5.7. Acknowledgements

The authors acknowledge the financial support from Deutsche Forschungsgemeinschaft (Project No.230710387), Fundação para a Ciência e a Tecnologia (FCT-MCTES), Radiation Biology and Biophysics Doctoral Training Programme (RaBBiT, PD/00193/2012); Applied Molecular Biosciences Unit - UCIBIO (UIDB/04378/2020) and CEFITEC Unit (UIDB/00068/2020); and scholarship grant number SFRH/BD/106032/2015 to Telma S. Marques.

5.8. References

[1] J. R. Mejía-Salazar and O. N. Oliveira, “Plasmonic Biosensing,” *Chem. Rev.*, vol. 118, no. 20, pp. 10617–10625, 2018, doi: 10.1021/acs.chemrev.8b00359.

[2] K. A. Willets and R. P. Van Duyne, “Localized Surface Plasmon Resonance Spectroscopy and Sensing,” *Annu. Rev. Phys. Chem.*, vol. 58, no. 1, pp. 267–297, 2007, doi: 10.1146/annurev.physchem.58.032806.104607.

[3] Y. Zhang *et al.*, “Surface-Plasmon-Driven Hot Electron Photochemistry,” *Chemical Reviews*, vol. 118, no. 6. American Chemical Society, pp. 2927–2954, 2018, doi: 10.1021/acs.chemrev.7b00430.

[4] N. S. Abadeer and C. J. Murphy, “Recent Progress in Cancer Thermal Therapy Using Gold Nanoparticles,” *Journal of Physical Chemistry C*, vol. 120, no. 9. American Chemical Society, pp. 4691–4716, 2016, doi: 10.1021/acs.jpcc.5b11232.

[5] K. Haume *et al.*, “Gold nanoparticles for cancer radiotherapy: a review,” *Cancer Nanotechnol.*, vol. 7, no. 1, 2016, doi: 10.1186/s12645-016-0021-x.

[6] D. Lin *et al.*, “Highly Efficient Destruction of Amyloid-β Fibrils by Femtosecond Laser-Induced Nanoexplosion of Gold Nanorods,” *ACS Chem. Neurosci.*, vol. 7, no. 12, pp. 1728–1736, 2016, doi: 10.1021/acschemneuro.6b00244.

[7] E. Cortés, “Efficiency and Bond Selectivity in Plasmon-Induced Photochemistry,” *Adv. Opt. Mater.*, vol. 5, no. 15, p. 1700191, 2017, doi: 10.1002/adom.201700191.

[8] R. Schürmann, K. Ebel, C. Nicolas, A. R. Milosavljević, and I. Bald, “Role of Valence Band States and Plasmonic Enhancement in Electron-Transfer-Induced Transformation of Nitrothiophenol,” *J. Phys. Chem. Lett.*, vol. 10, no. 11, pp. 3153–3158, 2019, doi: 10.1021/acs.jpclett.9b00848.

[9] Z. Qin and J. C. Bischof, “Thermophysical and biological responses of gold nanoparticle laser heating,” *Chemical Society Reviews*, vol. 41, no. 3. pp. 1191–1217, 2012, doi: 10.1039/c1cs15184c.

[10] S. Hashimoto, D. Werner, and T. Uwada, “Studies on the interaction of pulsed lasers with plasmonic gold nanoparticles toward light manipulation, heat management, and nanofabrication,” *Journal of Photochemistry and Photobiology C: Photochemistry Reviews*, vol. 13, no. 1. pp. 28–54, 2012, doi: 10.1016/j.jphotochemrev.2012.01.001.

[11] M. Strasser, K. Setoura, U. Langbein, and S. Hashimoto, “Computational Modeling of Pulsed Laser-Induced Heating and Evaporation of Gold Nanoparticles,” *J. Phys. Chem. C*, vol. 118, no. 44, pp. 25748–25755, 2014, doi: 10.1021/jp508316v.

[12] G. González-Rubio, A. Guerrero-Martínez, and L. M. Liz-Marzán, “Reshaping, Fragmentation, and Assembly of Gold Nanoparticles Assisted by Pulse Lasers,” *Acc. Chem. Res.*, vol. 49, no. 4, pp. 678–686, 2016, doi: 10.1021/acs.accounts.6b00041.

[13] A. R. Ziefuß *et al.*, “Laser Fragmentation of Colloidal Gold Nanoparticles with High-Intensity Nanosecond Pulses is Driven by a Single-Step Fragmentation Mechanism with a Defined Educt Particle-Size Threshold,” *J. Phys. Chem. C*, vol. 122, no. 38, pp. 22125–22136, 2018, doi: 10.1021/acs.jpcc.8b04374.

[14] D. Zhang, B. Gökce, and S. Barcikowski, “Laser Synthesis and Processing of Colloids: Fundamentals and Applications,” *Chem. Rev.*, vol. 117, no. 5, pp. 3990–4103, 2017, doi: 10.1021/acs.chemrev.6b00468.

[15] S. Hashimoto, T. Katayama, K. Setoura, M. Strasser, T. Uwada, and H. Miyasaka, “Laser-driven phase transitions in aqueous colloidal gold nanoparticles under high pressure: Picosecond pump-probe study,” *Phys. Chem. Chem. Phys.*, vol. 18, no. 6, pp. 4994–5004, 2016, doi: 10.1039/c5cp07395b.

[16] K. Metwally, S. Mensah, and G. Baffou, “Fluence Threshold for Photothermal Bubble Generation Using Plasmonic Nanoparticles,” *J. Phys. Chem. C*, vol. 119, no. 51, pp. 28586–28596, 2015, doi: 10.1021/acs.jpcc.5b09903.

[17] S. Wang, L. Fu, Y. Zhang, J. Wang, and Z. Zhang, “Quantitative Evaluation and Optimization of Photothermal Bubble Generation around Overheated Nanoparticles Excited by Pulsed Lasers,” *J. Phys. Chem. C*, vol. 122, no. 42, pp. 24421–24435, 2018,

doi: 10.1021/acs.jpcc.8b07672.

[18] S. J. Chadwick, D. Salah, P. M. Livesey, M. Brust, and M. Volk, “Singlet oxygen generation by laser irradiation of gold nanoparticles,” *J. Phys. Chem. C*, vol. 120, no. 19, pp. 10647–10657, 2016, doi: 10.1021/acs.jpcc.6b02005.

[19] K. Yamada, K. Miyajima, and F. Mafuné, “Thermionic emission of electrons from gold nanoparticles by nanosecond pulse-laser excitation of interband,” *J. Phys. Chem. C*, vol. 111, no. 30, pp. 11246–11251, 2007, doi: 10.1021/jp0730747.

[20] A. Pyatenko, M. Yamaguchi, and M. Suzuki, “Mechanisms of Size Reduction of Colloidal Silver and Gold Nanoparticles Irradiated by Nd:YAG Laser,” *J. Phys. Chem. C*, vol. 113, no. 21, pp. 9078–9085, 2009, doi: 10.1021/jp808300q.

[21] R. Schürmann and I. Bald, “Decomposition of DNA Nucleobases by Laser Irradiation of Gold Nanoparticles Monitored by Surface-Enhanced Raman Scattering,” *J. Phys. Chem. C*, vol. 120, no. 5, pp. 3001–3009, 2016, doi: 10.1021/acs.jpcc.5b10564.

[22] R. Schürmann and I. Bald, “Effect of adsorption kinetics on dissociation of DNA-nucleobases on gold nanoparticles under pulsed laser illumination,” *Physical Chemistry Chemical Physics*, vol. 19, no. 17. pp. 10796–10803, 2017, doi: 10.1039/C6CP08433H.

[23] Y. Takeda, T. Kondow, and F. Mafuné, “Selective decomposition of nucleic acids by laser irradiation on probe-tethered gold nanoparticles in solution,” *Phys. Chem. Chem. Phys.*, vol. 13, no. 2, pp. 586–592, 2011, doi: 10.1039/c0cp00770f.

[24] F. Sauvage *et al.*, “Nanomaterials to avoid and destroy protein aggregates,” *Nano Today*. Elsevier B.V., p. 100837, 2020, doi: 10.1016/j.nantod.2019.100837.

[25] Y. Takeda, T. Kondow, and F. Mafuné, “Degradation of protein in nanoplasma generated around gold nanoparticles in solution by laser irradiation,” *J. Phys. Chem. B*, vol. 110, no. 5, pp. 2393–2397, 2006, doi: 10.1021/jp058204v.

[26] Y. Takeda, F. Mafuné, and T. Kondow, “Selective degradation of proteins by laser irradiation onto gold nanoparticles in solution,” *J. Phys. Chem. C*, vol. 113, no. 13, pp.

5027–5030, 2009, doi: 10.1021/jp809438d.

[27] T. Tsuji *et al.*, “Stabilizer-Concentration Effects on the Size of Gold Submicrometer-Sized Spherical Particles Prepared Using Laser-Induced Agglomeration and Melting of Colloidal Nanoparticles,” *J. Phys. Chem. C*, vol. 122, no. 37, pp. 21659–21666, 2018, doi: 10.1021/acs.jpcc.8b05911.

[28] M. Aioub and M. A. El-Sayed, “A Real-Time Surface Enhanced Raman Spectroscopy Study of Plasmonic Photothermal Cell Death Using Targeted Gold Nanoparticles,” *J. Am. Chem. Soc.*, vol. 138, no. 4, pp. 1258–1264, 2016, doi: 10.1021/jacs.5b10997.

[29] E. Boulais, R. Lachaine, A. Hatef, and M. Meunier, “Plasmonics for pulsed-laser cell nanosurgery: Fundamentals and applications,” *J. Photochem. Photobiol. C Photochem. Rev.*, vol. 17, pp. 26–49, 2013, doi: 10.1016/j.jphotochemrev.2013.06.001.

[30] M. D. Prados *et al.*, “Phase III randomized study of radiotherapy plus procarbazine, lomustine, and vincristine with or without BUdR for treatment of anaplastic astrocytoma: Final report of RTOG 9404,” *Int. J. Radiat. Oncol. Biol. Phys.*, vol. 58, no. 4, pp. 1147–1152, 2004, doi: 10.1016/j.ijrobp.2003.08.024.

[31] J. Rak *et al.*, “Mechanisms of Damage to DNA Labeled with Electrophilic Nucleobases Induced by Ionizing or UV Radiation,” *Journal of Physical Chemistry B*, vol. 119, no. 26. American Chemical Society, pp. 8227–8238, 2015, doi: 10.1021/acs.jpcb.5b03948.

[32] M. Zdrowowicz, B. Michalska, A. Zylicz-Stachula, and J. Rak, “Photoinduced single strand breaks and intrastrand cross-links in an oligonucleotide labeled with 5-bromouracil,” *J. Phys. Chem. B*, vol. 118, no. 19, pp. 5009–5016, 2014, doi: 10.1021/jp500192z.

[33] H. Abdoul-Carime, M. A. Huels, F. Brüning, E. Illenberger, and L. Sanche, “Dissociative electron attachment to gas-phase 5-bromouracil,” *J. Chem. Phys.*, vol. 113, no. 7, pp. 2517–2521, 2000, doi: 10.1063/1.1306654.

[34] R. Schürmann and I. Bald, “Real-time monitoring of plasmon induced dissociative

electron transfer to the potential DNA radiosensitizer 8-bromoadenine," *Nanoscale*, vol. 9, no. 5, pp. 1951–1955, 2017, doi: 10.1039/c6nr08695k.

[35] R. Schürmann, K. Tanzer, I. Dąbkowska, S. Denifl, and I. Bald, "Stability of the Parent Anion of the Potential Radiosensitizer 8-Bromoadenine Formed by Low-Energy (<3 eV) Electron Attachment," *J. Phys. Chem. B*, vol. 121, no. 23, pp. 5730–5734, 2017, doi: 10.1021/acs.jpcb.7b02130.

[36] D. B. DUNN and J. D. SMITH, "Effects of 5-halogenated uracils on the growth of Escherichia coli and their incorporation into deoxyribonucleic acids.," *Biochem. J.*, vol. 67, no. 3, pp. 494–506, 1957, doi: 10.1042/bj0670494.

[37] G. D. Fasman, *CRC Handbook of Biochemistry and Molecular Biology, 9 Volume Set: Georrge D. Fasman: Amazon.com: Books*, 3rd ed. 2019.

[38] J. C. Tully, "Mode-selective control of surface reactions," *Science*, vol. 312, no. 5776. pp. 1004–1005, 2006, doi: 10.1126/science.1126341.

[39] A. A. Serkov, P. G. Kuzmin, I. I. Rakov, and G. A. Shafeev, "Influence of laser-induced breakdown on the fragmentation of gold nanoparticles in water," *Quantum Electron.*, vol. 46, no. 8, pp. 713–718, 2016, doi: 10.1070/qel16094.

[40] M. Enders, S. Mukai, T. Uwada, and S. Hashimoto, "Plasmonic Nanofabrication through Optical Heating," *J. Phys. Chem. C*, vol. 120, no. 12, pp. 6723–6732, 2016, doi: 10.1021/acs.jpcc.5b11762.

[41] B. Barc *et al.*, "Multi-photon ionization and fragmentation of uracil: Neutral excited-state ring opening and hydration effects," *J. Chem. Phys.*, vol. 139, no. 24, 2013, doi: 10.1063/1.4851476.

[42] R. Pandey *et al.*, "Threshold behavior in metastable dissociation of multi-photon ionized thymine and uracil," *Chem. Phys. Lett.*, vol. 684, pp. 233–238, 2017, doi: 10.1016/j.cplett.2017.06.051.

5.9. Supporting Information

Kinetics of Molecular Decomposition under Irradiation of Gold Nanoparticles with nanosecond Laser Pulses – A 5-Bromouracil case study

Telma S. Marques[c,f], Robin Schürmann, [a,b] Kenny Ebel,[a,b], Christian Heck [a], Małgorzata A. Śmiałek,[c,d] Sam Eden,[c] Nigel Mason,[c,e] and Ilko Bald*[a,b]

[a] Physical Chemistry, Institute of Chemistry,
University of Potsdam
Karl-Liebknecht-Str. 24-25, 14476 Potsdam-Golm, Germany

[b] Department of Analytical Chemistry
BAM, Federal Institute of Material Research and Testing
Richard-Willstätter-Str. 11, 12489 Berlin, Germany

[c] Department of Physical Sciences, The Open University, Walton Hall, MK7 6AA, Milton Keynes, UK

[d] Department of Control and Power Engineering, Faculty of Ocean Engineering and Ship Technology, Gdansk University of Technology, Gabriela Narutowicza 11/12, 80-233 Gdansk, Poland

[e] School of Physical Sciences, University of Kent at Canterbury CT2 7NH, United Kingdom

[f] CEFITEC, Departamento de Física, Faculdade de Ciências e Tecnologia, Universidade Nova de Lisboa, 2829-516 Caparica, Portugal

In the SI are presented all the complete derivation of the reaction kinetics, irradiation of 5BrU in the absence of AuNPs, and error calculation.

S.I. 5.9.1 Complete derivation of the reaction kinetics

$$BrU \xrightarrow{k1} small\ fragments \qquad (1)$$

$$BrU \xrightarrow{k2} U \qquad (2)$$

$$U \xrightarrow{k3} small\ fragments \qquad (3)$$

Based on equation (1) and (2) the decomposition of 5BrU is following a (pseudo-) first order reaction that can be described by the following equation:

$$\frac{d[BrU]}{dt} = -k_1[BrU] - k_2[BrU] \qquad (4)$$

According to equation (2) and (3) the generation and decomposition of *U* can be described by:

$$\frac{d[U]}{dt} = -k_3[U] + k_2[BrU] \qquad (5)$$

From equation (4) we get for the concentration of *[BrU]* after an irradiation time *t*:

$$[BrU] = [BrU]_0 e^{-(k_1+k_2)t} \qquad (6)$$

Where $[BrU]_0$ is the initial concentration of *5BrU* before the irradiation. If we insert this expression for *[BrU]* into equation (5) we get:

$$\frac{d[U]}{dt} + k_3[U] = k_2[BrU]_0 e^{-(k_1+k_2)t} \qquad (7)$$

By using the integral method, which allows to solve differential equations of the type:

$\frac{dy}{dx} + f(x)y = g(x)$ by multiplication with $e^{\int f(x)dx} = e^{\int k_3 dt} = e^{k_3 t}$, we get:

$$e^{k_3 t}\frac{d[U]}{dt} + e^{k_3 t}k_3[U] = k_2[BrU]_0 e^{-(k_1+k_2)t} e^{k_3 t} \qquad (8)$$

Which can be rearranged to:

$$\frac{d([U]e^{k_3 t})}{dt} = k_2[BrU]_0\, e^{-(k_1+k_2-k_3)t} \qquad (9)$$

by using $\frac{d([U]e^{k_3 t})}{dt} = e^{k_3 t}\frac{d[U]}{dt} = e^{k_3 t}k_3[U]$. Thus the integration of the equation (9):

$$\int_{[U_0]e^0}^{[U]e^{k_3 t}} d([U]e^{k_3 t}) = k_2[BrU]_0 \int_0^t e^{-(k_1+k_2-k_3)t} dt \qquad (10)$$

gives us:

$$[U]e^{k_3 t} - [U_0] = \frac{k_2[BrU]_0}{k_3 - k_1 - k_2}\left(e^{-(k_1+k_2-k_3)t} - 1\right) \qquad (11)$$

With $[U_0] = 0$, since there has been initially no *U* in the solution, we get for *[U]*:

$$[U] = \frac{k_2[BrU]_0}{k_3 - k_1 - k_2}\left(e^{-(k_1+k_2)t} - e^{-k_3 t}\right) \quad (12)$$

Consequently, the ratio of *[U]* and be *[BrU]* can be determined using equation (6) and (12):

$$\frac{[U]}{[BrU]} = \frac{k_2}{k_3 - k_1 - k_2}\left(1 - e^{-(k_3-k_1-k_2)t}\right) \quad (13)$$

By using the Taylor expansion: $e^x \approx 1 + x$ we can simplify the expression for short illumination times *t* to:

$$\frac{[U]}{[BrU]} \approx k_2 t \qquad (14)$$

S.I. 5.9.2 Irradiation of 5BrU in the absence of AuNPs

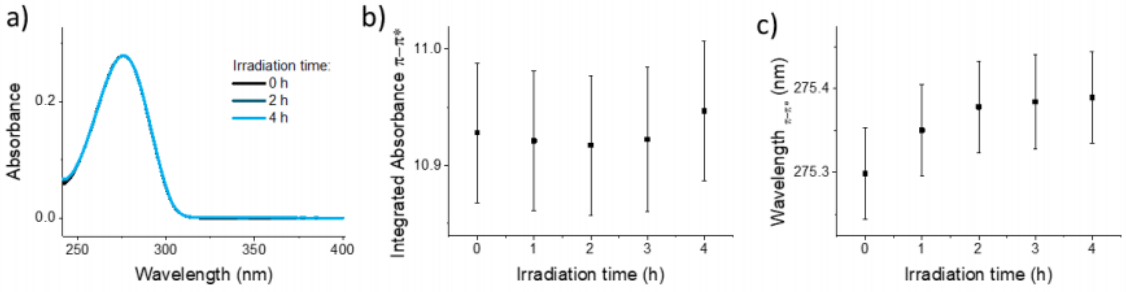

S.I. 5.1 – a) UV-Vis spectra of 5BrU solution irradiated with a focused 532 nm ns laser pulses with a repetition rate of 15 Hz with a maximum laser fluence of 4×10^{13} W/m^2 after 0 h, 2 h and 4 h of irradiation. b) Integrated Absorbance of the π-π* resonance of 5BrU as a function of the illumination time. c) Center wavelength of the π-π* resonance as a function of the illumination time.

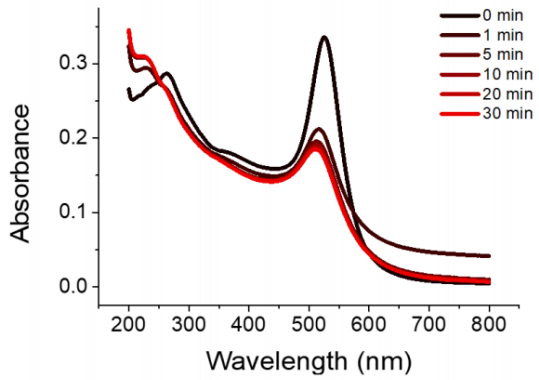

S.I. 5.2 – Exemplary set of UV-Vis spectra of an AuNPs solution irradiated with a focused 532 nm ns laser pulses with a repetition rate of 15 Hz with a maximum laser fluence of 3.4x10^{12} W/m^2 used as background correction.

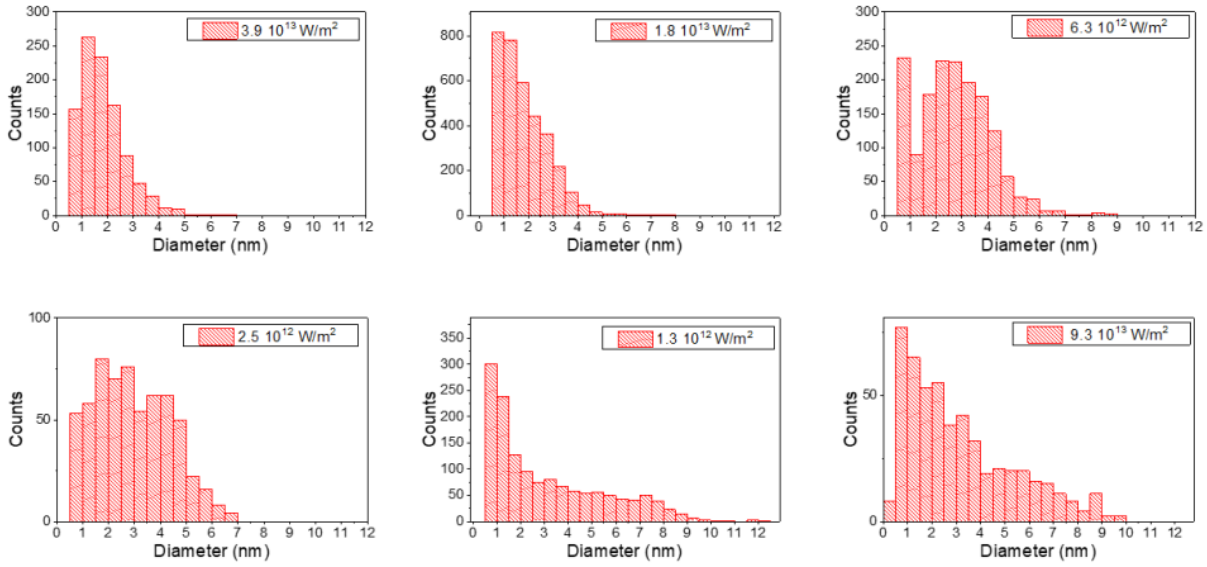

S.I. 5.3 – Histograms of the AuNPs sizes after laser illumination with different fluences.

S.I. 5.9.3 Error calculation

The error of the surface area of the irradiated surface area A_s has been calculated based on the error of *P(r)*, which is given by:

$$\Delta P(r) = \frac{\Delta N(r)}{N_{ges}} + \frac{N(r)}{{N_{ges}}^2} \cdot \Delta N_{ges} \qquad (15)$$

With:

$$N = \sqrt{N} \qquad (16)$$

Thus we get:

$$\Delta A_S = \left[\sum_r \left| \frac{\partial}{\partial P(r)} \frac{V_{gold}}{\sum_r P(r) \cdot \frac{4}{3} \cdot \pi \cdot r^3} \cdot \sum_r 4\pi \cdot P(r) \cdot r^2 \right|^2 \cdot \Delta P(r)^2 \right]^{1/2} \qquad (17)$$

Which can be written as:

$$\Delta A_S = \left[\left[\frac{V_{gold} \cdot \sum_r \frac{4}{3} \cdot \pi \cdot r^3 \cdot \Delta P(r)}{\left(\sum_r P(r) \cdot \frac{4}{3} \cdot \pi \cdot r^3 \right)^2} \cdot \sum_r 4\pi \cdot P(r) \cdot r^2 \right]^2 + \left[\frac{V_{gold}}{\sum_r P(r) \cdot \frac{4}{3} \cdot \pi \cdot r^3} \cdot \sum_r 4\pi \cdot r^2 \cdot \Delta P(r) \right]^2 \right]^{1/2} \qquad (18)$$

The error for the illuminated surface area of the AuNPs is given by:

$$\Delta A_{ill} = \frac{V_{ill}}{V_{total}} \cdot \Delta A_S \qquad (19)$$

The error for the absorbed heat by an individual AuNP:

$$Q = \frac{Abs \cdot \sum_r P(r) \cdot \frac{4}{3} \cdot \pi \cdot r^3}{V_{gold} \cdot N_{AuNP\ 40nm} \cdot l} \cdot I \qquad (20)$$

has been calculated by:

$$\Delta Q = \left[\sum_r \left| \frac{\partial}{\partial P(r)} \frac{Abs \cdot \sum_r P(r) \cdot \frac{4}{3} \cdot \pi \cdot r^3}{V_{gold} \cdot N_{AuNP\ 40nm} \cdot l} \cdot I \right|^2 \cdot \Delta P(r)^2 \right]^{\frac{1}{2}} = \frac{Abs \cdot \sum_r \frac{4}{3} \cdot \pi \cdot r^3 \cdot \Delta P(r)}{V_{gold} \cdot N_{AuNP\ 40nm} \cdot l} \cdot I \qquad (21)$$

S.I. Table 5.1 – Ratio of *[U]* and *[BrU]* as a function of the irradiation time. Data presented in Figure 5.3 a).

Irradiation time (min)	0	1	5	10	20	30
[U]/[BrU]	0.0319	0.0524	0.0417	0.0462	0.0545	0.0749
Δ[U]/[BrU]	0.0017	0.0019	0.0021	0.0019	0.0022	0.0022
Irradiation time (min)	40	50	60	70	80	90
[U]/[BrU]	0.1006	0.1192	0.1318	0.1534	0.1685	0.1899
Δ[U]/[BrU]	0.0022	0.003	0.0033	0.0052	0.0081	0.0167

S.I. Table 5.2 – Concentration *[BrU]* as a function of the irradiation time. Data presented in Figure 5.3 b).

Irradiation time (min)	0	1	5	10	20	30	40	50	60	70	80	90
[BrU]	12.37	11.14	10.28	9.67	8.54	7.40	6.30	5.20	4.29	3.37	2.56	1.62
Δ[BrU]	0.14	0.14	0.14	0.12	0.12	0.11	0.11	0.11	0.11	0.13	0.14	0.15

S.I. Table 5.3 – Reaction rates as a function of the laser repetition rates. Data presented in Figure 5.4.

40 mM BrU				
Frequency (Hz)	k1 ($puls^{-1}$)	Δk1 ($puls^{-1}$)	k2 ($puls^{-1}$)	Δk2 ($puls^{-1}$)
4	2.02184E-5	8.18345E-7	2.74703E-6	2.13321E-7
6	1.99022E-5	7.23873E-7	1.46826E-6	2.55005E-7
8	1.89349E-5	8.85859E-7	4.55324E-6	4.93752E-7
10	1.82486E-5	7.50822E-7	1.34997E-6	1.57657E-7
12	1.68431E-5	7.07432E-7	2.77589E-6	4.15534E-7
14	1,53243E-5	3,71962E-7	1,95252E-6	2,16141E-7
35 mM BrU				
Frequency (Hz)	k1 ($puls^{-1}$)	Δk1 ($puls^{-1}$)	k2 ($puls^{-1}$)	Δk2 ($puls^{-1}$)
3	1.84951E-5	9.57881E-7	3.83911E-7	3.40785E-8
5	1.73793E-5	1.36372E-6	1.73427E-6	3.44217E-7
7	1.54995E-5	1.31419E-6	2.31902E-6	4.55786E-7
10	1.59941E-5	6.67977E-7	1.78483E-6	1.29012E-7
12	1.68431E-5	7.07432E-7	2.77589E-6	4.15534E-7
15	1.30933E-5	7.38898E-7	1.10882E-6	8.34434E-8

S.I. Table 5.4 – Reaction rates as a function of the laser repetition rates. Data presented in Figure 5.5 a).

Laser fluence 10^{12}(W/m^2)	k1 (min^{-1})	Δk1 (min^{-1})	k2 (min^{-1})	Δk2 (min^{-1})
19.91	0.00586	0.0011	0.00152	1.6E-4
13.74	0.0191	0.00146	0.00361	3.0E-4
10.26	0.02113	0.00196	0.00374	5.2E-4
5.48	0.01869	0.00118	0.00188	8.0E-5
4.83	0.01529	8.3E-4	0.00175	8.4E-5
3.40	0.00789	4.7E-4	8.22E-4	5.5E-5
3.23	0.0097	4.5E-4	0.00137	5,3E-5
2.13	0.00508	2.7E-4	7.85E-4	7,1E-5
1.92	0.00566	2.7E-4	5.14E-4	4.9E-5
1.45	0.00204	9.3E-5	3.51E-4	2.8E-5
1.05	0.00119	2.7E-5	8.16E-5	7,1E-6

S.I. Table 5.5 – AuNP surface area as a function of the laser fluence. Data presented in Figure 5.6 d).

Laser fluence (W/m^2)	3.93E13	1.75E13	6.29E12	2.46E12	1.30E12	9.30E11
As (cm^2/ml)	0.00199	0.00187	0.00138	0.00130	8.8E-4	9.2E-4
ΔAs (cm^2/ml)	4.0E-4	2.3E-4	2.2E-4	2.9E-4	1.9E-4	3.1E-4

S.I. Table 5.6 – Illuminated AuNP surface area as a function of the laser fluence. Data presented in Figure 5.6 f).

Laser fluence (W/m^2)	3.93E13	1.75E13	6.29E12	2.46E12	1.30E12	9.30E11
A_{ill} (cm^2/ml)	1.10E-4	1.23E-4	1.23E-4	1.72E-4	1.62E-4	2.07E-4
ΔA_{ill} (cm^2/ml)	2.2E-5	1.5E-5	2.0E-5	3.8E-5	3.5E-5	6.8E-5

S.I. Table 5.7 – Heat absorbed by an individual AuNP as a function of the laser fluence. Data presented in Figure 5.7.

Laser fluence (W/m^2)	3.93E13	1.75E13	6.29E12	2.46E12	1.30E12	9.30E11
Q_{abs} *(J)*	1.42E-13	6.9E-14	6.8E-14	3.9E-14	4.9E-14	3.3E-14
ΔQ_{abs} *(J)*	3.5E-14	1.1E-14	1.3E-14	8.8E-15	1.1E-14	1.1E-14

Chapter 6

Decomposition of halogenated nucleobases by SPR excitation of gold nanoparticles

Decomposition of halogenated nucleobases[1]

6.1. Abstract

Halogenated uracil derivatives are of great interest for cancer therapy, either as chemotherapeutics or radiosensitizers depending on their halogen atom. In this work we investigated the radiation damage of uracil (U), 5-bromouracil (5BrU) and 5-fluorouracil (5FU) in the presence of gold nanoparticles (AuNPs) upon the irradiation with a Nd:YAG ns-pulsed laser operating at 532 nm at different fluences. AuNPs absorb light efficiently by their surface plasmon resonance and significantly damage DNA in their vicinity by an increase of temperature and the generation of reactive secondary species, like low energy electrons. Our results show that the presence of gold nanoparticles efficiently decompose the ring structure of nucleobases (NBs) independent of the halogen species. In addition to the decomposition of the fragmentation of the pyridine ring, for BrU the cleavage of the carbon-halogen could be observed, whereas for FU this reaction channel was inhibited. The obtained insights in the molecular damage towards DNA nucleobase derivatives in the proximity of laser irradiated AuNPs provide implications for cancer photo thermal therapy and the application of radiosensitizing molecules therein.

[1]This chapter is based on the following publication:

T.S. Marques, M.A. Śmiałek, R. Schürmann, I. Bald, M. Raposo, S. Eden and N.J. Mason. Decomposition of halogenated nucleobases by SPR excitation of gold nanoparticles. European Physical Journal D, Section: Atomic and Molecular Collisions. pp. 1-9, 74, 222 (2020). ISSN: 1434-6060. (https://doi.org/10.1140/epjd/e2020-10208-3).

6.2. Introduction

For many decades there is an on-going race for finding the most efficient and effective radiosensitizer to be used in several types of cancer therapy. One of the possible approaches to therapy is sensitizing DNA using halogenated nucleobases, like 5-Bromouracil (5BrU) and 5-Fluorouracil (5FU). Recent studies revealed that the first compound acts as a base analogue, replacing thymine in DNA without substantially altering their biological activity and it is known to act as a radiosensitizer, which enhances DNA radiation damage due to its high reactivity with electrons at very low energies [1]–[3]. The other uracil derivative, 5FU is commonly used as a drug in treatment of solid cancers, such as breast, head, skin, colon, stomach and head cancer [4], [5]. The structures of the molecules tested in our experiments are shown in Figure 6.1. Together with the reference molecule, uracil, our targets were tested for damage formation upon pulsed laser irradiation at 532 nm, since both compounds are known for their photosensitivity in the UV range.

Apart from direct damage, caused by the laser light, also gold nanoparticles (AuNPs) of 40 nm in diameter were used in order to test their sensitizing capabilities. AuNPs also show a characteristic surface plasmon resonance (SPR) around 530 nm, depending on the size and shape of the particles. The laser wavelength was chosen to match this SPR band associated with AuNPs [6], [7].

The use of AuNPs in cancer therapy is already a topic of a very broad investigation [7]–[14]. It was already shown that there is a sensitizing effect of AuNPs upon various types of radiation, being capable to entry into cancer cells [15], [16].

Thus, a combination of halogenated uracils and AuNPs may form a radiosensitizing “cocktail” for use in example in phototherapy. In this work, we wanted to combine these two approaches to sensitizing cancer cells and used both the sensitizer that is, a halogenated base that incorporates itself into the DNA helix, as well as the freely floating NPs that approach DNA but do not bind. We were aiming at combining the two effects already known from the literature and creating the system that enables more accurate and lethal damage to be delivered to a specific sequence in DNA helix.

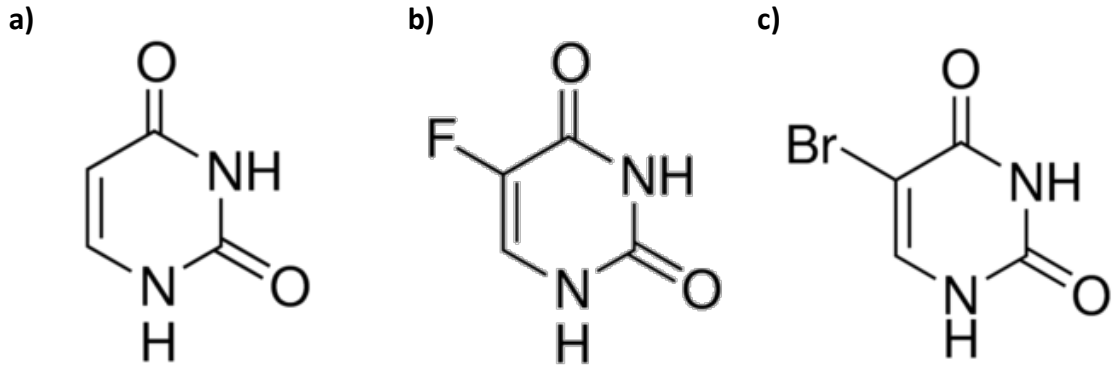

Figure 6.1 – Chemical structures of the nucleobases used in this work, a) U, b) 5FU and c) 5BrU.

6.3. Experimental methods

In these experiments we have replicated the setup described by Schürmann and co-workers [17] in order to allow direct comparison.

6.3.1. Chemicals and solutions

All the nucleobases used: uracil (U; cas 66-22-8), 5-bromouracil (5BrU; cas 51-20-7) and 5-fluorouracil (5FU; cas 51-21-8) were purchased from Sigma-Aldrich, UK. Gold nanoparticles of 40 nm diameter (AuNPs; cas EM.GC40) were purchased from British Biocell International (BBI Solutions), UK. The AuNPs were supplied as an aqueous suspension with a concentration of 9.00×10^{10} gold particles/mL. All chemicals were used without further purifications.

Aqueous solutions and dilutions were prepared with ultra-high purity water (UHPW) with resistivity of 18.2 MΩ.cm, supplied by a Suez-Purite Neptune purification system. The NBs were used at a final concentration of 25 µM, whereas AuNP solution with final concentration of 44.7 pM. Samples were prepared freshly before each set of irradiation. In each experiment, 2 mL of solution were placed in a QS (quartz glass high performance) cuvette (Hellma®), with 10 ± 0.01 mm of optical path length.

6.3.2. Irradiation setup

The experiments were performed in the Molecular Cluster Laboratory, The Open University, United Kingdom. We have used for these experiments a setup that is similar to the one used by Schürmann and co-workers described elsewhere in detail [17].

Briefly, the second harmonic (532 nm) of a Minilite nanosecond pulsed Nd:YAG laser from Continuum®, was chosen as the irradiating light source. In this study, the pulse repetition rate was maintained constant at 15 Hz and energy tuned to 16 mJ per pulse, giving the power of 240 mW. The distance from the focus of the laser beam (Z) can be varied through translation of the platform upon which the sample is placed with movement on the Z axis (3D) from 0 mm, where the beam is focused at the surface of the sample, to 10 mm, roughly halfway through the sample volume (Figure 6.2). The laser fluence at the surface per pulse for each position was calculated through equation [6.1]:

$$Laser\ fluence = \frac{energy\ per\ pulse}{A_{beam} \times pulse\ width} \qquad [6.1]$$

where the *energy per pulse* unit is in joules (J), and the *pulse width* (FWHM) corresponds to $5.0 \times 10^{-9}\ s$, while A_{beam} is the area of the circular beam in square meters at the entrance of the sample. The illuminated volume was obtained from the measurement of the r dependence with Z and calculating the resulting revolution solid integral. The results obtained are presented in the Supporting Information (SI) S.I. 6.8.1.

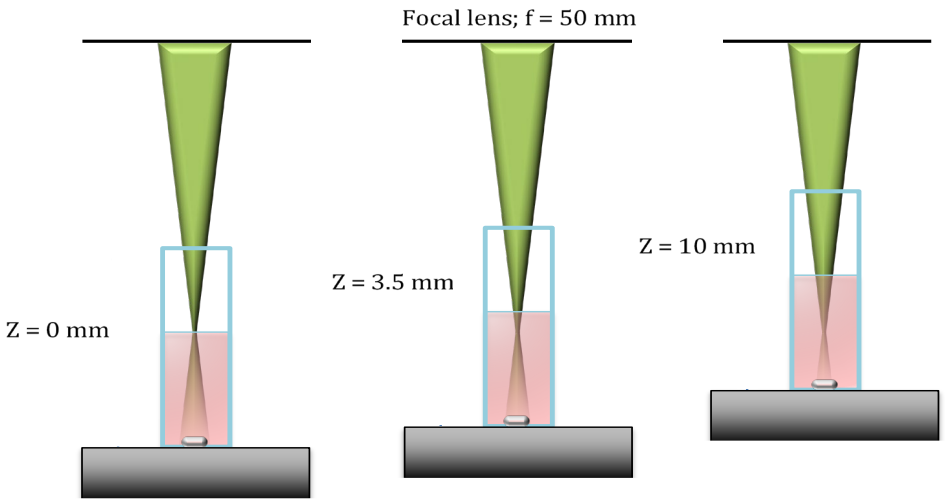

Figure 6.2 – Illustration of the focal distance Z variation inside the sample irradiated

The beam was focused by the optical system to a surface area of 0.12 mm^2, corresponding to the focal distance of Z = 0 mm, where the focus of the beam is at the surface of the sample (Figure 6.2). The samples were irradiated from the top whilst being continually stirred to avoid 'hot spots'. Before each set of irradiations, the power of the beam was assessed using a laser power meter (UNO from Gentec-EO).

6.3.3. Measurement photoabsorption spectrum of the solution

UV-Vis absorbance measurements were performed using a Thermo Scientific™ Evolution™ 201 (UK) spectrometer operating over the range of 190 to 800 nm, with a bandwidth of 1 nm and data intervals of 1nm. The spectrophotometer was placed next to the irradiation apparatus to minimize the time elapsed between irradiation and spectrum acquisition. Therefore, all spectra where acquired after the irradiation specific time and the cuvette place backwards on the setup for the coming irradiations. All measurements were performed at room temperature (RT), in triplicate, using measurements of UHPW as reference. The samples were irradiated until the spectrophotometric band of the analyte was close to zero absorbance, indicating that complete degradation of the NB.

6.4. Results and discussion

6.4.1. Absorption coefficient values determination

In this experimental work, we intended to determine the concentration decrease in the individual NBs. It is known that, uracil has a characteristic absorption band centred at 255 nm [18], 5BrU at 277 nm [17] and 5FU at 266 nm [3]. From the results available in the literature [2, 5, 17, 19] and the first plots obtained experimentally, we have observed that there is an overlap of π-π* signal of NBs with the interband (IB) states of AuNPs. Hence, the determination of the absorption coefficients from the standard curves of the NBs+AuNPs, helps us inferring on the probability of degradation due to higher absorption of light and the

fit equations will permit the quantification of NBs individual concentration in the mixed solution after irradiation. Figure 6.3 a) presents an example of the UV-Vis spectra, corrected for AuNPs signal, obtained of the aqueous solutions of U, 5FU and 5BrU at concentration of 25 µM with AuNPs for Z = 1 mm. These spectra show the maximum absorbance, associated with the π-π* transitions [5] for the NBs used. The uracil peak is slightly different from that found in the rerefences [1, 2, 18], which may be attributed to a solvent effect. To determine the absorption coefficients, the maximal values of absorbance that were achieved for each concentration after background subtraction (namely IB and SPR band) were plotted in Figure 6.3 b). The correction was obtained through the subtraction of the spectra of the AuNPs solution (the control solution) from the data NB+AuNPs. The standard curves were built for the three NBs, and are the result of the Gaussian fit of the corrected absorption spectra for each NB (Figure 6.3 b)). The linear fit suggests a direct proportionality between maximum absorption and concentration in the range studied (5 – 100 µM).

The experimental extinction coefficients of the NBs were calculated using the linear fit equations presented in Figure 6.3 b), and the values are listed in Table 6.1. Calculations of extinction coefficient (ε) are based on the Beer Lambert law, $A = \varepsilon \cdot l \cdot c$, where A is the absorbance of the solution at a particular wavelength, l is the length of the optical path and c the concentration of the solution. The extinction coefficient is experimentally calculated using the slope of the linear fit of the absorbance vs concentration spectra of a given compound for a given wavelength, that is measuring A/c, with l equal to 1 cm (from the cuvette specifications).

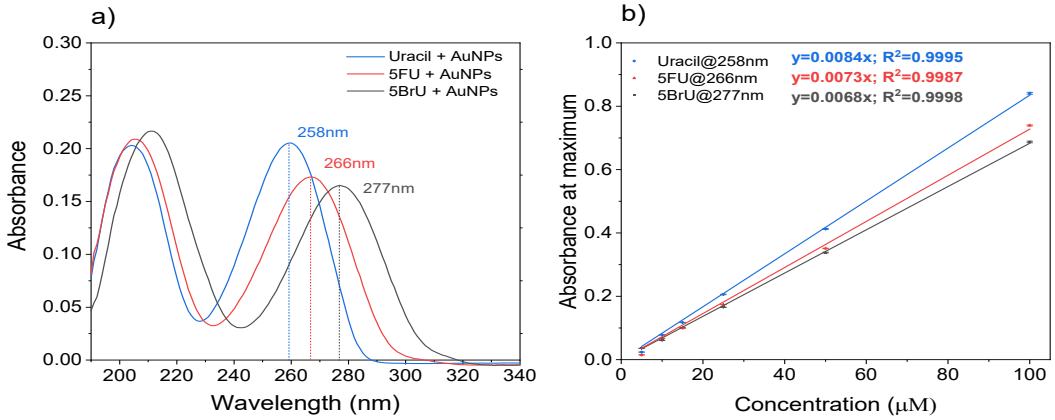

Figure 6.3 – a) UV-Vis spectra of aqueous solutions of U, 5FU and 5BrU with AuNPs at the concentration of 25 µM, and b) standard curves for the NBs in study where the maxima absorbance of the characteristic peaks (258, 266 and 277 nm, respectively) are plotted *vs* concentration of aqueous solutions NBs+AuNPs.

Table 6.1 also presents the maximum wavelength (π-π^*) of the characteristic peak in the UV-Vis spectra for the nucleobases studied (Figure 6.3 a)) as well as the calculated values for the extinction coefficient, where the error presented is the standard deviation of the average, compared to the ones found in the literature.

Table 6.1 – Maximum wavelength and extinction coefficients of U, 5FU and 5BrU.

Nucleobase	π-π^* (nm)	Extinction coefficient ($M.cm^{-1}$)	
		Literature	This work
Uracil	260; 255	7800-8200 [1], [2], [18]	8400 ± 562
5FU	266	7000 [3]	7300 ± 659
5BrU	277	7010 [2], [4]	6800 ± 400

The comparison of the experimental data with the data available in the literature (see Table 6.1) suggest that the values are similar, considering the uncertainties obtained for each fitted curve. These coefficients suggest that U is the molecule that presents higher capacity to absorb photons, followed by 5FU and 5BrU. These results may indicate that the decomposition rate of Uracil when exposed to laser light will be the highest while 5BrU presents the lower degradation rate. This statement will be further assessed and discussed in the results section.

6.4.2. Photon-Induced damage

The absorbance of NBs mixed with AuNPs, for various irradiation times, and of pure AuNPs under the same conditions, are shown in columns a) and b) in Figure 6.4. The effect of the irradiation time on the nucleobases is presented in Figure 6.4 column c). These spectra are obtained by subtracting from the UV-Vis spectra of the NBs with AuNPs, Figure 6.4 column a), the spectra of pure AuNPs, Figure 6.4 column b), when irradiated under the same conditions (Z = 1 mm). The spectra of U, 5FU and 5BrU are shown in rows 1), 2) and 3), respectively, of Figure 6.4.

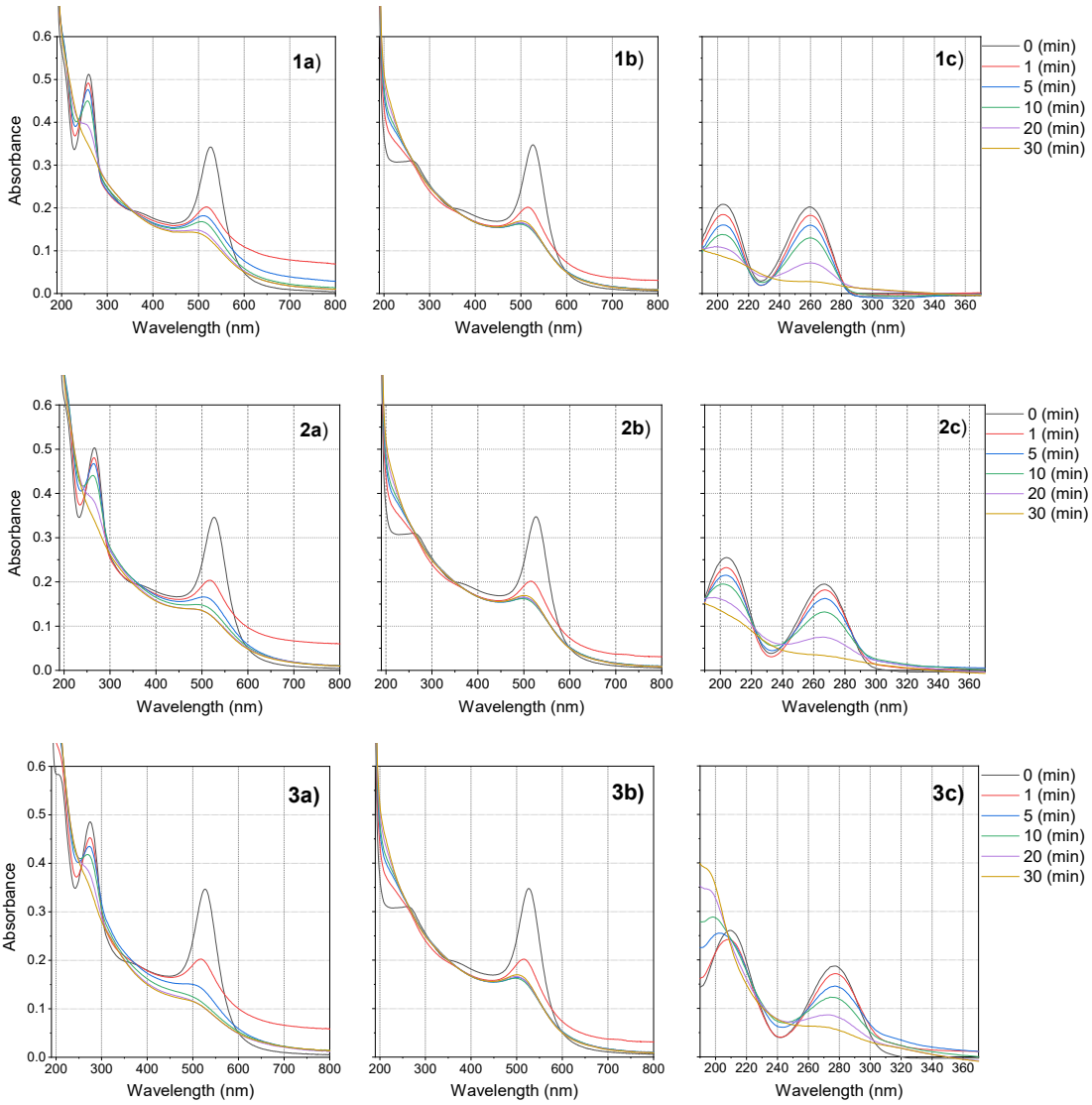

Figure 6.4 – Absorption spectra of 1) U; 2) 5FU; and 3) 5BrU exposed to Nd:YAG laser radiation of 532 nm up to 30 minutes with a) showing the raw spectra of NB+AuNPs solution, b) the raw spectra of AuNPs solution and c) the correction of the nucleobase absorption spectra by subtracting the spectrum of nucleobase irradiated with AuNPs with the correspondent spectrum obtained for the solution of AuNPs irradiated. Z = 1 mm.

All the irradiations described above where measured in the same day in order to avoid contributions/modifications from external factors; that way the same control for all the samples was used.

The corrected spectra of all NBs show that the exposure to the laser light led to the reduction of the absorbance band assigned to π-π* transitions of these compounds, which is a result of the decomposition of the NBs. Moreover, when the data presented in column c) was fitted with Gaussian curve for the maximum wavelength characteristic of each NB and the resulting absorbencies plotted against the irradiation time (Figure 6.5).

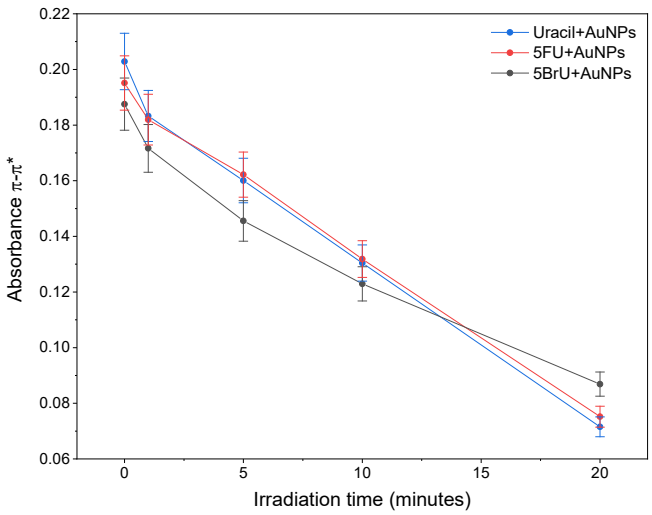

Figure 6.5 – Maximal absorbance, associated with the π-π* transitions, measured in the corrected spectra of U, 5FU and 5BrU as a function of the irradiation with Nd:YAG at laser fluence 25.5x10^{13} W/m^2 (Z = 1mm).

For uracil, a highest rate of decomposition was noted, of approximately 65 % for the 20 mins irradiation time. It is followed by 5FU with a decrease in the characteristic peak of 61 % and 5BrU showing a reduction of around 54 %. Similar trends where obtained for the different positions analysed whose plots are presented in S.I. 6.8.2.

To analyse the variations occurring in the AuNPs SPR absorption band, the maximum absorption at 532 nm was plotted for the different sample positions (z) at the exposure time of 20 minutes and are presented in Figure 6.6. The irradiated volume decreases with sample position due to the conical distribution of the beam. As the sample moves up, the irradiated volume decreases, as shown in Table 6.2 – Variation of the irradiated volume and temperature of the AuNPs with sample position., hence increasing the energy deposited per volume per pulse (i.e. irradiation dose). The dose (and hence the temperature), on the other hand, has an effect on the response of the NPs, namely on the size distribution, which will also dictate the SPR absorption characteristics (area, peak position). Thus, position 0 will have a larger irradiated volume, a lower dose as well as lower increase in temperature (~1700 K) while position 10 has the smallest irradiated volume, a higher dose and a three-fold temperature increase to about 4600 K. The (rough) estimation of temperature was carried considering that the 1/100 of the energy pulse was absorbed by all 20 nm radius NPs in the illuminated volume, using bulk Au constants. The temperature will affect the dynamics of the destruction (explosion) of

the AuNPs, cooling (water does not absorb in these wavelengths and the measured temperature remained close to RT) and aggregation of the AuNPs. In fact, for the irradiation times up to 1 minute, preliminary DLS and TEM measurements (data not showed) revealed a normal distribution of NPs centred at ≈1 nm diameter. As the dose increases, large particles of diameter greater than 30 nm are also observed [19].

Table 6.2 – Variation of the irradiated volume and temperature of the AuNPs with sample position.

Position Z (mm)	Surface fluence (W/m^2)	Illuminated volume (m^3)	Illuminated volume (%)	ΔT (K)
0	$4.02x10^{14}$	$4.2\ x10^{-08}$	2.10	1700
1	$2.55\ x10^{14}$	$3.7\ x10^{-08}$	1.85	1900
2	$1.82\ x10^{14}$	$3.2\ x10^{-08}$	1.63	2200
3.5	$1.00\ x10^{14}$	$2.7\ x10^{-08}$	1.34	2700
5	$6.63\ x10^{13}$	$2.2\ x10^{-08}$	1.11	3200
10	$1.56\ x10^{13}$	$1.6x10^{-08}$	0.78	4600

The maximum absorbances of the characteristic wavelength for each NB+AuNPs was plotted against laser fluence and is presented in Figure 6.6 a). The data suggest that 5BrU has a slower decomposition rate as predicted.

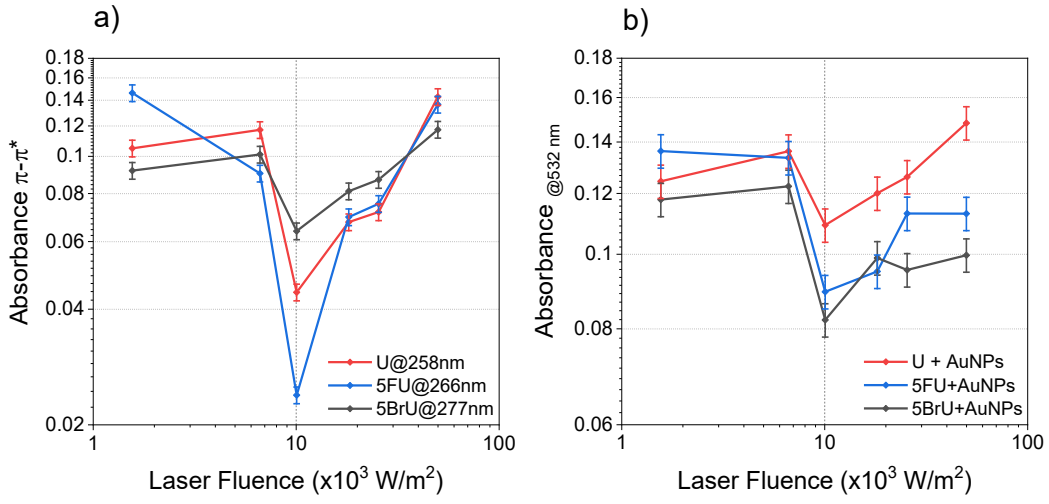

Figure 6.6 – Maximum absorbance of a) solutions uracil (red), 5FU (blue) and 5BrU (grey) with AuNPs, at 258 266 and 277 nm, respectively, after 20 minutes of laser illumination, and b) absorption of AuNPs solutions with uracil (red), 5FU (blue) and 5BrU (grey) for the characteristic SPR at 532 nm, after 20 minutes of laser illumination, plotted as a function of laser fluence.

Both U and 5FU present a very similar trend, and all the NBs reached a minimum of the absorption at 10^{13} W/m^2 (position 3.5 mm), fluences where there are essentially 2 nm NPs, resulting in a large decrease of the plasmon band. As the laser fluences increases (positions 5 and 10), the average size of the particles tend to increase due to coalescence, increasing the intensity of the SPR absorption band. This may indicate that for higher area to volume ratio (positions 0 to 3.5 mm) the reaction occurs at a higher rate. This rate decreases as some large particles are formed (positions 5 and 10), which decrease the area/volume ratio. It is worth noting that at positions 5 and 10 the boiling temperature of bulk gold (2792 K) is exceeded.

6.4.3. Do the AuNPs enhance the laser irradiation effect?

To answer this question, we have exposed the three NBs to the laser radiation under the same conditions. As discussed previously, we have chosen the position of Z = 1 mm, and 20 minutes as maximum of exposure period. For each compound, we have performed the experiments in the absence of AuNPs, using the same final concentration of NB, and with solutions freshly prepared. The data treatment applied to the spectra obtained follows the same rationale used for the samples with AuNPs, however here the control is only UHPW irradiated in the same conditions as the samples and is presented in detail in S.I. 6.8.3. Figure 6.7 a) was generated from the Gaussian fit to the π-π* transitions of the NBs varying with time in absence of AuNPs, and in Figure 6.7 b) the same data as in Figure 6.5 are shown, thus the maximum absorbance in NBs solutions with AuNPs up to 20 minutes of irradiation.

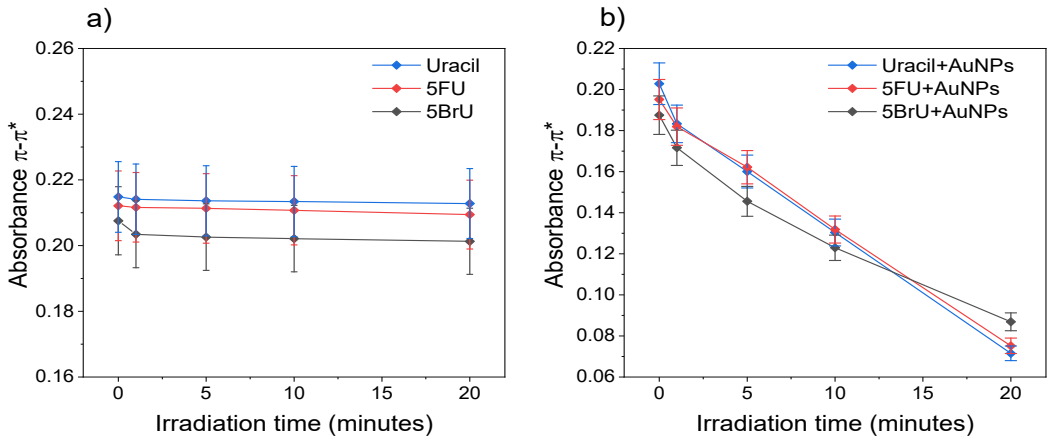

Figure 6.7 – Changes in the maximum absorbance of the NBs in study after exposure to laser light a) without AuNPs, and b) in presence of AuNPs, performed at laser fluence 25.5x10^{13} W/m^2 (Z = 1 mm).

The results presented above clearly show that the presence of AuNPs during the irradiation with the 532 nm Nd:YAG laser dramatically enhances the degradation of all the nucleobases under study as compared to nucleobases irradiated under the same conditions in the absence of AuNPs. The percentage variation of the π-π* transitions for the NBs was determined through the following equation:

$$\Delta Abs = \frac{Abs_0 - Abs_n}{Abs_0} \times 100\ \%, \qquad [6.1]$$

where ΔAbs is the variation of the absorbances, Abs_0 the absorption before the laser illumination and Abs_n corresponds to the absorption measured for a specific irradiation time between 1 and 20 minutes, and the result is presented in Table 6.3. Uracil is the NB that absorbs more light and thus presents the highest reduction of the peak for the maximum time of irradiation in presence of AuNPs. In the absence of the AuNPs, the laser light itself does not seem to be able to induce significant decomposition of the NBs.

Table 6.3 – Summary of the reduction (in percentage) of the characteristic band for each nucleobase with the increase of the illumination time (Z= 1 mm).

Irradiation time (minutes)	Presence of AuNPs			Absence of AuNPs		
	U	5FU	5BrU	U	5FU	5BrU
0	0	0	0	0	0	0
1	10	7	8	0	2	0
5	21	17	22	1	2	0
10	36	32	34	1	3	1
20	65	61	54	1	3	1

6.4.4. Concentration calculations

The results described in this work show the reduction of the π-π* absorption band for the three NBs in study, after irradiation in the presence of AuNPs. Therefore, it is important to understand the mechanism that drives this damage. Since we expect that the decomposition of 5FU and 5BrU increases with irradiation time, an increase in the concentration of the uracil should be observed providing that dehalogenation is the key mechanism. We have thus estimated the amount of 5FU, 5BrU and U that are being formed/decomposed. The Gaussian fit for two peaks with maximum wavelengths of 258 and 266 nm for each individual spectrum presented in Figure 6.4 2c) (5FU results), and two peaks with maximum of 258 and 277 nm

for each individual spectrum presented in Figure 6.4 3c) (5BrU results), were calculated from the respective absorbances. The next step was to determine the concentration of each pair (5FU+U and 5BrU+U) using the linear fit equation employed already in Figure 6.4 2 b), thus creating standard curves of 5FU and 5BrU. An example of the data analysis for 5BrU is shown in the plots presented in Figure 6.8.

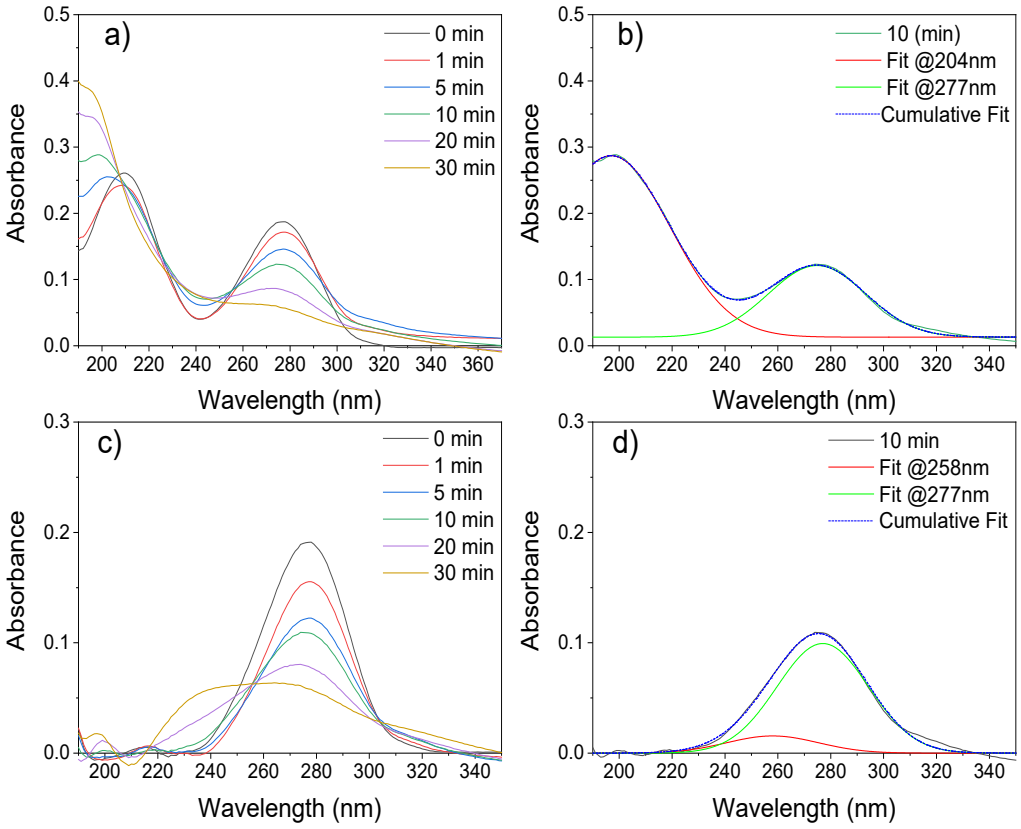

Figure 6.8 – Example of the data analysis: a) corrected 5BrU+AuNPs spectra (Fig. 6.4 3c)); b) Gaussian fit of the two peaks, ≈204 nm and 277 nm, in the 10 minutes spectra; c) subtraction of the band @204 nm and resulting spectra for all the irradiation periods; and d) Gaussian fit for U and 5BrU bands @258 and 277 nm, respectively (Z= 1 mm).

The values of concentration obtained with increasing irradiation time of 5FU are shown in Figure 6.9 a) and irradiation of 5BrU are shown in Figure 6.9 b). The results obtained show that both molecules are strongly affected by the exposure to the laser light, suggesting that although 5BrU is more transparent than 5FU to photons, the total amount of U formed from the decomposition of the parent molecule during the irradiation is higher. Moreover, 30 minutes of irradiation lead to a decrease of approximately 100 % of the 5FU concentration and ≈90 % for the 5BrU.

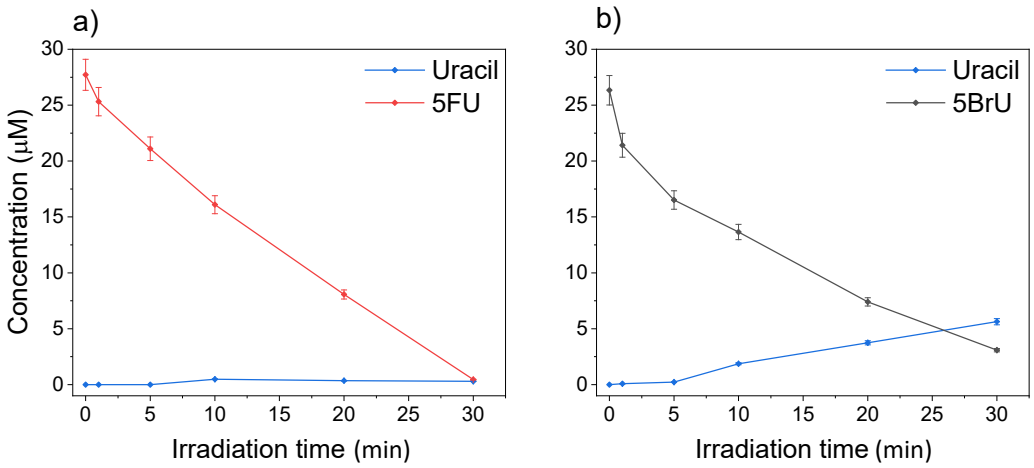

Figure 6.9 – Variations in the concentration of the a) U and 5FU characteristic bands when 5FU is irradiated with AuNPs, and b) U and 5BrU characteristic bands when 5BrU is irradiated with AuNPs, after exposure to laser light, performed at laser fluence 25.5×10^{13} W/m^2 (Z = 1mm).

The similar decrease in the concentration of both 5FU and 5BrU is attributed to the dehalogenation. This process is nearly linear in the case of 5FU, its concentration decreasing close to zero after 30 minutes irradiation, while for 5BrU there is an exponential decay, with a final (30 min) concentration of about 3 μM.

The trend in changes of uracil levels also differs between the two target molecules. The absence of U signal in the case of 5FU indicates that there is immediate ring fragmentation as U is produced from the above-mentioned dehalogenation process. In the case of 5BrU, when the dehalogenation process is more effective (up to 5 minutes, steeper curve) the U concentration is nearly zero and as this process decelerates (5 to 30 minutes) the U concentration increases, possibly from the dehalogenation of the recombined 5BrU. It is worth noting that for 20 and 30 minutes irradiations an additional absorption band at lower wavelengths can be observed (Figure 6.8 c)) that may enlarge the obtained values of U concentration. The expected simultaneous reactions for the decomposition pattern of these NBs are presented in Table 6.4.

Table 6.4 – Equations of the decomposition reactions expected to occur for 5FU and 5BrU, with the increasing of the irradiation time.

Reactions	5FU	5BrU
Dehalogenation	Inhibited or very poor	$BrU + hv \rightleftharpoons Br + U$
Ring fragmentation	$U + hv \rightarrow ring\ fragmentation$	$BrU + U + hv \rightarrow ring\ fragmentation + U$

6.5. Conclusions

We presented a novel approach to study the response of the RNA base uracil and its halogenated analogues to laser photon irradiation in the presence and absence of gold nanoparticles. Our results show clearly that the presence of nanoparticles dramatically increases the levels of damage to modified nucleobases, causing dehalogenation along with damage to the aromatic ring of the base, seen as a loss of the absorption signal with increasing irradiation time. This effect is more pronounced for 5FU than for 5BrU. In fact, 5BrU decomposition is attributed to simultaneous dehalogenation and ring fragmentation, whereas additional recombination of detached Br and U may influence the results. These interesting and novel observations not only present a potential for a new, combined chemo-phototherapy but also proves the outstanding potential of AuNPs as sensitizers.

6.6. Acknowledgements

The authors acknowledge the financial support from the Fundação para a Ciência e a Tecnologia (FCT-MCTES), Radiation Biology and Biophysics Doctoral Training Programme (RaBBiT, PD/00193/2012), Applied Molecular Biosciences Unit - UCIBIO (UIDB/04378/2020) and CEFITEC Unit (UIDB/00068/2020), and scholarship grant number SFRH/BD/106032/2015 to Telma S. Marques.

Author contribution statement

All the authors have been involved in the research and in the preparation of the manuscript. All the authors have read and approved the final manuscript.

Publisher's Note

The EPJ Publishers remain neutral with regard to jurisdictional claims in published maps and institutional affiliations.

6.7. References

[1] R. Schürmann and I. Bald, “Real-time monitoring of plasmon induced dissociative electron transfer to the potential DNA radiosensitizer 8-bromoadenine,” *Nanoscale*, vol. 9, no. 5, pp. 1951–1955, Feb. 2017.

[2] R. Schürmann, “Interaction of the potential DNA-radiosensitizer 8-bromoadenine with free and plasmonically generated electrons,” Faculty of Science of the University of Potsdam, 2017.

[3] R. A. A. Z. Ibrahim, F. S. A. Suhail, and H. K. Al-Hakeim, “Stability of anticancer drug 5-fluorouracil in aqueous solution: An assessment of kinetic behavior,” *Nano Biomed. Eng.*, vol. 10, no. 3, pp. 224–234, 2018.

[4] D. B. DUNN and J. D. SMITH, “Effects of 5-halogenated uracils on the growth of Escherichia coli and their incorporation into deoxyribonucleic acids.,” *Biochem. J.*, vol. 67, no. 3, pp. 494–506, Nov. 1957.

[5] T. S. Marques *et al.*, “Kinetics of molecular decomposition under irradiation of gold nanoparticles with nanosecond laser pulses—A 5-Bromouracil case study,” *J. Chem. Phys.*, vol. 152, no. 12, p. 124712, Mar. 2020.

[6] G. González-Rubio, A. Guerrero-Martínez, and L. M. Liz-Marzán, “Reshaping, Fragmentation, and Assembly of Gold Nanoparticles Assisted by Pulse Lasers,” *Acc. Chem. Res.*, vol. 49, no. 4, pp. 678–686, Apr. 2016.

[7] M. B. Ferruz *et al.*, “New research in ionizing radiation and nanoparticles: The ARGENT project,” in *Nanoscale Insights into Ion-Beam Cancer Therapy*, A. Solov’y., Springer, Ed. Springer International Publishing, 2016, pp. 379–434.

[8] K. Haume *et al.*, “Gold nanoparticles for cancer radiotherapy : a review,” *Cancer Nanotechnol.*, vol. 7, 2016.

[9] S. Grellet *et al.*, “Cancer-selective, single agent chemoradiosensitising gold nanoparticles,” *PLoS One*, vol. 12, no. 7, 2017.

[10] K. Haume, P. de Vera, A. Verkhovtsev, E. Surdutovich, N. J. Mason, and A. V. Solov'yov, "Transport of secondary electrons through coatings of ion-irradiated metallic nanoparticles," *Eur. Phys. J. D*, vol. 72, no. 6, 2018.

[11] K. Haume, N. J. Mason, and A. V. Solov'yov, "Modeling of nanoparticle coatings for medical applications," *Eur. Phys. J. D*, vol. 70, no. 9, 2016.

[12] A. V. Verkhovtsev, A. V. Korol, and A. V. Solov'Yov, "Revealing the mechanism of the low-energy electron yield enhancement from sensitizing nanoparticles," *Phys. Rev. Lett.*, vol. 114, no. 6, pp. 1–6, 2015.

[13] A. V. Verkhovtsev, A. V. Korol, and A. V. Solov'yov, "Electron production by sensitizing gold nanoparticles irradiated by fast ions," *J. Phys. Chem. C*, vol. 119, no. 20, pp. 11000–11013, 2015.

[14] K. T. Butterworth, S. J. McMahon, F. J. Currell, and K. M. Prise, "Physical basis and biological mechanisms of gold nanoparticle radiosensitization," *Nanoscale*, vol. 4, no. 16, pp. 4830–4838, Aug. 2012.

[15] L. Sanche, "Interaction of low energy electrons with DNA: Applications to cancer radiation therapy," *Radiat. Phys. Chem.*, vol. 128, pp. 36–43, 2016.

[16] Y. Zheng and L. Sanche, "Gold Nanoparticles Enhance DNA Damage Induced by Anti-cancer Drugs and Radiation," *Radiat. Res.*, vol. 172, no. 1, pp. 114–119, Jul. 2009.

[17] R. Schürmann and I. Bald, "Decomposition of DNA Nucleobases by Laser Irradiation of Gold Nanoparticles Monitored by Surface-Enhanced Raman Scattering," *J. Phys. Chem. C*, vol. 120, no. 5, pp. 3001–3009, 2016.

[18] R. L. LUNDBLAD and F. M. MACDONALD, Eds., *Handbook of Biochemistry and Molecular Biology*, CRC Press. 2010.

[19] R. Schu and I. Bald, "Effect of adsorption kinetics on dissociation of DNA-nucleobases on gold nanoparticles under pulsed laser illumination †," vol. 39, 2017.

6.8. Supporting Information

S.I. 6.8.1 Laser fluence

S.I. Table 6.1 – Laser fluence for each focal point chose and respective beam diameter.

Focal distance (mm)	Beam diameter (mm)	Surface area (m^2)	Laser Fluence (W/m^2)
0	0.39	$1.19x10^{-07}$	$40.2x10^{13}$
1	0.49	$1.89\ x10^{-07}$	$25.5\ x10^{13}$
2	0.58	$2.64\ x10^{-07}$	$18.2\ x10^{13}$
3.5	0.78	$4.78\ x10^{-07}$	$10.0\ x10^{13}$
5	0.96	$7.24\ x10^{-07}$	$6.63\ x10^{13}$
10	1.98	$3.08\ x10^{-06}$	$1.56\ x10^{13}$

S.I. 6.8.2 Maximal absorbance for U, 5FU and 5BrU

S.I. Table 6.2 – Maximal absorbance, associated with the π-π* transitions, measured in the corrected spectra of U, 5FU and 5BrU as a function of the irradiation with Nd:YAG at laser fluence.

Focal distance (mm)	Laser Fluence (W/m^2)	π -π* Transition plots
0	**$40.2x10^{13}$**	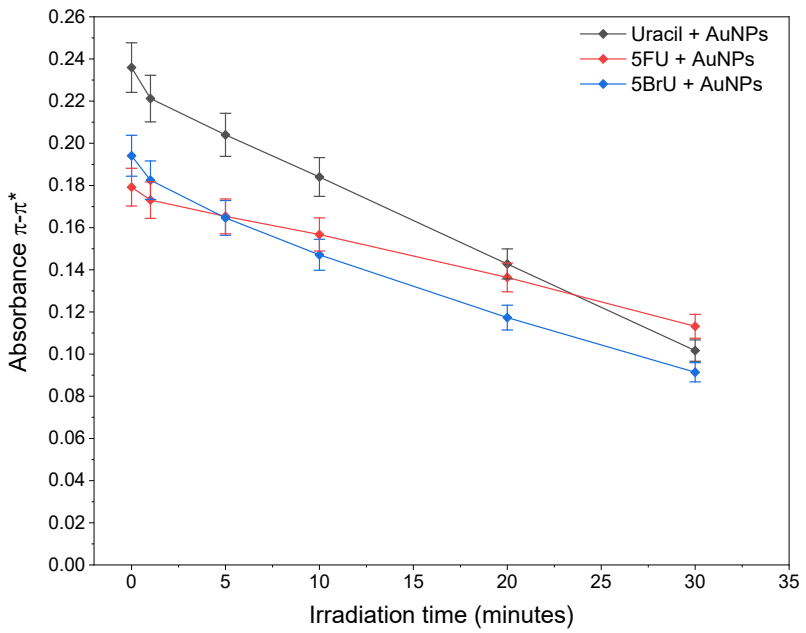

1	**25.5 x10^{13}**	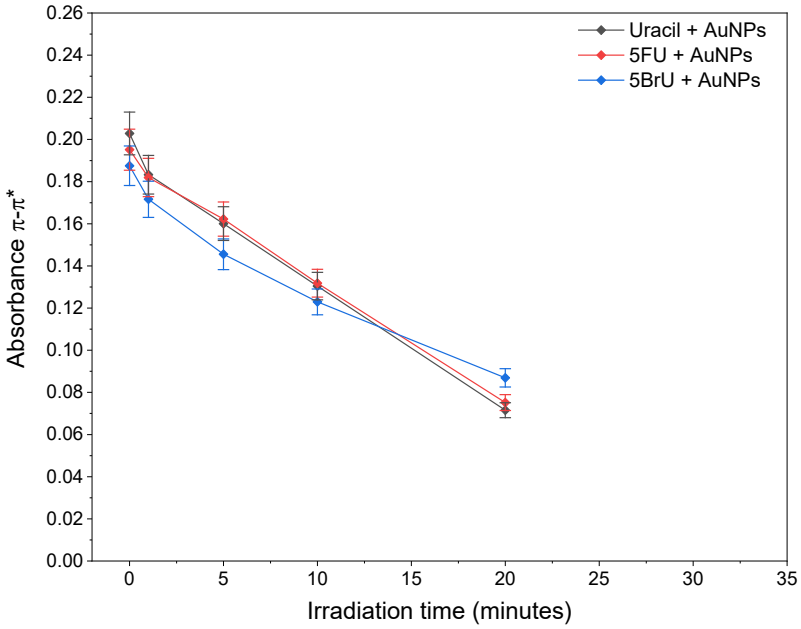
2	**18.2 x10^{13}**	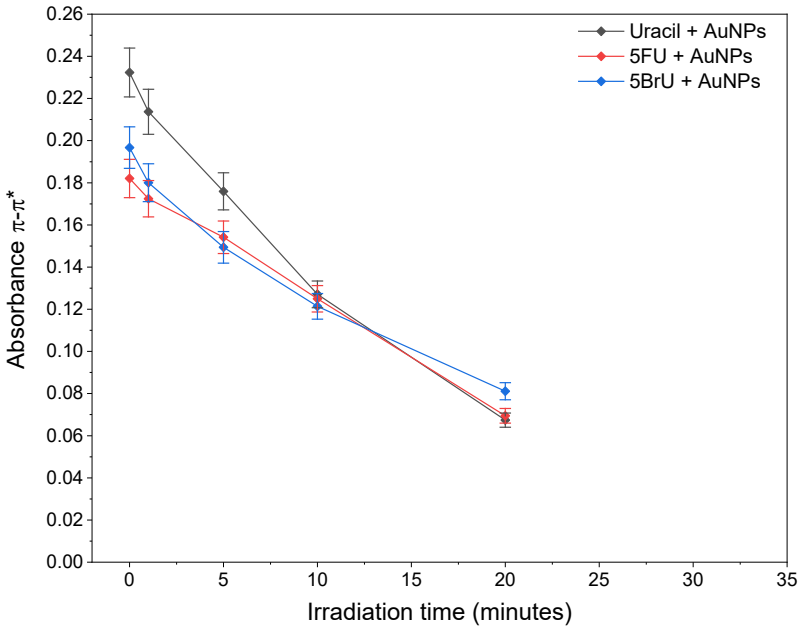

3.5 **10.0 x10^{13}**

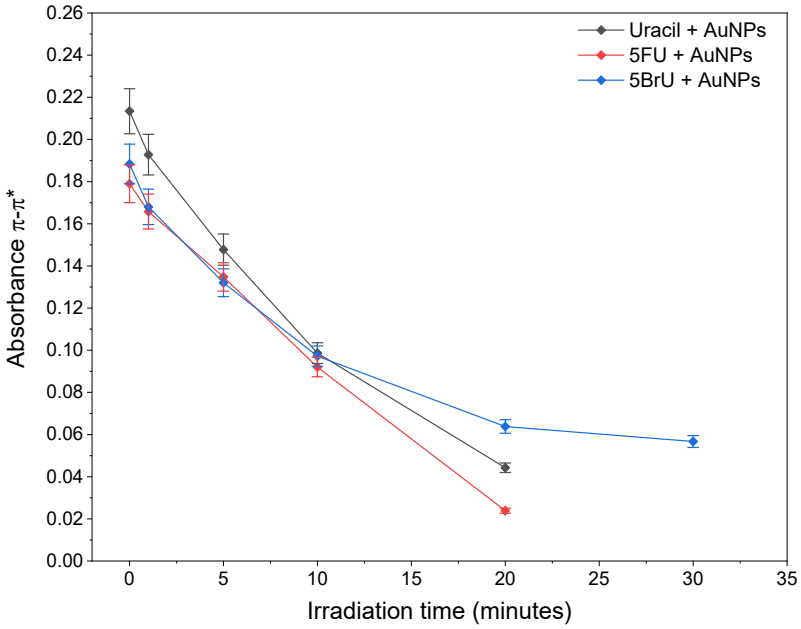

5 **6.63 x10^{13}**

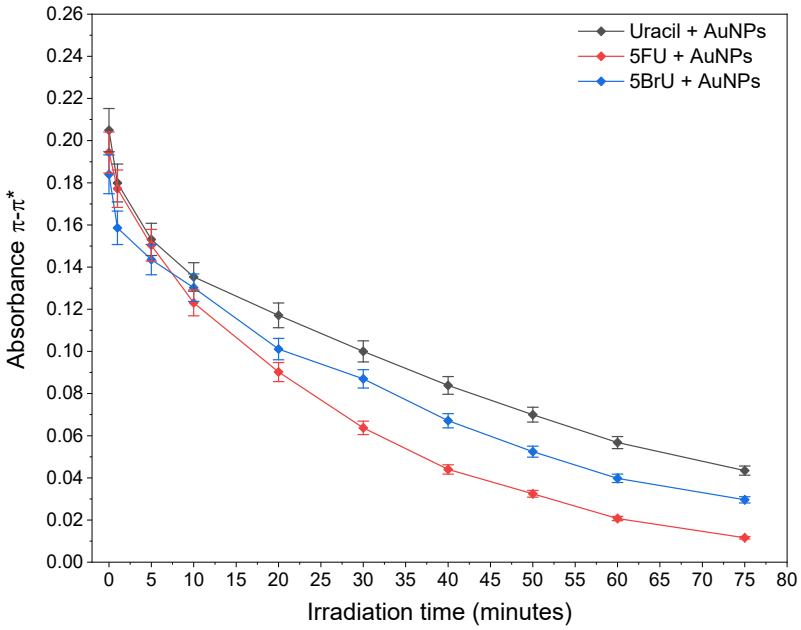

10	**1.56 x10^{13}**	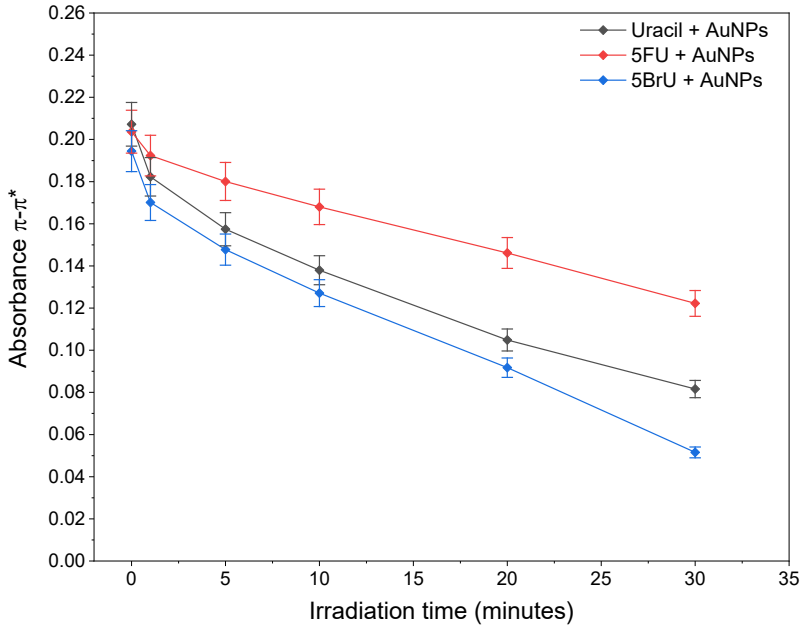

Uracil + AuNPs
5FU + AuNPs
5BrU + AuNPs
Absorbance π-π*
Irradiation time (minutes)
0.26
0.24
0.22
0.20
0.18
0.16
0.14
0.12
0.10
0.08
0.06
0.04
0.02
0.00
0
5
10
15
20
25
30
35

S.I. 6.8.3 Spectra correction in absence of AuNPs

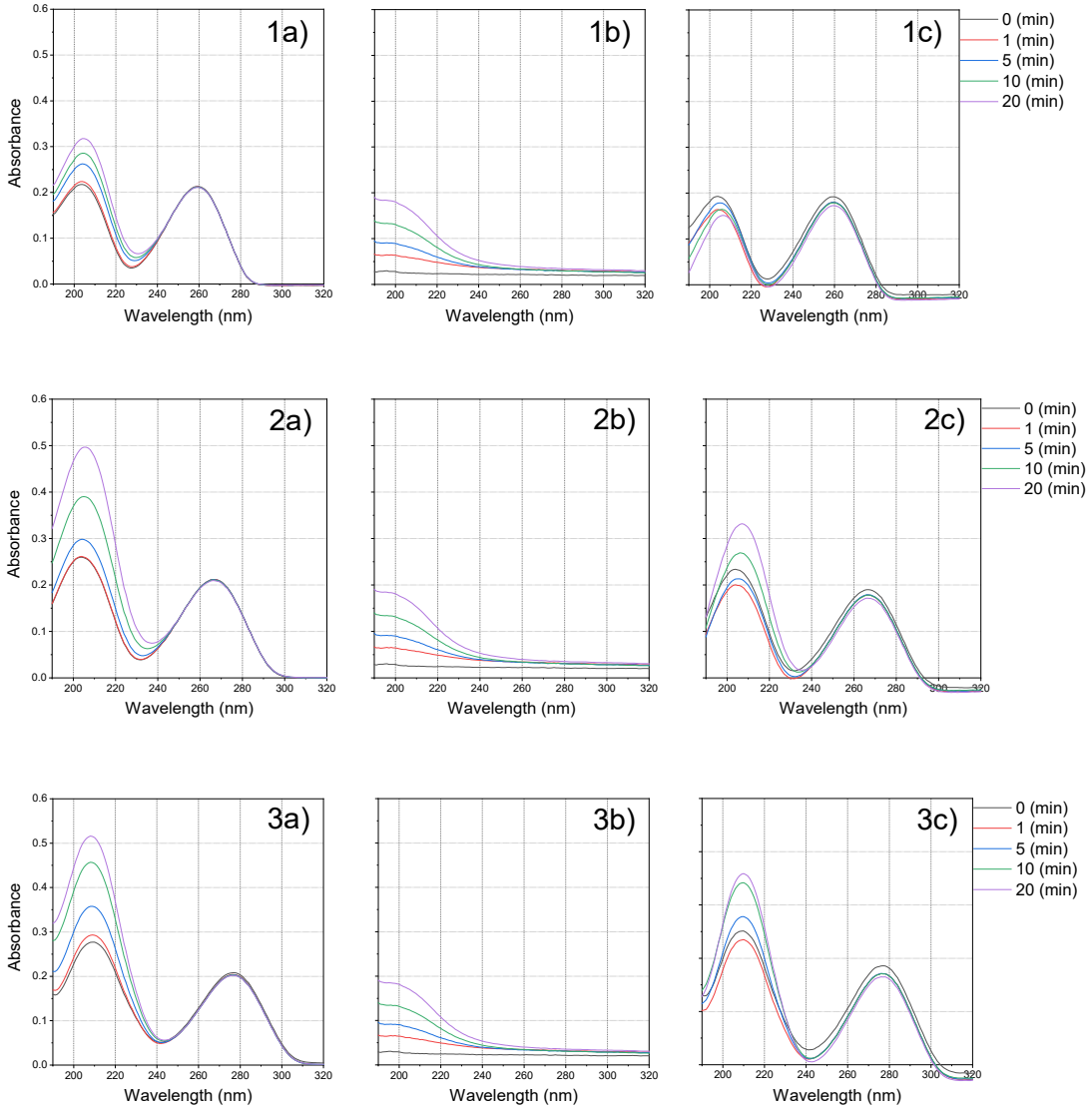

S.I. 6.1 – Absorption spectra of 1) U; 2) 5FU; and 3) 5BrU exposed to Nd:YAG laser radiation of 532 nm up to 20 minutes with a) showing the raw spectra of NBs solutions, b) the raw spectra of UHPW and c) the correction of the nucleobase absorption spectra by subtracting the spectrum of nucleobase irradiated with the correspondent spectrum obtained for the control (UHPW) irradiated. Z = 1 mm.

Chapter 7

DNA damage enhancement through radical formation by Nd:YAG laser irradiation of gold nanoparticles

DNA damage enhancement through radical formation[1]

7.1. Abstract

A long-standing goal in photodynamic therapy is to use visible light for cancer treatment. One of the emerging treatments is photothermal therapy in which visible light is used in conjunction with gold nanoparticles (AuNPs) to generate a surface plasmon resonance on the AuNPs. In this work, we analyse the contribution of the size of the AuNPs to the damage efficiency in the plasmid deoxyribonucleic acid (DNA) when irradiated with 532 nm light delivered from a Nd:YAG pulsed laser. We have demonstrated that an intensity of 5.0×10^{14} W.m^{-2} from the Nd:YAG laser is sufficient to enhance damage to plasmid DNA molecules in aqueous solutions, mainly through water photoionization leading to free radical-induced products such as DNA single-strand breaks (SSBs) and DNA double-strand breaks (DSBs), a rising bulk temperature and AuNPs explosions created by Coulomb effect. Results also demonstrate that such irradiation leads to a major reduction in the diameter of the AuNPs, evaluated by dynamic light scattering and transmission electron microscopy techniques, from 40 to $\approx$ 3 nm after one minute of laser exposition. The addition of a hydroxyl radical scavenger, ethanol (EtOH), to plasmid DNA in the presence of AuNPs reduces the DNA damage, suggesting that DNA damage is induced mostly by free radicals.

[1]This chapter is based on the following publication:

T.S. Marques, G. Ferreira, M.A. Śmiałek, J.P. Golding, M. Raposo, S. Eden and N.J. Mason. DNA damage enhancement through radical formation by Nd:YAG laser irradiation of gold nanoparticles. Manuscript under preparation for submission.

7.2. Introduction

Cancer remains one of the most challenging diseases in the world, inspiring researchers to study and mitigate it through different approaches. Depending on the type of cancer and its location, treatments are adjusted to achieve the greatest efficiency in eradicating the tumour cells and preventing the disease from spreading [1], while limiting damage to healthy cells in the vicinity of the tumour. To achieve this local action, noble metal nanoparticles (NPs) are being exploited along with several energy sources to concentrate damage in biological molecules such as deoxyribonucleic acid (DNA) within tumour cells [2], [3]. Although techniques and therapies have undergone many advancements in recent years, the development of new and more efficient cancer treatments remains one of the significant challenges within the scientific community. One of the emerging treatments is photothermal therapy (PTT) in conjunction with the use nanoparticles [4]–[7]. Recent work in this field has shown evidence of the efficacy of this concomitancy on different types of cancers, for instance, breast cancer, skin cancer, prostate cancer, brain tumours, oral cancer, among others [5], [6], [8], [9]. Gold nanoparticles (AuNPs) have been at the forefront of medical research due to their optical characteristics (e.g. tunable surface plasmon resonance in the visible region) as well as their excellent biocompatibility [8], [10], [11]. The uptake of AuNPs into cancer cells increases cell death by PPT and can be attributed to three major processes occurring locally to the AuNPs: 1) sharp increases in temperature; 2) enhanced production of water-derived free-radicals; and 3) dissolved oxygen in the surrounding medium [12], [13]. These radicals react with nearby molecules in a very short life-time (17 to 10^{-10} s) resulting in breakage of chemical bonds or oxidation of the affected molecules [14], [15]. However, the critical effect in the cells results from the formation of strand breaks in DNA [8], [10]. Yet, the specific mechanisms responsible for AuNP-enhanced radiation damage to DNA and their relative importance are not fully understood.

DNA damage induced by radiation is due to direct effects (DNA and other biological molecules interact directly with the radiation leading to structural alterations including cell death), and indirect effects, namely by free radicals formed during water radiolysis, the process of decomposition of water molecules through ionizing radiation [16], that will react with the biomolecules causing molecular structural damage and the death of the cell [17]. The radicals

produced during water radiolysis are hydrated electrons($e-_{aq}$), hydroxyl radicals ($OH^{\bullet}$), hydrogen atoms ($H^{\bullet}$), superoxide ($O_2^{\bullet-}$) and hydroperoxyl radicals ($HO_2^{\bullet}$). The molecular products formed are hydrogen (H_2) and hydrogen peroxide (H_2O_2). These species, namely $OH^{\bullet}$, $HO_2^{\bullet}$ and H_2O_2, can act as oxidizing agents or reducing species ($e-_{aq}$ and $H^{\bullet}$) [16].

$$H_2O \xrightarrow{Ionizing\ radiation} e^-_{aq}, OH^{\bullet}, H^{\bullet}, HO_2^{\bullet}, H_3O^+, OH^-, H_2O_2, H_2$$

Saha, G. (2013) reported that the indirect processes are far more relevant in the radiation-induced damage since water is the major constituent of cells, and the ultimate outcome of ionizing radiation, direct or indirect, induced alterations in biomolecules and cells that can manifest themselves a long time after the exposure to radiation (seconds or even decades later) [17], [18]. The most relevant DNA lesions caused by radiation are usually reported as base damage and single and double-strand breaks (SSB and DSB) [19]. Several researchers have been studying the methods to demonstrate and evaluate the extension of biological damage and one of the techniques most commonly used is agarose gel electrophoresis (AGE), a simple and efficient method to analyse DNA alterations [20], [21]. These types of DNA damage lead to mutations, carcinogenesis and, ultimately, in cell death, with DSB alterations causing the most injurious effects [19].

The efficacy of cancer treatments can be increased using NPs, which can act as a radiosensitizer. In this context, several researchers are studying the incorporation of metallic NPs to the irradiated system, where they act as radiation magnifiers, tunnelling higher quantities of the energy deposited to the tumour cells, thus increasing the radiosensitization [22]. Gilles, et. al (2018) showed that irradiated gold nanoparticles (AuNPs) in a water medium, increased the production of free radicals, considered as a second step of the irradiation. The first step is the absorption of energy by the AuNPs that will lead to a chemical reaction of the AuNPs and water, resulting in the formation of reactive species [23]. The extension of each of these steps involved in biological damage is intrinsically related to the radiation type and energy, the constituents of the NPs as well as their size, shape and coating, cell location and quantity [22], [23].

In this work, plasmid DNA in aqueous solutions was irradiated with 532 nm pulsed laser light for different periods of time, in the presence and absence of AuNPs. The second harmonic of

the Nd:YAG laser was chosen since the characteristic surface plasmon resonance (SPR) band of the AuNPs with 40 nm is located around 530 nm, and the main goal of this work is to exploit AuNPs effect in order to study induced damage. The irradiation setup and method were developed by I. Bald and co-workers and are described in reference [10].

A selection of different techniques was applied to characterize DNA damage effects of AuNPs in the irradiated samples, including agarose gel electrophoresis (AGE), UV-Visible (UV-Vis) spectroscopy, and fluorescence spectroscopy. AGE and fluorescence measurements following irradiation with and without free radical inhibitors confirm that water-derived free radicals produced during the laser exposure are responsible for extensive cleavage of the DNA strands. Moreover, free radical driven-damage is strongly enhanced in the presence of AuNPs and ethanol was used to confirm the formation of these radical species. These findings support the hypothesis of the size dependency of AuNPs on laser-induced DNA damage.

7.3. Experimental section

7.3.1. Experimental conditions

In this work we have exposed different plasmid DNA solutions to visible light from a Nd:YAG pulsed laser in order to study the damage produced. The solutions of plasmid DNA were irradiated in the presence (samples entitled AuNPs_YAG) and absence (No_AuNPs_YAG) of AuNPs, and compared with the non-irradiated controls (AuNPs and No_AuNPs). To understand the damage driven by free radicals production we have added an $OH^{\bullet}$ scavenger (ethanol, EtOH) to the samples without plasmid DNA and proceeded with similar rational. The effect of the laser in the illuminated AuNPs solutions was measured by subtracting the control solutions (in presence and absence of AuNPs and EtOH) from plasmid DNA solutions in the presence and absence of AuNPs and EtOH (AuNPs_EtOH).

7.3.2. Irradiation setup and UV-Visible measurements

In these experiments, we have replicated the setup described by Schürmann and co-workers [24] and used it without further modifications. Briefly, samples were irradiated with Nd:YAG ns-pulsed laser (Minilite I) from Continuum. The energy was tuned to 16 mJ and the pulse repetition rate was 15 Hz. The diameter of the beam at the solution surface was 0.35 mm, and the pulse width was $4.0 \times 10^{-9}\ s$, thus the calculated laser fluence from equation [7.1] was 5.0×10^{14} W·m^{-2}:

$$Laser\ fluence = \frac{Energy\ per\ pulse}{A_{beam} \times pulse\ width}. \qquad [7.1]$$

The irradiation system focused the beam to a spot of the area of 0.096 mm^2, and the solutions were irradiated from the top and stirred on a magnetic plate during the process.

Before each set of irradiations, the power of the beam was assessed using a laser power meter (UNO from gentec-EO). All measurements were performed at room temperature (RT) in triplicate, with ultra-high pure water (UHPW) as reference. Samples were placed in QS (quartz glass high performance) cuvettes (Hellma®) with light path of 1 cm. The samples were irradiated up to 30 minutes in the absence and presence of AuNPs to evaluate their effectiveness. The UV spectroscopic measurements were performed using a Thermo Scientific™ Evolution™ 201 (UK) spectrometer operating over the range of 190 to 360 nm, with a bandwidth of 1 nm and data intervals of 0.2 nm.

For all experiments, with and without AuNPs, UV-Vis spectra were recorded under the same conditions for the samples and controls (UHPW for solutions in absence of AuNPs, and AuNPs for samples in presence of AuNPs) and the final UV-Vis plots presented in this work correspond to the subtraction of the control (background) data from sample data.

7.3.3. Plasmid DNA Preparation

The strain *E. coli* DH5α competent cells was used as a bacterial host for plasmid pBV-Luc/Del-6, a gift from Joan Massague, Addgene plasmid # 14969, with the size of 4.9 kbp. Single colonies of the bacteria were cultivated in 1 L glass flasks containing 200 mL Luria Bertani (LB) medium L3022 purchased from Sigma-Aldrich (UK) and 50 µg/ml ampicillin (Sigma-Aldrich, UK) antibiotic. Bacteria were grown overnight on a shaker (New Brunswick™ Scientific Classic C10, Eppendorf, UK) at 37°C and 100 rpm. The amplified bacteria were centrifuged at 4°C, 6000 x g for 30 minutes (using Sorvall™ RC 6 Plus Centrifuge, rotor SS-34, Thermo Scientific™, UK), and the remaining bacterial pellet was air-dried for approximately 1 hour. Plasmid DNA was isolated and purified using the QIAGEN Plasmid Maxi Kit (QIAGEN, Hilden, Germany) according to the manufacturer's instructions. The concentration of the extracted DNA was determined spectrophotometrically by measuring absorbance at 260 nm using a NanoDrop™ One Microvolume UV-Vis Spectrophotometer from Thermo Scientific™, UK.

7.3.4. DNA and AuNPs solutions

UHPW from a Suez®- Purite Neptune purification system (resistivity 18.2 MΩ·cm) was used to prepare all the solutions used in this work. A solution of AuNPs with 40 nm diameter, 9.00×10^{10} particles/mL, was purchased from British Biocell International (BBI™ Solutions, Cardiff, UK) and used without further modifications. Samples were prepared in a quartz cuvette with a final concentration of 25 µg/mL DNA and 44.7 pM of AuNP solution, before each set of irradiations.

7.3.5. Agarose Gel Electrophoresis

Agarose gel electrophoresis (AGE) was performed using a horizontal gel system, and the gel was prepared in the concentration of 1.0 % agarose (Seakem ® LE Agarose, Cambrex, UK) in 1x Tris/Borate/EDTA buffer (TBE) at pH 8.0 and run at 8 V/cm at RT for 2 h. Four µL of sample solution were mixed with 2 µL of bromophenol blue used as loading dye and loaded into the

well of the agarose gel. To stain DNA, 0.3 µg/mL of ethidium bromide was added to the agarose mixture before it solidified. Three microliters of Quick-Load® Purple 1 kbp DNA ladder (New England Biolabs, Ipswich, Massachusetts) was used as reference to the correction of the fluorescence intensity of the DNA conformations. The different conformations of plasmid DNA were visualized using a UV transilluminator (G:Box Chemi XX6, Syngene, Cambridge, UK). The DNA bands were imaged by a high quantum efficiency (QE) camera. The DNA bands were analysed with GeneTools (Syngene, Cambridge, UK) and for the interpretation of the results, the sum of the fractions of supercoiled (SC), relaxed (R) and linear (L) forms was assumed as 100 %. With our samples, SC and R plasmid bands were the native ones, with the SC band being the highest intensity in all control samples. Therefore, DNA damage was characterised by the measured increase of the R form, with consequent decrease of the SC, and the appearance of a new band – L conformation [25].

The R band of plasmid DNA corresponds to the fraction of induced SSBs, while the L band corresponds to the fraction of induced DSBs [25]. DNA damage was quantified by integrating the fluorescence intensity of the three possible DNA conformations. The yields of each form of plasmid DNA were quantified by integrating the corresponding fluorescence intensity of the gel bands using GeneTools software.

7.3.6. AuNPs size distribution measurements

Dynamic light scattering (DLS) analysis of irradiated AuNPs was performed using a Nanotrac® Flex 180° backscattering DLS system (Microtrac, UK) equipped with a red laser (780 nm, 5 mW) and a photodetector. Aliquots of 10 µl from the AuNPs solutions were placed on the sample holder and analysed in triplicate. Each measurement was an average of 30-seconds runs. The AuNPs size distribution was measured by transmission electron microscopy (TEM) imaging using a JEM-2100 microscope (JEOL®, USA) at an accelerating voltage of 100 kV and a magnification from x50 000 to x200 000. Aliquots of 2 µl of AuNPs were air-dried overnight on an electrostatically discharged carbon mesh grid before electron microscopy. The nanoparticle size was measured after applying a threshold to TEM images using ImageJ® software, where the data of the area of AuNPs was obtained. The AuNPs diameter was

calculated from the area values from the 2D images, assuming that each AuNPs shape is a sphere. Moreover, DLS allows to measure the polydispersity index (PDI) of the AuNPs in solution, enabling to infer on the aggregation of the NPs upon laser illumination.

7.3.7. Free radical assays

The action of a free radical through oxidation damages biological molecules such as DNA. In these experiments, free radicals are formed during water radiolysis, and they are integral to DNA damage and will be studied using fluorescence probes.

7.3.7.1. Coumarin-3-carboxylic acid

To evaluate 7-hydroxycoumarin-3-carboxylic acid (7-OHCCA) activity in the solutions we have followed the method previously described by Park et al [26]. Coumarin-3-carboxylic acid (3-CCA) is a fluorogenic probe that is sensitive to $OH^{\bullet}$, thus 3-CCA oxidation originates 7-OHCCA and the fluorescence intensity is measured to estimate the production of $OH^{\bullet}$. A stock solution of 3-CCA 5 mM was prepared in phosphate-buffered saline (PBS at 3%) at RT until the 3-CCA was fully dissolved. The, pH was adjusted to 7.4 with a solution of hydrochloric acid (HCl 1 M). Since this method is highly sensitive to pH alterations, control samples were carried and subtracted from the experimental results to minimize the influence of external factors. A calibration curve of 7-OHCCA was prepared in phosphate-buffered saline (PBS) with several dilutions of the stock solution (10 up to 100 µM), and the results were corrected using the control. The fluorescence intensity was measured, in quadruplicate, with a FLUOstar OPTIMA FL - Microplate Reader from BMG LABTECH, using the emission wavelength of 450 nm, excitation of 390 nm and a fluorescence-signal gain of 2500. 3-CCA solutions were prepared with a final concentration of 2.5 mM in the presence and absence of AuNPs. The samples were irradiated by the Nd:YAG pulsed laser for up to 30 minutes and fluorescence intensity was measured in quadruplicate for each exposure time. Control samples were also carried out in the presence and absence of AuNPs.

7.3.7.2. Dihydrorhodamine-123

To evaluate H_2O_2 activity in the solutions we have followed the method previously described by Wang et al [27]. The principle of the method is based on the oxidation of the Dihydrorhodamine-123 (DHR-123) molecules giving rise to rhodamine 123 (RHD-123), a fluorescent molecule, which allows the detection of H_2O_2 in solution. Stock solutions of DHR-123 (5 mM) were prepared in 3 % PBS at RT. The pH was adjusted to 7.4 with the solution of 1 M HCl. The fluorescence intensity was measured for the samples in the presence and absence of AuNPs and with 2.5 mM DHR-123, final concentration. A calibration curve of RHD-123 was prepared in phosphate-buffered saline (PBS) with several dilutions of the stock solution (8.4×10^{-6} to 6.4×10^{-3}μM), and the results were corrected to the control. The samples were irradiated with a Nd:YAG pulsed laser for up to 30 minutes, and fluorescence intensity was measured, in quadruplicate, with a FLUOstar OPTIMA FL - Microplate Reader from BMG LABTECH, using the emission wavelength of 544 nm, excitation of 485 nm and a gain of 1500, for each exposure time. Control samples were carried out.

7.3.7.3. Ethanol as hydroxyl scavenger

To evaluate the effect of hydroxyl radicals ($OH^{\bullet}$), ethanol was chosen as an $OH^{\bullet}$ scavenger [28]. Pure ethanol was added to the solutions with AuNPs to achieve the final concentration of 5 % ethanol, and the irradiations proceeded as usual. After different periods of laser light exposure (up to 30 minutes), aliquots were placed into a 96-well plate and the fluorescence was measured as for the 3-CCA. All measurements were performed in quadruplicate and a control sample was measured as well. After irradiation, samples were loaded on a agarose gel and the bands were revealed with UV gel doc system (G:BOX Chemi XX9 from Syngene). The results were compared with control samples irradiated for the same periods to evaluate the role of the $OH^{\bullet}$ radicals in the solutions.

7.4. Results and discussion

7.4.1. UV-Visible spectroscopy

The UV-Visible (UV-Vis) spectra (from 190 to 800 nm) of all samples were recorded to evaluate the effects of the exposure to the laser light. It is important to mention the reasons why we used a wavelength range from 190 to 370 nm for most of the UV-Vis measurements. Firstly it is where DNA molecules absorb and, secondly this is because the characteristic surface plasmon resonance (SPR) band of the AuNPs is located around 530 nm and we did not analyse the effects on this spectral region. The necessary increase in the resolution of the spectra from 1 nm step to 0.2 nm in the UV region would lead to a huge increase of the integration time, if data were acquired in the same conditions from 190 to 800 nm (≈3 times longer). Since we were interested in changes on the characteristic DNA band that is at 260 nm and we have observed in previous irradiations that AuNPs SPR is very stable during the exposure periods chosen, we decided to decrease the spectral range and increase its wavelength resolution. We thus aimed to detect any minor differences and/or shifts in the characteristic band of the DNA.

During the experiments, we intended to evaluate the effect of the Nd:YAG laser at 532 nm on DNA molecules as well as on the AuNPs. UV-Vis spectroscopy allows rapid detection of optical changes in the characteristic absorption spectra of the species under study. The characteristic spectra for plasmid DNA and AuNPs in aqueous solutions, which are the control samples without exposure to the laser light, are shown in Figure 7.1. The signature bands are localised at the maximum wavelength of 260 nm for DNA and 526 nm for AuNPs.

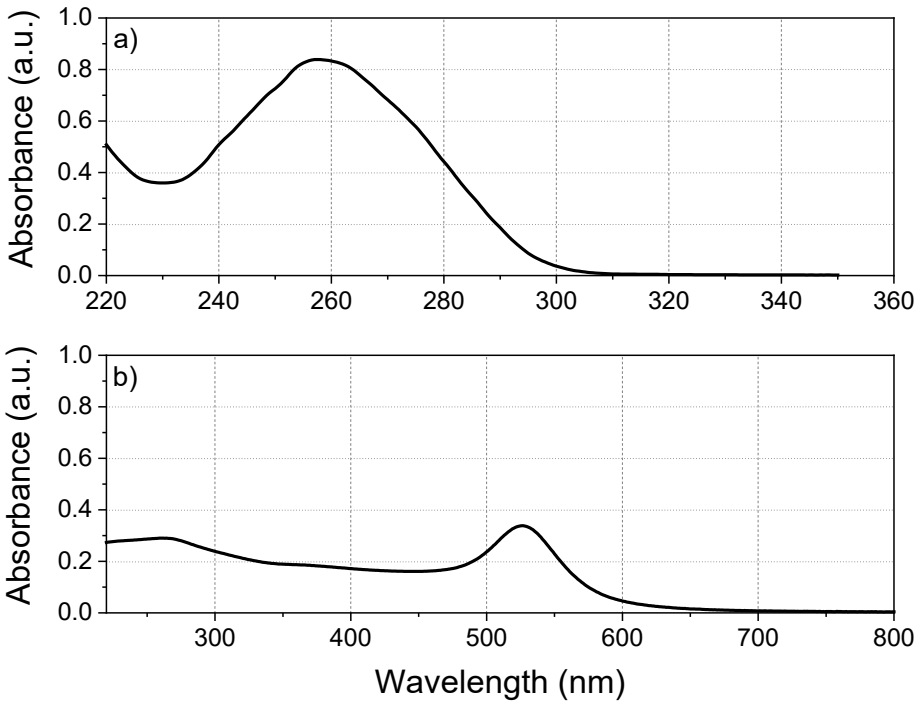

Figure 7.1– Characteristic UV-Vis spectra of a) plasmid DNA and b) AuNPs, both in aqueous solution.

To study the stability of plasmid DNA solutions in both the absence and presence of AuNPs, absorption spectra were recorded up to 30 minutes and the results obtained are presented in Figure 7.2. For all the plots presented below without irradiation, the solutions were kept in the dark at room conditions between measurements.

A similar rational was performed to evaluate the stability of the irradiated samples. We irradiated the solutions in the absence and presence of AuNPs and recorded the spectra in the same conditions used for the non-irradiated samples. The results obtained are also presented in Figure 7.2. All spectra where background corrected and the plots are shown in S.I. 7.1. The first spectra plotted in Figure 7.2a) correspond to the solutions of plasmid DNA without AuNPs, not exposed to laser light and the spectra of Figure 7.2b) to plasmid DNA in presence of AuNPs. Figure 7.2c) and d) show the UV-Vis results for the plasmid DNA irradiated in absence and presence of AuNPs, respectively. These results show that the plasmid DNA optical features do not undergo significant changes in aqueous solution at RT up to approximately thirty minutes.

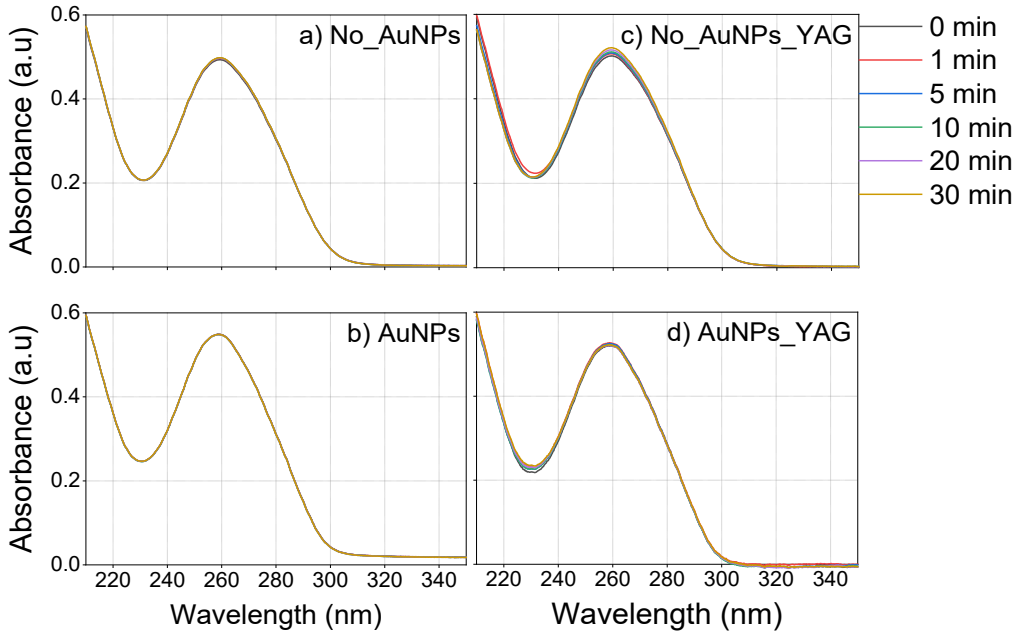

Figure 7.2 – Spectroscopic measurements to assess the stability of plasmid aqueous solution. First two plots in the left (a and b) correspond to non-irradiated samples, and the following to the irradiated ones (c and d). The samples analysed were: a) UHPW non-irradiated, corresponding to the control solution in absence of AuNPs and without irradiation; b) non-irradiated AuNPs, corresponding to the control solution in presence of AuNPs and without irradiation; c) UHPW irradiated, corresponding to the control solution in absence of AuNPs and irradiated; and d) irradiated AuNPs, corresponding to the control solution in presence of AuNPs and irradiated. For all plasmid DNA solutions, the spectra were recorded up to 30 minutes.

Figure 7.2c) presents the spectra of plasmid DNA solutions irradiated with Nd:YAG ns-pulsed laser, without AuNPs, up to 30 minutes. The spectra suggest that the Nd:YAG has minor effect on the DNA signature band, which can be related to the fact that DNA does not absorb visible light. The maximum absorption band of DNA located at 260 nm is due to nucleotides that form DNA strands. Figure 7.2d) shows the results obtained on irradiated solutions with AuNPs and DNA, from which we can conclude that the presence of the AuNPs does not significantly change the absorption spectra of the plasmid DNA. The absence of spectral modifications suggest that DNA molecules are not affected by the laser light when in aqueous solution, with or without AuNPs or the modifications occurred are not detectable by this technique, since DNA molecules can be intact or fragmented and should still give the same 260 nm absorbance. Moreover, to verify the integrity of DNA strands, further experiments with gel electrophoresis or melting point analyses will reveal the DNA structure changes.

Figure 7.3 shows the maximum absorption at 260 nm *vs.* irradiation time for the solutions of plasmid DNA with and without AuNPs. The solutions irradiated in the presence of AuNPs show, in general, slightly higher absorbance (up to 3 %) at this characteristic band of DNA. The contribution from the AuNPs in the DNA characteristic absorption region, should not affect the corrected spectra: the spectra for each irradiation time were corrected with the respective blank solutions. The small variation observed in the absorbance of both samples suggests that DNA is slightly affected by the exposure to Nd:YAG pulsed laser or the presence of AuNPs, however we cannot identify the DNA conformations through these results and thus distinguish between SSBs and DSBs.

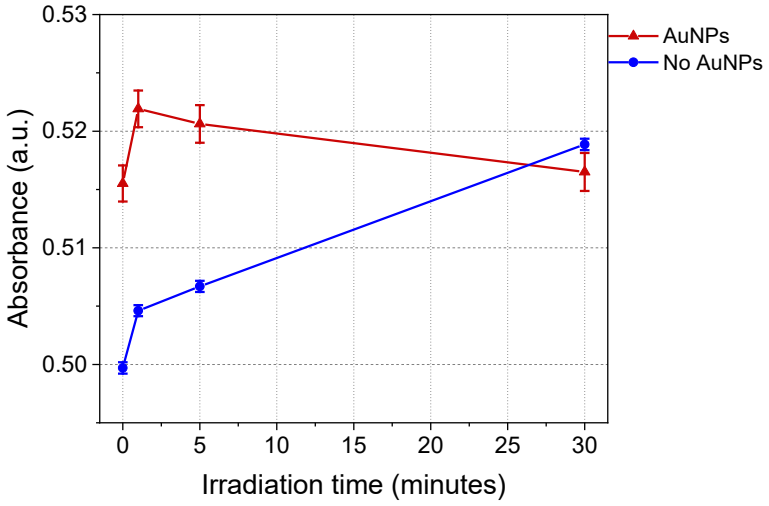

Figure 7.3 – Comparison between maximum absorption at 260 nm, for each illumination period with Nd:YAG laser, for solutions of plasmid DNA with (red) and without (blue) AuNPs.

UV-Vis shows insignificant variations in the DNA absorption band. This can be due to low sensitivity of this technique to changes in the DNA band or because DNA does not absorb visible light, which led us to evaluate the possible damage caused by the exposition to laser light by other techniques, such as agarose electrophoresis gel (AGE) to assess the damage in single-strand breaks (SSB) and double-strand breaks (DSB) on the DNA.

To evaluate the response of AuNPs solutions to laser light, we have measured the UV-Vis spectra of AuNPs solution after laser irradiation up to 30 minutes (Figure 7.4). The characteristic surface plasmon resonance (SPR) band of AuNPs can be observed at 526 nm (black line). With the increase of the irradiation time, one can observe a decrease in the

absorbance of the SPR band accompanied by a blue shift of its maximum and an increase in its FWHM. We suspect that this decrease in absorbance is related to the size reduction of the AuNPs. According to Link [29], a decrease in the size of the NP corresponds to a blue-shift in the absorption spectra, a feature that is visible in Figure 7.4. It is also well established that the broadening of the SPR band is inversely proportional to the radius of the NP [30], [31].

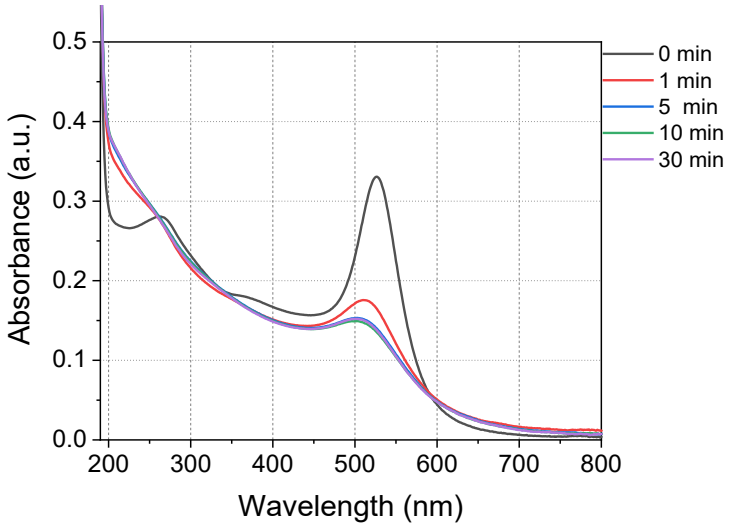

Figure 7.4 – UV-Vis spectra of the surface plasmon resonance (SPR) of AuNPs irradiated up to 30 minutes.

To quantify the SPR absorption band reduction Figure 7.5 shows the peak area of the band at 526 nm *versus* the irradiation time. The difference between the area of the control sample and the one irradiated for 1 minute is approximately 20 %, followed by another reduction at 5 minutes (≈5 %), remaining nearly constant up to 30 minutes of irradiation (25 % of initial area decrease).

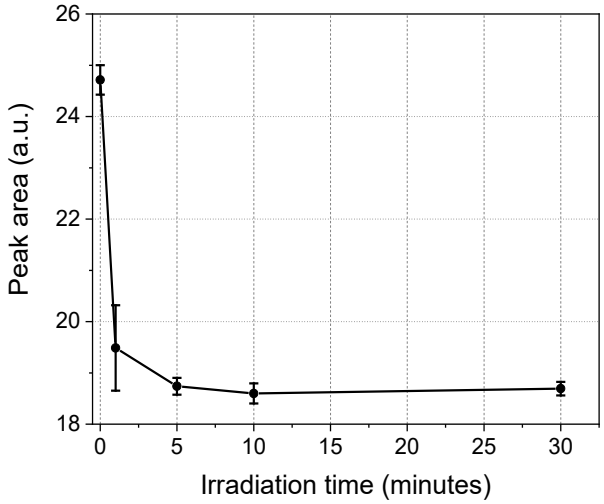

Figure 7.5 – SPR area modifications with the increase to the laser light exposure.

7.4.2. AuNPs size distribution study

To better understand the changes of the AuNPs with the irradiation time, a size distribution study was carried with dynamic light scattering (DLS) and transmission electron microscopy (TEM) techniques. Due to equipment constraints, namely limited user-time for the measurements, we had to choose periods that seemed to be more relevant to analyse. Consequently, the size of AuNPs was assessed for control samples, 1, 5 and 30 minutes of laser exposition. Our previous studies pointed to the possibility of AuNPs size reduction with ongoing Nd:YAG laser exposition [32].

In Figure 7.6, one can observe the effect of the laser light on the diameter of the nanoparticles with the irradiation time, evaluated through DLS and TEM. The values presented correspond to the frequency in counts as a function of AuNPs diameter for each set of samples exposed to Nd:YAG laser light. TEM frequencies were normalized to DLS frequencies, dividing the experimental data by 10, 500, 5000 and 100 for 0, 1, 5 and 30 minutes, respectively. As the UV-Vis absorption spectra of the AuNPs SPR band suggested (Figure 7.5), the AuNPs decrease drastically their size even after with one minute of irradiation, decreasing from 40 ± 3 nm to approximately 1 nm. TEM results consistently showed a broader range of AuNPs sizes, but the averaged and most frequent size of the NPs measured is in good agreement with DLS data. Pearson correlation coefficient obtained was 1.00, see Table 7.1. Given that TEM measurements take a longer time to perform, one can attribute this size differences to some degree of coalescence of the small NPs, forming aggregates and, consequently TEM images and analyses show larger diameters with shapes different than the spherical one expected and observed in the control, see last column of Figure 7.6. These variations could also be related with the technique sensibility, samples preparation, or short acquisition time and additional measurements should be taken with optimized parameters.

In an overall analysis, most of the NPs population for irradiated samples are between 0 and 9 nm. Regarding control samples, the dominant size observed was between 30 and 45 nm.

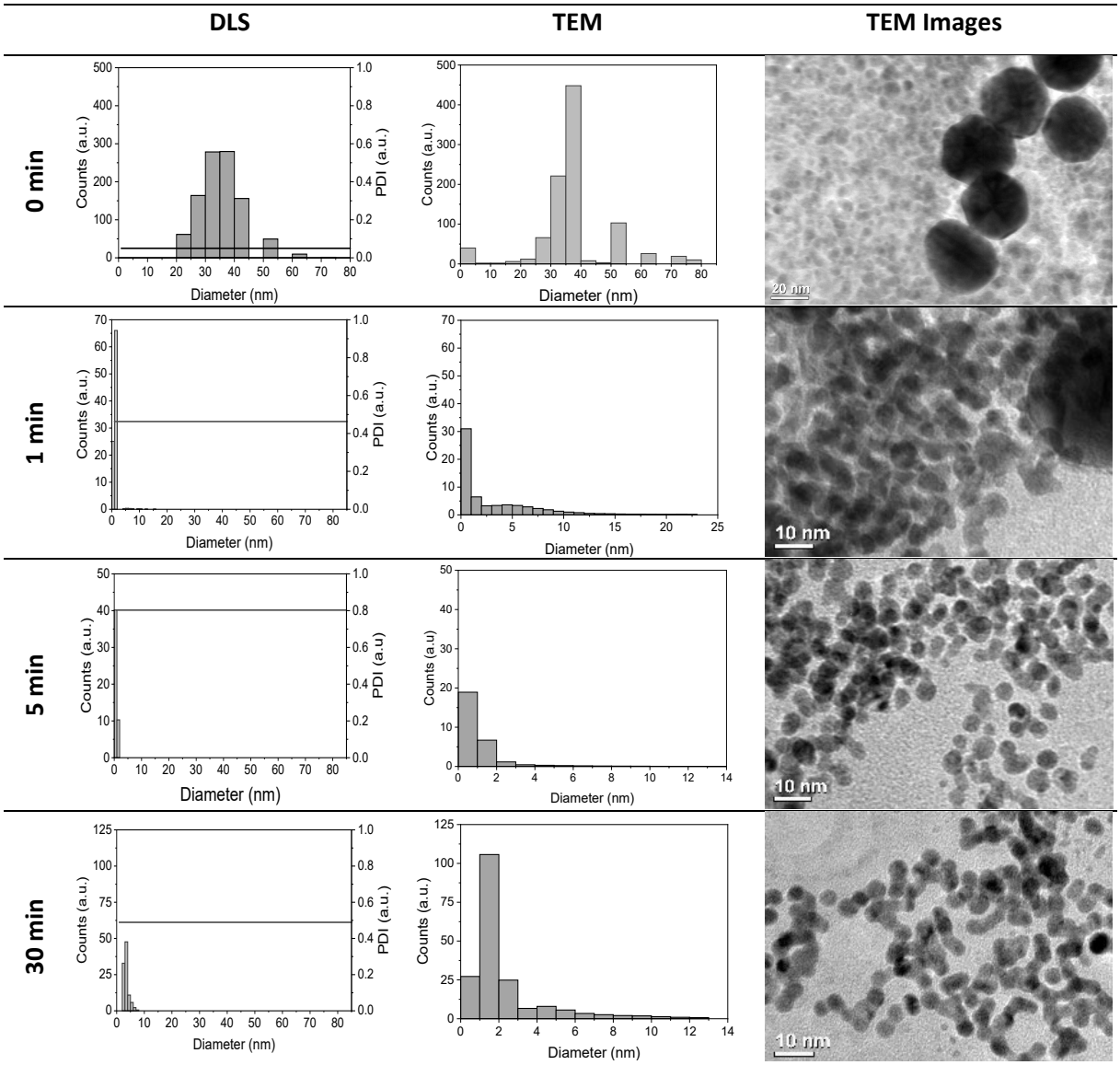

Figure 7.6 - Histogram of size distribution for AuNPs exposed to laser light for different periods obtained for DLS measurements (first column), and for TEM measurements (second column). In the third column TEM images of AuNPs solutions dried on a grid over-night are presented. First line: non-irradiated (mean diameter ≈38 nm); second line: AuNPs illuminated for 1 minute with Nd:YAG laser (mean diameter ≈4 nm); third line: illuminated for 5 minutes (mean diameter ≈ 1nm); and fourth line: AuNPs illuminated for 30 minutes (mean diameter ≈2 nm).

The average diameter found for each sample, with both techniques, is summarized in Figure 7.7.

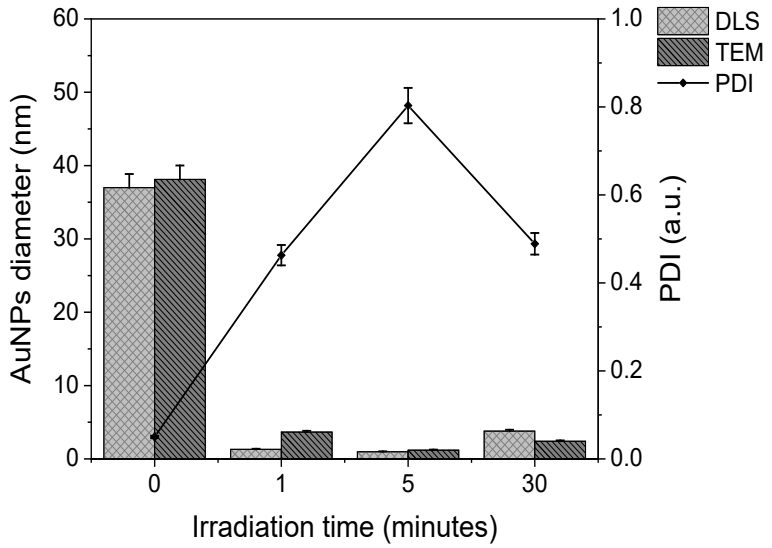

Figure 7.7 – Size distribution measured with two different techniques, DLS and TEM. The results show that both techniques are in good agreement on the size of the AuNPs for the same periods of illumination with the Nd:YAG laser (standard error of the mean is 5 %).

Figure 7.7 shows that the analysis of size distribution by DLS and TEM are in good agreement. With both techniques we measured a reduction of about 90 % of the initial diameter of AuNPs (to ≈1 nm for DLS and ≈3 nm for TEM measurements) after 1 minute of exposure to the laser light. One of the reasons for this effect could be that the energy deposited into AuNPs is sufficient for the destruction of the coagulated NPs resulting in nanoparticles with reduced diameters. However, polydispersity index (PDI) values obtained with DLS experiments revealed that the coalescence of the AuNPs occurs immediately after 1 minute of illumination, achieving a maximum for 5 minutes of exposition. The aggregation of small AuNPs will lead to an increase of the NPs surface area. The evaluation of the damage of DNA molecules as a function of the size of AuNPs needs to be assessed to understand if there is a size dependency on laser-induced DNA damage.

7.4.3. Gel electrophoresis

Changes in the conformation of native supercoiled DNA molecules have been observed with agarose gel electrophoresis following irradiation of plasmid DNA [33]. Supercoiled (SC) and relaxed (R) conformations are characteristic of pure plasmid DNA, and control samples should not present linear (L) forms to ensure DNA integrity [34], [35]. In this experiment, we have exposed the DNA to laser light up to 150 minutes to record the damage caused by long irradiation times (Figure 7.8). The original AGE images from where the DNA conformation bands were calculated are presented in S.I. 7.2.

The effects of the Nd:YAG laser irradiation at 532 nm in plasmid DNA without AuNPs are presented in the left plot of Figure 7.8. The damage driven by irradiation is clearly showed by the decrease of SC accompanied by an increase in the R conformation for up to 150 minutes after which only the R form is present. This is usually attributed to the formation of single-strand breaks (SSB). The linear form, associated with double-strand breaks (DSB), remains approximately zero.

On the other hand, the samples illuminated with Nd:YAG in the presence of AuNPs (rigth plot in Figure 7.8) showed a sharp decrease of the SC form, which disappears after 40 minutes, and a concomitant increase of the R form, which peaks at 40 minutes. After this period, the L form starts to increase up to 150 minutes, reaching ≈35 %.

These results clearly suggest that the DNA damage is enhanced by AuNPs, with faster production of SSB up to 40 minutes and DSB afterwards, as the increasing number of SSB enhances the probability of formation of DSB in plasmid DNA.

The differences observed in Figure 7.8 can be due to several factors namely the increase in the surface area of the AuNPs after their fragmentation during laser exposure, with consequent arise in the production of free electrons and secondary electrons released through illumination and water photolysis with the production and release of free radicals and radical species that will attack DNA nucleosides. It is also important to mention, that fragmentation and damage-induced in DNA strands is related with dissociative electron attachment (DEA), through the action of low-energy electrons in water medium [36], [37]. In

the next section (see 7.4.4. **Erro! A origem da referência não foi encontrada.**) the effect of two free radicals will be explored.

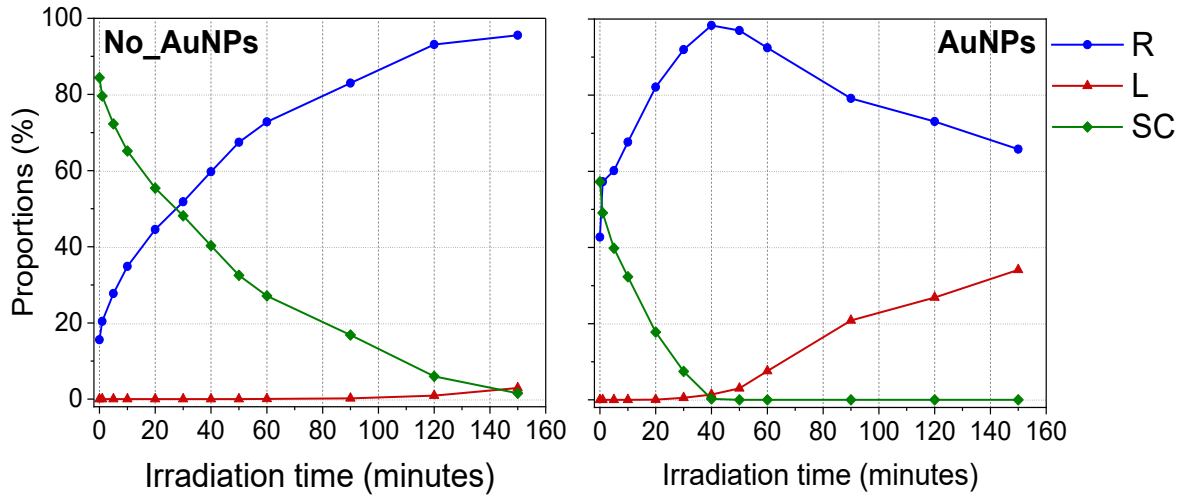

Figure 7.8 – Variation in percentage of different plasmid DNA conformations, R-relaxed, L-linear and SC-supercoiled, irradiated with Nd:YAG laser in absence of AuNPs (left plot) and in presence of AuNPs (right plot), up to 150 minutes (standard error of the mean is 5 %).

Figure 7.9 presents the variation of different plasmid DNA conformations for samples of plasmid DNA illuminated with Nd:YAG light up to 30 minutes in presence of AuNPs without (left plot) and with 5 % EtOH, an $OH^{\bullet}$ scavenger (right plot). The original AGE images from where the DNA conformation bands were calculated are presented in S.I. 7.3**Erro! A origem da referência não foi encontrada.**. It is known that EtOH acts as $OH^{\bullet}$ scavenger, having a protective effect on the damage caused by the free radicals produced during the water radiolysis. For this experiment, the maximum laser exposition was 30 minutes since at this point it was already clear that the damaged caused in DNA is highly due to the presence of AuNPs. In both experiments, the plots were obtained through the separation of DNA forms with AGE technique, thus evaluating the induced DNA strand breaks.

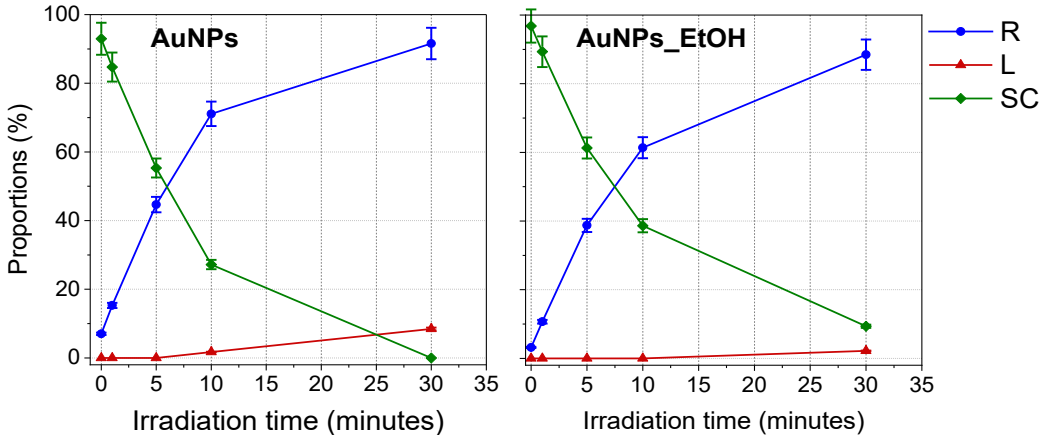

Figure 7.9 – Variation in percentage of different plasmid DNA conformations, R-relaxed, L-linear and SC-supercoiled, irradiated with Nd:YAG laser with AuNPs (left plot) and AuNPs with 5 % EtOH (right plot) up to 30 minutes (standard error of the mean is 5 %).

The results presented revealed a partial inhibition of the damage caused by the AuNPs when 5 % of EtOH is present in the irradiated solution. In fact, the rates of decrease of the SC form and increase of the R form are showed. In addition, it also seems to inhibit the formation of the L conformation.

The results presented for the different samples tested suggest that AuNPs play an important role in DNA damage when exposed to Nd:YAG light, leading to the formation of SSB and DSB. Moreover, they also suggest that water-derived radicals could be responsible for the extensive cleavage of DNA strands since when EtOH is present in the irradiated solutions the damage is reduced and less L from indicting double breaks is seen (Figure 7.9 right plot). Furthermore, we have demonstrated that AuNPs suffer a size reduction when irradiated (results presented in section 7.4.2). The resulting smaller nanoparticles, giving a larger available surface area, seem to enhance water radiolysis and, consequently, free radicals production which may attack the DNA molecules. These findings support the hypothesis of the size dependency of AuNPs on laser-induced DNA damage.

7.4.4. Free radicals

Fluorescence spectroscopy was used to evaluate the free radicals produced during the irradiation and its possible dependence with the size distribution of AuNPs. Two probes were tested, 3-CCA and DHR-123. The first is usually used to detect the formation of $OH^{\bullet}$ radicals in the solution, through the measurements of the fluorescence intensity of the oxidised product 7-OHCCA, and DHR-123 can be related with the production of H_2O_2 radicals, through the measurements of the fluorescence intensity of the oxidised product RHD-123.

The concentration of free radicals produced for each probe during laser illumination, was calculated through the respective linear fit to the calibration curves prepared with concentrations over the range of 0 to 100 µM for 7-OHCCA ($y = 492.04\,x - 71.072;\ R^2 = 0.9998$) and in the range of 8.4×10^{-6} to 6.4×10^{-3}µM for RHD-123 ($y = 7.0 \times 10^{6}x + 40.755;\ R^2 = 0.9924$). The experimental fluorescence intensity obtained was converted to a concentration of the respective fluorescent product through the respective linear regressions, followed by normalization, dividing the irradiated data by the non-irradiated data (control; all results used to construct the graphs are presented in S.I. Table 7.1).

The results obtained are plotted against illumination time and size distribution, measured with DLS, and are shown in Figure 7.10. As previously reported, the dependency of AuNPs with illumination periods is very similar for both techniques analysed and thus we decided to present only the DLS results (see 7.4.2. AuNPs size distribution study).

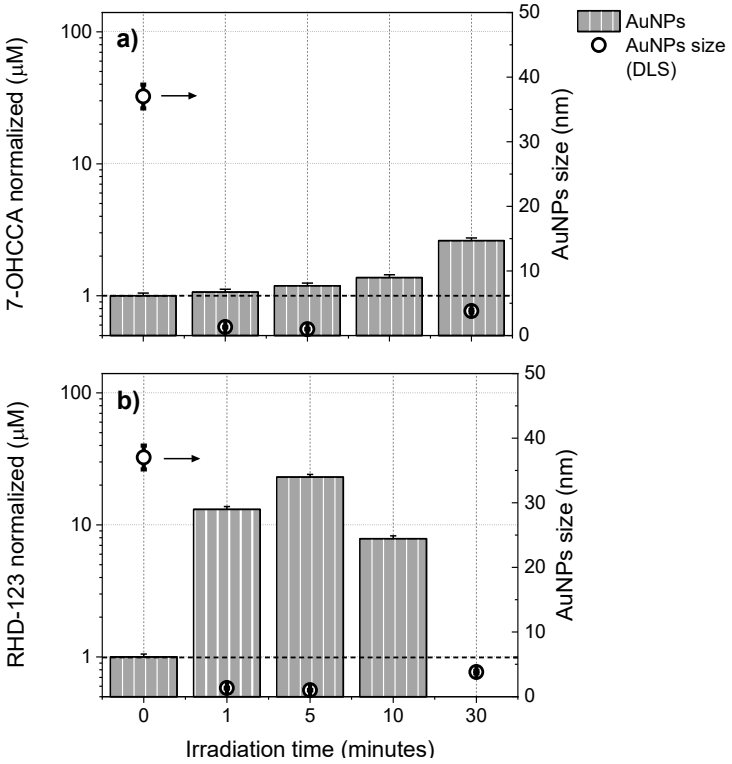

Figure 7.10 – Quenching results for the fluorescent products a) 7-OHCCA with production of $OH^{\bullet}$; and b) RHD-123 with production of H_2O_2, in presence and absence of AuNPs, irradiated up to 30 minutes (n = 12). On the right axis, the average diameter of AuNPs is presented. The error bars presented correspond to 5 % of the standard error of the mean.

By analysing the formation of $OH^{\bullet}$ in the samples studied (see Figure 7.10a), one can say that the presence of AuNPs slightly increases the production of this free radical up to 10 minutes. A major difference is observed when AuNPs are exposed to laser light for 30 minutes. These observations suggest that AuNPs moderately influence the production of $OH^{\bullet}$ radical species, since the abrupt reduction on NPs diameter, observed after 1 minute of illumination, is related with the increase in the formation of this free radical. The analysis of the Pearson correlation coefficient (see Table 7.1) calculated for this samples (DLS, R=-0.34) supports these findings and one possible explanation could be the increase in the total surface area of the smaller AuNPs in solution, enhancing the water photolysis by Nd:YAG laser.

The irradiation of DHR-123 with AuNPs enhances the formation of rhodamine 123 (RHD-123), the fluorescent product of DHR-123 oxidation due to photon illumination (see Figure 7.10b). At an irradiation time of 5 minutes, a maximum of RHD-123 concentration is observed which

suggest that the small size of the AuNPs increases the production of this compound and, consequently, the formation of H_2O_2 species. After this period, the data suggest that a saturation point of the probe used was reached or that probe degradation occurred with higher times of exposition, driven by AuNPs, since the formation of free radicals is accompanied by a decrease on the values recorded for the normalized concentration of RHD-123. Moreover, Figure 7.10 a) and b) suggest that the formation of the free radical $OH^{\bullet}$ is significantly lower when compared to the formation of H_2O_2 reactive species, in the presence of AuNPs. Even the drastic decrease in RHD-123 concentration observed in Figure 7.10b) at 30 minutes, assumes a higher value (7.87 ± 0.39 μM) compared with 7-OHCCA concentration (1.37 ± 0.07 μM, see Figure 7.10a), in the same conditions. This observation suggests that when water molecules interact with the laser light, they tend to form more H_2O_2 species rather than $OH^{\bullet}$, or that two $OH^{\bullet}$ molecules combine very rapidly and originate H_2O_2 [38].

According to several authors [16], [38]–[40], H atom ($H^{\bullet}$), $OH^{\bullet}$, hydrated electron (e^-_{aq}), H_2, superoxide radical ($O_2^{\bullet-}$) and hydrogen peroxide (H_2O_2) are the primary molecular and radical species produced during water radiolysis while it is commonly accepted that $OH^{\bullet}$ is the more abundant species. However, in our experiments, the yield of H_2O_2 is larger in the illuminated AuNPs solutions. One possible explanation for this observation is AuNPs scavenge the free electrons formed during laser exposition, thus decreasing the reaction of oxidation of the probe DHR-123 to the fluorescence product RHD-123. On the other hand, our previous work [32] pointed out that the interaction of 532 nm Nd:YAG laser with AuNPs would most probably lead to electron or thermally induced processes. This hypothesis could explain the predomination observed in the formation of the fluorescence product RDH-123 since the reaction that originates this molecule is driven by electrons. As stated above, several authors already demonstrated that DEA processes and the consequent production of secondary free electrons and radical species will induce damage to DNA strands [36], [37], [41]–[44] .

Figure 7.11 shows the results obtained (see S.I. Table 7.1) with the probe 3-CCA with addition of EtOH, that acts as $OH^{\bullet}$ radical scavenger, in absence and presence of AuNPs. This experiment aims to evaluate if the fluorescence intensity, and consequently the concentration of 7-OHCCA, varies when these hydroxyl radicals are quenched by EtOH, thus resulting in a lower probe concentration at the end of each period of laser exposition. $OH^{\bullet}$

concentration was obtained as described previously. To facilitate reader's appreciation, the data presented in Figure 7.10a) is plotted once more in Figure 7.11.

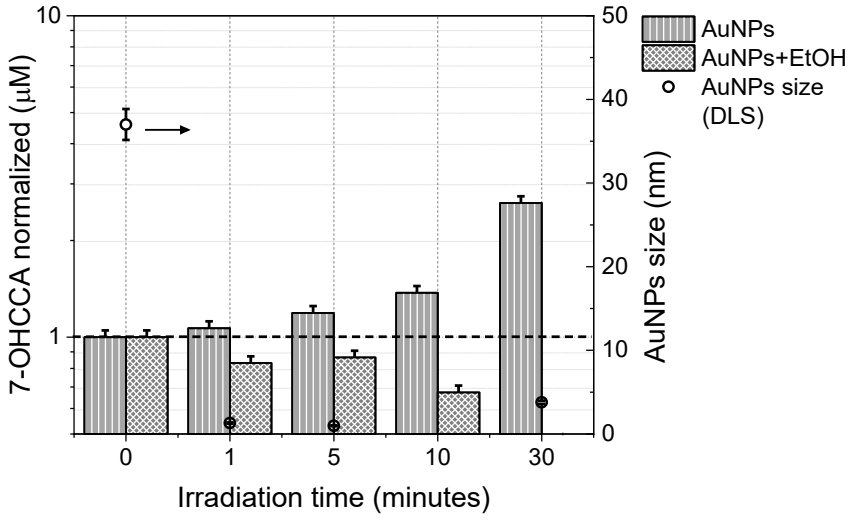

Figure 7.11 – Evaluation of EtOH scavenger effect in $OH^{\bullet}$ radicals, in presence of AuNPs, irradiated up to 30 minutes (n = 4). On the right axis, the average diameter of AuNPs is presented. The error bars presented correspond to 5 % of the standard error of the mean.

As stated previously, the presence of AuNPs increases the concentration of 7-OHCCA, suggesting that AuNPs enhance the production of $OH^{\bullet}$ radicals in irradiated aqueous solutions. On the other hand, a comparison with samples prepared in similar conditions but where EtOH was added (Figure 7.11), reveals the scavenger effect of the EtOH. Moreover, the concentrations experimentally measured for the laser illuminations of solutions with EtOH follow a decreasing tendency with the increase of the exposure time. It is important to point that the values obtained for AuNPs with and without EtOH suggest that these two independent measurements are inversely proportional with a strong correlation, validated by the calculated Pearson correlation coefficient of -0.99 (see Table 7.1). These findings are expected, since the purpose of this study to delay or hinder the oxidation of 3-CCA onto the fluorescent product 7-OHCCA, was accomplished. Consequently, we have confirmed the scavenger capacity of EtOH and also the enhancement of the formation of $OH^{\bullet}$ species upon laser illumination, in presence of AuNPs. Furthermore, the study of EtOH ability to scavenger hydroxyl radicals shows that the damage of plasmid DNA, observed in section 7.4.3., could be

possibly attributed to the action of other radical species or driven by electrons formed upon laser illumination.

Regarding the size distribution of the AuNPs and $OH^{\bullet}$ scavenging by EtOH, the results obtained suggest that the scavenger capacity is independent of the presence and diameter of the AuNPs, and the results are supported by the weak correlation between size distribution methods and 7-OHCCA concentration measured (TEM, R=0.45; DLS, R=0.38).

Similar analysis for H_2O_2 species should be conducted in the future by adding an electron scavenger to the irradiated samples and evaluate the damage-driven by laser exposure. For instance, 5-Bromouracil that was described earlier (Chapter 5) has been used as electron scavenger by several groups [45]–[48].

The matrix of Pearson correlation coefficient was calculated with OriginLab© and it is presented in Table 7.1.

Table 7.1 – Pearson correlation coefficients between size distribution methods and free radical assays in presence of AuNPs.

		7-OHCCA with EtOH	**RHD-123**	**AuNPs Size**	
		AuNPs	**AuNPs**	**TEM**	**DLS**
7-OHCCA	**AuNPs**	**-0.99** [a]	**-0.85** [b]	-0.41 [d]	-0.34 [d]
7-OHCCA with EtOH	**AuNPs**	-	**0.84** [b]	0.45 [d]	0.38 [d]
RHD-123	**AuNPs**		-	-0.09	-0.15 [d]
AuNPs Size	**TEM**			-	**1.00**[a]

The correlation of the data was analysed according the Pearson correlation factors presented by C. Santos (2007) [49], and the results are flagged with letters a, b, c and d, where **a** corresponds to a perfect correlation (|R|=1) ; **b** to a strong correlation (0.8≤|R|<1); **c** to a moderate correlation (0.5≤|R|<0.8); and **d** to a weak correlation (0.1≤|R|<0.5). The results presented in Table 7.1 confirmed that both techniques for the measurements of AuNPs size distribution with the increasing of laser exposition are perfectly correlated (R=1), as expected. In the analysis of the production of $OH^{\bullet}$ (related with formation of 7-OHCCA), the Pearson correlation coefficient suggest that when AuNPs assume smaller diameters the yield of this radical slightly increases, and a weak negative correlation is observed (TEM, R=-0.41; DLS, R=-0.34), especially for TEM measures. However, the yield of $OH^{\bullet}$ when EtOH is present in solution, shows a decrease tendency in function of laser exposition time, suggesting that the production of this radical derives mostly from reactions between water molecules and AuNPs.

This assumption is supported by the values of Pearson correlation coefficients obtained with TEM and DLS, as discussed above (see Figure 7.11). When the results for the production of the fluorescent product 7-OHCCA of illuminated AuNPs with EtOH are compared with the plasmid DNA damage (see Figure 7.9), one can see that DNA damage is still occurring and SSBs and DSBs are being formed. This observation suggests that the DNA-strands are being attacked by other species rather than $OH^{\bullet}$. Additionally, in Figure 7.10 we have showed that the production of the H_2O_2 assumes largely higher values compared with $OH^{\bullet}$, particularly for 1 and 5 minutes of laser illumination. Therefore, the results presented in this work support the relevance of DNA damage-driven through H_2O_2 in the presence of AuNPs. These findings suggest that the formation of H_2O_2 occurs regardless the diameter of the AuNPs in the illuminated solutions. The content of smaller AuNPs dispersed in the solution increase the surface area and, consequently, increases the number of active sites for O_2 reduction. These findings suggest that smaller Au particles have larger number of reduction sites for O_2 and efficiently produce H_2O_2. Moreover, the values obtained for the Pearson correlation coefficient revealed a weak or inexistent negative correlation with both size distribution techniques (DLS, R=-0.15; TEM, R=-0.09).

On the other hand, the strong and negative correlation (R=-0.85) measured between 3-CCA and DHR-123 assays, and the strong positive correlation (R=0.84) between 3-CCA with EtOH and DHR-123 assays, reinforce the hypothesis that the higher yield of radical species formed upon laser exposition by AuNPs is H_2O_2.

The effect of adding EtOH as an $OH^{\bullet}$ scavenger shows that even when the diameter of the AuNPs is smaller, the quenching of the free radical is greater than its production and is highlighted by the strong negative correlation (R=-0.99) of 3-CCA assay with and without EtOH. This observation also suggests that independent of the size of the AuNPs and the increase in the irradiation time, EtOH can quench the hydroxyl radicals formed.

Analysing the damage-driven by free radicals, the results point out that higher rate of DNA attack is due to electron transfer reactions rather than hydrogen atom abstraction in the absence of AuNPs, a conclusion supported by the higher yield of RHD-123 observed and, consequent low yield for 7-OHCCA in the same conditions. Moreover, the Pearson correlation coefficient obtained for experiments of 7-OHCCA with AuNPs *versus* AuNPs and EtOH confirm

this pathway (R=-0.99) but further experiments, particularly with a H_2O_2 scavenger, should be conducted to verify these findings.

7.5. Conclusions

The main conclusions of this work are that the size of the AuNPs directly affect the efficiency of the damaged caused in the plasmid DNA and the water photolysis generates free radicals that will also contribute for this damage. The minor differences observed in UV-Vis spectra, i.e. in the π-π* resonance of DNA molecules, when DNA was illuminated in presence and absence of AuNPs, could be due to the individual spectral contributions of the DNA constituents bases. Namely, plasmid DNA is a mixture of nucleobases and the interaction of 532 nm Nd:YAG laser and AuNPs SPR with the DNA, might individualize the bases but all of them will still contribute to the characteristic absorption band of DNA. Therefore, minimal changes can be detected with this technique. Additionally, we have confirmed experimentally, with DLS and TEM measurements, that AuNPs size reduces drastically upon Nd:YAG laser exposition. Results presented in the evaluation of the damage induced, with AGE experiments, strongly suggest that the presence and fragmentation of AuNPs, upon laser exposition, drastically enhance the formation of SSBs and DSBs in DNA strands. This outcome reinforces the applicability of AuNPs in skin cancer photon therapy. Additionally, smaller AuNPs will be able to fit into the DNA major and minor grooves, so that could be important in helping to localise the damage to the DNA.

Moreover, the addition of ethanol, an $OH^{\bullet}$ scavenger, to the plasmid DNA samples in the presence of AuNPs delays the damage-driven, suggesting that the free radical is mainly interacting with EtOH and not with DNA. The laser light at 532 nm leads to the massive reduction of the diameter of the AuNPs after one minute of exposure (from 40 nm to ≈ 3 nm diameter) when evaluated through two techniques, DLS and TEM. The small diameter of AuNPs enhance the formation of hydroxyl radical.

Former studies [38] showed that it is possible to achieve water ionization with photon energy of approximately 7 eV and with high-intensity lasers with energy greater than 10^{11} $W.m^{-2}$.

In our experiments, we have experimentally measured the intensity of the Nd:YAG laser as 5.0 x 10^{14} $W.m^{-2}$ and this value is in accordance with described by von Sonntag (2006). Therefore, we propose that the Nd:YAG pulsed laser combined with AuNPs enhances the damage-driven to plasmid DNA molecules in aqueous solutions, through two main processes: 1) water photoionization leading to free radical-induced products such as DNA SSBs and DNA DSBs; and, on the other hand, 2) the enhancement of damage induced by AuNPs SPR, also driving to DNA injury.

Further experiments should be conducted to better understand the effect of the size distribution of AuNPs on DNA-radiosensitization and to assess the response of different types of DNA, and to exploit the influence of other damage-inducing mechanisms that are not evaluated in this work.

7.6. Acknowledgements

The authors acknowledge the financial support from the Fundação para a Ciência e a Tecnologia (FCT-MCTES), Radiation Biology and Biophysics Doctoral Training Programme (RaBBiT, PD/00193/2012), Applied Molecular Biosciences Unit - UCIBIO (UIDB/04378/2020) and CEFITEC Unit (UIDB/00068/2020), and scholarship grant number SFRH/BD/106032/2015 to Telma S. Marques and SFRH/BD/135055/2017 to Gonçalo Ferreira. We are also grateful for the OU's logistical support and for the expert technical support provided by C. Hall, R. Seaton, T. Webley and their colleagues in building and maintaining the experiment. Finally, our thanks go to Michael Batham (OU) and Oddur Ingolffson (University of Iceland) for providing the UV-Vis spectrometer and the pulsed YAG laser, respectively. R. Schürmann and I. Bald designed the experimental set-up, methodology and gave training to T.S. Marques. The authors want to acknowledge OriginLab Corporation© for providing a student license to T.S. Marques to analyse the data presented in this work.

Author contribution statement

T.S. Marques, G. Ferreira, S. Eden and N.J. Mason performed the experiments and analysed the data. T.S. Marques, M.A. Śmiałek and M. Raposo wrote the first draft of the manuscript. All authors contributed to the final version of the manuscript.

7.7. References

[1] K. Haume et al., "Gold nanoparticles for cancer radiotherapy: a review," Cancer Nanotechnol., vol. 7, no. 1, 2016, doi: 10.1186/s12645-016-0021-x.

[2] IAEA, "RADIOTHERAPY IN CANCER CARE: FACING THE GLOBAL CHALLENGE," E. Rosenblatt and E. Zubizarreta, Eds. Vienna, 2017.

[3] M. B. Ferruz et al., "New research in ionizing radiation and nanoparticles: The ARGENT project," in Nanoscale Insights into Ion-Beam Cancer Therapy, A. Solov'y., Springer, Ed. Springer International Publishing, 2016, pp. 379–434.

[4] M. E. Khosroshahi, Z. Hassannejad, M. Firouzi, and A. R. Arshi, "Nanoshell-mediated targeted photothermal therapy of HER2 human breast cancer cells using pulsed and continuous wave lasers: an in vitro study," Lasers Med. Sci., vol. 30, no. 7, pp. 1913–1922, 2015, doi: 10.1007/s10103-015-1782-x.

[5] E. Boisselier and D. Astruc, "Gold nanoparticles in nanomedicine: Preparations, imaging, diagnostics, therapies and toxicity," Chemical Society Reviews, vol. 38, no. 6. pp. 1759–1782, 2009, doi: 10.1039/b806051g.

[6] X. Huang and M. A. El-Sayed, "Plasmonic photo-thermal therapy (PPTT)," Alexandria J. Med., vol. 47, no. 1, pp. 1–9, 2011, doi: 10.1016/j.ajme.2011.01.001.

[7] X. Huang and M. A. El-Sayed, "Gold nanoparticles: Optical properties and implementations in cancer diagnosis and photothermal therapy," J. Adv. Res., vol. 1, no. 1, pp. 13–28, 2010, doi: 10.1016/j.jare.2010.02.002.

[8] S. Grellet et al., “Cancer-selective, single agent chemoradiosensitising gold nanoparticles,” PLoS One, vol. 12, no. 7, 2017, doi: 10.1371/journal.pone.0181103.

[9] C. Iodice et al., “Enhancing photothermal cancer therapy by clustering gold nanoparticles into spherical polymeric nanoconstructs,” Opt. Lasers Eng., vol. 76, pp. 74–81, 2016, doi: 10.1016/j.optlaseng.2015.04.017.

[10] R. Schürmann and I. Bald, “Decomposition of DNA Nucleobases by Laser Irradiation of Gold Nanoparticles Monitored by Surface-Enhanced Raman Scattering,” J. Phys. Chem. C, vol. 120, no. 5, pp. 3001–3009, 2016, doi: 10.1021/acs.jpcc.5b10564.

[11] T. S. Marques et al., “Decomposition of halogenated nucleobases by surface plasmon resonance excitation of gold nanoparticles,” Eur. Phys. J. D, vol. 74, no. 11, p. 222, 2020, doi: 10.1140/epjd/e2020-10208-3.

[12] J. L. Ravanat and T. Douki, “UV and ionizing radiations induced DNA damage, differences and similarities,” Radiat. Phys. Chem., vol. 128, pp. 92–102, 2016, doi: 10.1016/j.radphyschem.2016.07.007.

[13] M. Aioub and M. A. El-Sayed, “A Real-Time Surface Enhanced Raman Spectroscopy Study of Plasmonic Photothermal Cell Death Using Targeted Gold Nanoparticles,” J. Am. Chem. Soc., vol. 138, no. 4, pp. 1258–1264, 2016, doi: 10.1021/jacs.5b10997.

[14] P. J. P. Gomes, “Characterization of Molecular Damage Induced by UV Photons and Carbon Ions on Biomimetic Heterostructures. PhD Dissertation,” no. December 2014, 2014.

[15] A. Phaniendra, D. B. Jestadi, and L. Periyasamy, “Free Radicals: Properties, Sources, Targets, and Their Implication in Various Diseases,” Indian J. Clin. Biochem., vol. 30, no. 1, pp. 11–26, 2015, doi: 10.1007/s12291-014-0446-0.

[16] S. Le Caër, “Water radiolysis: Influence of oxide surfaces on H2 production under ionizing radiation,” Water (Switzerland), vol. 3, no. 1, pp. 235–253, 2011, doi: 10.3390/w3010235.

[17] O. Desouky, N. Ding, and G. Zhou, “Targeted and non-targeted effects of ionizing radiation,” J. Radiat. Res. Appl. Sci., vol. 8, no. 2, pp. 247–254, 2015, doi: 10.1016/j.jrras.2015.03.003.

[18] G. B. Saha, Physics and radiobiology of nuclear medicine. Springer New York, 2013.

[19] E. Choi, K. Su Chon, and M. Geun Yoon, “Evaluating direct and indirect effects of low-energy electrons using Geant4-DNA,” Radiat. Eff. Defects Solids, vol. 175, pp. 1042–1051, 2020, doi: 10.1080/10420150.2020.1799372.

[20] Z. Nikitaki et al., “Measurement of complex DNA damage induction and repair in human cellular systems after exposure to ionizing radiations of varying linear energy transfer (LET),” Free Radic. Res., vol. 50, pp. S64–S78, 2016, doi: 10.1080/10715762.2016.1232484.

[21] Z. Nikitaki et al., “Non-DSB clustered DNA lesions. Does theory colocalize with the experiment?,” Radiat. Phys. Chem., vol. 128, pp. 26–35, 2016, doi: 10.1016/j.radphyschem.2016.06.020.

[22] G. Baldacchino et al., “Importance of radiolytic reactions during high-LET irradiation modalities: LET effect, role of O2 and radiosensitization by nanoparticles,” Cancer Nanotechnol., vol. 10, no. 1, pp. 1–21, 2019, doi: 10.1186/s12645-019-0047-y.

[23] M. Gilles, E. Brun, and C. Sicard-Roselli, “Quantification of hydroxyl radicals and solvated electrons produced by irradiated gold nanoparticles suggests a crucial role of interfacial water,” J. Colloid Interface Sci., vol. 525, pp. 31–38, 2018, doi: 10.1016/j.jcis.2018.04.017.

[24] R. Schürmann and I. Bald, “Decomposition of DNA Nucleobases by Laser Irradiation of Gold Nanoparticles Monitored by Surface-Enhanced Raman Scattering,” J. Phys. Chem. C, vol. 120, no. 5, pp. 3001–3009, 2016, doi: 10.1021/acs.jpcc.5b10564.

[25] M. A. Smialek, “Evaluating experimental molecular physics studies of radiation damage in DNA,” 2016, doi: 10.1140/epjd/e2016-70390-3.

[26] M.-A. Park, S. C. Moore, N. Limpa-Amara, Z. Kang, and G. M. Makrigiorgos, “Performance of a coumarin-based liquid dosimeter for phantom evaluations of internal dosimetry,” Nucl. Instruments Methods Phys. Res. Sect. A Accel. Spectrometers, Detect. Assoc. Equip., vol. 569, no. 2, pp. 543–547, 2006, doi: 10.1016/J.NIMA.2006.08.090.

[27] S. T. Wang et al., “Sensitivity of activatable reactive oxygen species probes by fluorescence spectroelectrochemistry,” Analyst, vol. 138, no. 15, pp. 4363–4369, 2013, doi: 10.1039/c3an00459g.

[28] M. Spotheim-Maurizot, M. Charlier, and R. Sabattier, “DNA radiolysis by fast neutrons,” Int. J. Radiat. Biol., vol. 57, no. 2, pp. 301–313, 1990, doi: 10.1080/09553009014552421.

[29] S. Link and M. A. El-Sayed, “Spectral Properties and Relaxation Dynamics of Surface Plasmon Electronic Oscillations in Gold and Silver Nanodots and Nanorods,” 1999, doi: 10.1021/jp9917648.

[30] U. Kreibig and M. Vollmer, Optical Properties of Metal Clusters, vol. 25. Berlin, Heidelberg: Springer Berlin Heidelberg, 1995.

[31] U. Kreibig and L. Genzel, “Optical absorption of small metallic particles,” Surf. Sci., vol. 156, no. PART 2, pp. 678–700, 1985, doi: 10.1016/0039-6028(85)90239-0.

[32] T. S. Marques et al., “Kinetics of Molecular Decomposition Under Irradiation of Gold Nanoparticles with Nanosecond Laser Pulses – A 5-Bromouracil Case Study,” J. Chem. Phys., 2019.

[33] C. Hamelin, “Production of single- and double-strand breaks in plasmid dna by ozone,” Int. J. Radiat. Oncol., vol. 11, no. 2, pp. 253–257, 1985, doi: 10.1016/0360-3016(85)90146-4.

[34] Felix M. Milian, “Estudo in vitro dos efeitos radiobiológicos no DNA plasmidial com radiações ionizantes de baixo LET,” Universidade de São Paulo. Instituto de Física, 2006.

[35] J. R. Milligan, J. A. Aguilera, and J. F. Ward, “Variation of Single-Strand Break Yield with Scavenger Concentration for Plasmid DNA Irradiated in Aqueous Solution,” 1993.

[36] S. E. Huber, M. A. Śmiałek, K. Tanzer, and S. Denifl, “Dissociative electron attachment to the radiosensitizing chemotherapeutic agent hydroxyurea,” J. Chem. Phys., vol. 144, no. 22, 2016, doi: 10.1063/1.4953579.

[37] M. A. Śmiałek, “Evaluating experimental molecular physics studies of radiation damage in DNA*,” Eur. Phys. J. D, vol. 70, no. 11, 2016, doi: 10.1140/epjd/e2016-70390-3.

[38] C. von Sonntag, Free-Radical-Induced DNA Damage and Its Repair. 2006.

[39] G. Baldacchino et al., “Determination of the time-dependent OH-yield by using a fluorescent probe. Application to heavy ion irradiation,” Chem. Phys. Lett., vol. 468, no. 4–6, pp. 275–279, 2009, doi: 10.1016/J.CPLETT.2008.12.006.

[40] J. Ma, “Ultrafast Electron Transfer in Solutions Studied by Picosecond Pulse Radiolysis THESE DE DOCTORAT DE L ’ UNIVERSITE PARIS -SACLAY Préparée à l ’ Université Paris Sud Ultrafast Electron Transfer in Solutions Studied by Picosecond Pulse Radiolysis,” Université Paris Saclay (COmUE), 2015.

[41] I. I. Fabrikant, S. Eden, N. J. Mason, and J. Fedor, “Recent Progress in Dissociative Electron Attachment: From Diatomics to Biomolecules,” Adv. At. Mol. Opt. Phys., vol. 66, pp. 545–657, 2017, doi: 10.1016/BS.AAMOP.2017.02.002.

[42] I. I. Fabrikant, “Theory of dissociative electron attachment: Biomolecules and clusters,” EPJ Web Conf., vol. 84, 2015, doi: 10.1051/EPJCONF/20158407001.

[43] S. Ptasińska and L. Sanche, “Dissociative electron attachment to hydrated single DNA strands,” Phys. Rev. E, vol. 75, no. 3, p. 031915, 2007, doi: 10.1103/PhysRevE.75.031915.

[44] B. Boudaïffa, P. Cloutier, D. Hunting, M. A. Huels, and L. Sanche, “Resonant formation of DNA strand breaks by low-energy (3 to 20 eV) electrons,” Science (80-.)., vol. 287, no. 5458, pp. 1658–1660, 2000, doi: 10.1126/SCIENCE.287.5458.1658.

[45] D. AK, B. H, D. JA, D. JS, and M. D, “DNA damage by OH radicals produced using intense, ultrashort, long wavelength laser pulses,” Phys. Rev. Lett., vol. 112, no. 13, 2014, doi: 10.1103/PHYSREVLETT.112.138105.

[46] J. A. Dharmadhikari et al., “Optical control of filamentation-induced damage to DNA by intense, ultrashort, near-infrared laser pulses,” Sci. Rep., vol. 6, 2016, doi: 10.1038/SREP27515.

[47] L. Sanche, “Interaction of low energy electrons with DNA: Applications to cancer radiation therapy,” Radiat. Phys. Chem., vol. 128, pp. 36–43, 2016, doi: 10.1016/j.radphyschem.2016.05.008.

[48] J. Rak et al., “Mechanisms of Damage to DNA Labeled with Electrophilic Nucleobases Induced by Ionizing or UV Radiation,” Journal of Physical Chemistry B, vol. 119, no. 26. American Chemical Society, pp. 8227–8238, 2015, doi: 10.1021/acs.jpcb.5b03948.

[49] C. Santos, Estatística descritiva : manual de auto-aprendizagem, 3a. Lisboa: Edições Sílabo, 2007.

7.8. Supporting Information

The background correction for the final graphs presented in Figure 7.2, was achieved through subtraction of the control spectrum (S.I. 7.1 column b) of the raw spectrum (S.I. 7.1 column a). The corrected spectrum is presented in column c) of S.I. 7.1.

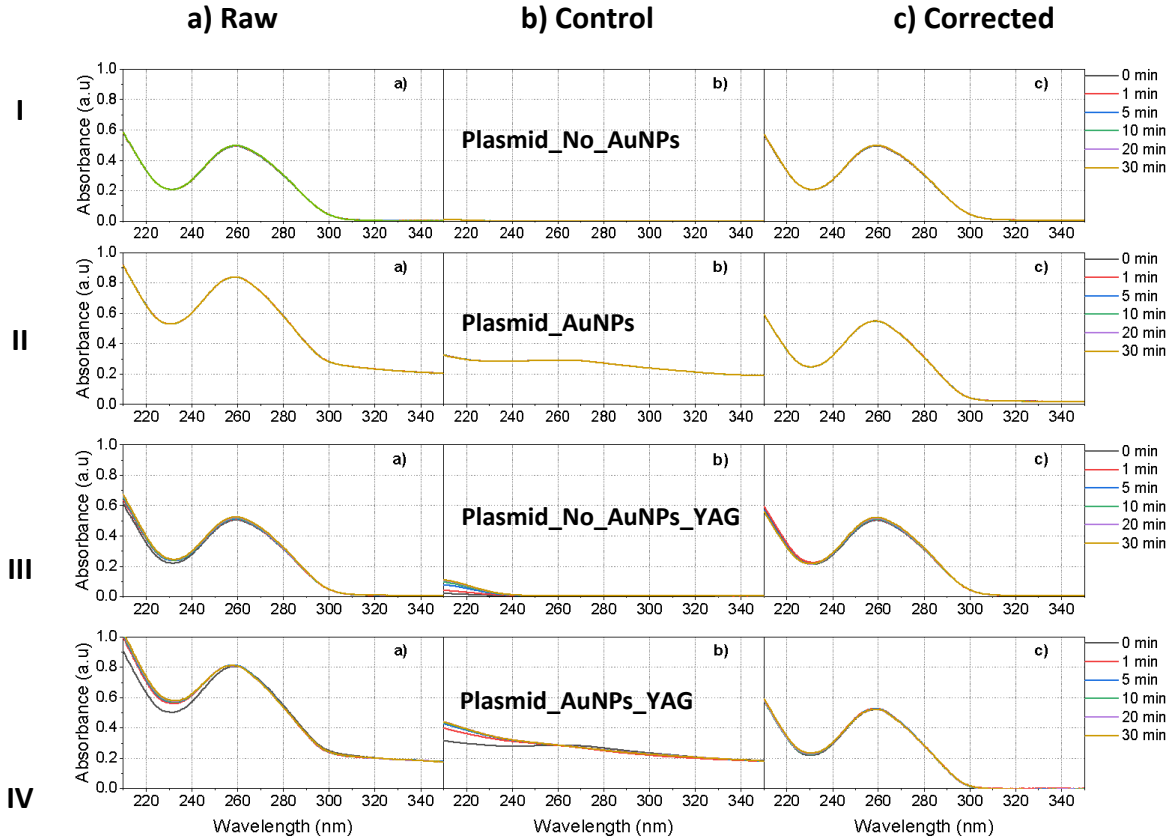

S.I. 7.1 – Spectroscopic measurements of plasmid aqueous solution. Lines numbers **I** and **II** correspond to non-irradiated samples, **III** and **IV** to the irradiated ones. Plasmid DNA solutions without AuNPs are in line **I** and **III** and the results for experiments in presence of AuNPs are presented in lines **II** and **IV**. For all DNA solutions, non-irradiated and irradiated, the spectra were recorded up to 30 minutes.

Figure 7.8 was constructed after the analyses of the DNA bands presented in S.I. 7.2.

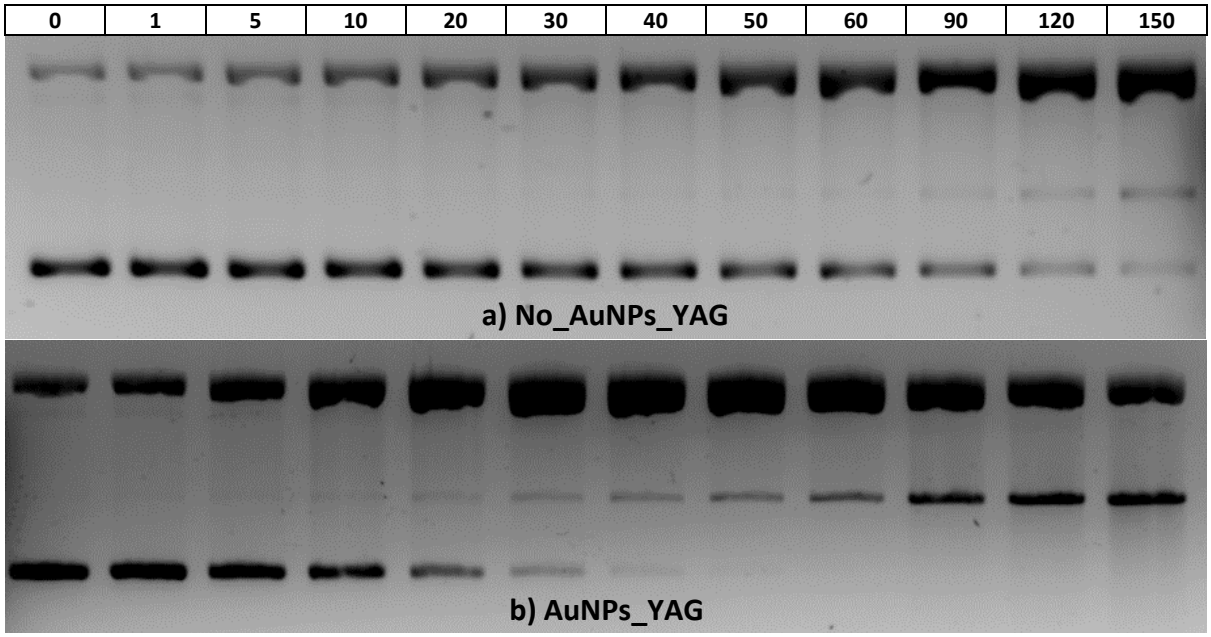

S.I. 7.2 – AGE of plasmid DNA a) in absence and b) presence of AuNPs of AuNPs irradiated with Nd:YAG laser up to 150 minutes. The samples in the lanes are: 0, 1, 5, 10, 20, 30, 40, 50, 60, 90, 120 and 150 minutes.

Figure 7.9 was constructed after the analyses of the DNA bands presented in S.I. 7.3.

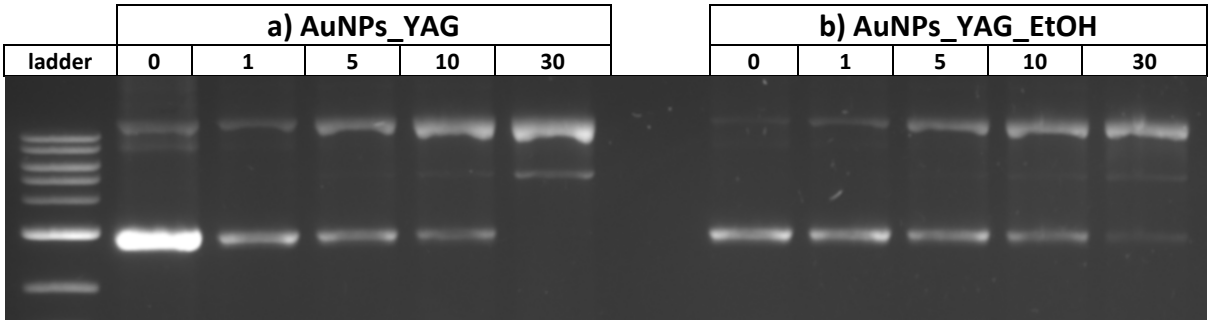

S.I. 7.3 – AGE for samples a) plasmid in presence of AuNPs and b) plasmid in presence of AuNPs and 5 % of ethanol, exposed to Nd:YAG laser up to 30 minutes. The first lane corresponds to the molecular weight (ladder) used in this experiment. The samples in the lanes are: 0, 1, 5, 10, 20 and 30 minutes.

Figure 7.10 was constructed according the data presented in S.I. Table 7.1.

S.I. Table 7.1 – Quenching results for the fluorescent products 7-OHCCA and RHD-123 presented in Figure 7.10. The values presented correspond to average ± 5% of the standard error of the average (n = 12).

Irradiation time (minutes)	7-OHCCA normalized concentration (μM)		RHD-123 normalized concentration (μM)
	AuNPs	AuNPs_EtOH	AuNPs
0	1.00 ± 0.05	1.00 ± 0.05	1.00 ± 0.05
1	1.07 ± 0.05	0.83 ± 0.04	13.09 ± 0.65
5	1.19 ± 0.06	0.86 ± 0.04	22.99 ± 1.15
10	1.37 ± 0.07	0.67 ± 0.03	7.87 ± 0.39
30	2.61 ± 0.13	0.00 ± -0.01	0.00 ± -1.20

Chapter 8

Final conclusions

Final conclusions

This section intends to explore, summarize and link the main conclusions of this doctoral thesis.

The main purpose of this work was to investigate the damage driven by UV and visible radiation in relevant biological molecules and to understand how to enhance such radiation damage, namely by adding AuNPs to illuminated DNA samples. To address this goal, the experimental work was divided in two major parts: 1) the study of the degradation of DNA molecules after exposure to UVC radiation, to design a biological dosimeter that effectively demonstrates and measures the radiation induced damage; and 2) the investigation of the effects of visible light laser radiation (Nd:YAG) on halogenated nucleobases and plasmid DNA conjugated with AuNPs. Hence, the work presented in this thesis is focused on the study of molecular effects of visible radiation on DNA and other molecules of biological interest, namely Uracil, 5-Bromouracil (5BrU) and 5-Fluorouracil (5FU), in presence of AuNPs, to better understand the opportunities for developing photothermal therapy. Concerning this goal, in a first approach, DNA UV radiation damage has been assessed for its potential use as a UV biological dosimeter (Chapter 4). The second study explored the exposure of a well-known radiosensitizer, 5-bromouracil (5BrU) with and without AuNPs by Nd:YAG ns-pulsed laser, studying the laser-driven decomposition kinetics of this DNA nucleobase analogue (Chapter 5). The decomposition of halogenated nucleobases was studied (Chapter 6) to understand the Nd:YAG driven-damage in the DNA and RNA constituents, with the expectation that the increasing knowledge of processes involving simple biomolecules will lead to a better understanding of the behaviour of more complex molecules, such as plasmid DNA (double-stranded molecule). In the final results chapter, damage induced by 532nm radiation from the Nd:YAG laser on plasmid DNA in both the presence and absence of AuNPs was studied and demonstrated the ability of AuNPs to act as radiosensitisers inducing strand breaks and thus may be useful as an agent phototherapy.

A set of the most important conclusions and its interconnections is summarized in the following paragraphs.

Regarding the clarification of the molecular effect of 254 nm wavelength light (UVC), on DNA molecule and to prove the consequent hypothesis that DNA could be used as a biological dosimeter for UV radiation at 254 nm (UVC), experimental results reported in Chapter 4 obtained with DNA solutions clearly demonstrated that these assumptions were correct. The spectroscopic absorbance measurements performed revealed significant changes in the characteristic absorption band of DNA (260 nm). Furthermore, the changes in the absorption spectra could be related to the biological damage, with the increasing exposition to UV light leading to an exponential decrease in the optical absorbance at 260 nm. Additionally, a dependency was found between the pH of the DNA solution and the damage kinetics. The DNA dosimeter was thus tested successfully in the UVC region but further research should be conducted to investigate the applicability of the system in UVA and UVB regions. Since DNA films presented a different behaviour, we can conclude that the presence of water has a major impact on radiation damage to DNA, as expected and this was confirmed by the results presented in Chapter 7.

From Chapter 4, we have learned that DNA molecules are modified by UVC light action, namely in aqueous solutions. Since 5BrU is a well-known radiosensitizer used in photothermal therapy, in Chapter 5 the interaction of laser light with aqueous solutions of this nucleobase analogue was exploited. We found that the decomposition rates for the fragmentation of the BrU ring structure depended on the fluence and the repetition rate of the laser as well as on the starting concentration of 5BrU. Higher laser fluences lead to the decomposition of AuNPs, increasing their surface area and promoting higher local temperatures. This process has the disadvantage of reducing the response of the AuNPs SPR, which decreases as the particle's diameter decrease. Hence, these opposite effects compromise the decomposition rates. Experimental measurements conducted within this work pointed out that the fragmentation of 5BrU occurs is most likely due to electron and/or thermal processes.

However, one question remained unclear from the work described in Chapters 4 and 5. Is the damage observed identically distributed amongst the pyrimidines and purines groups, or is it more prevalent in one of the two groups? To clarify this question, we evaluated the damage,

in similar conditions, in the available pyrimidines (Uracil) and pyrimidines analogues (5BrU and 5FU) in our laboratory and the results obtained were discussed in Chapter 6. This work has shown a drastically decomposition of these molecules, with more relevance in Uracil. Although pyrimidines and purines strongly absorb in UV region, the induced-damage is higher in pyrimidines exposed to UV light. Our work demonstrates that similar effect is observed when halogenated nucleobases are exposed to pulsed laser light and AuNPs.

As the results presented in Chapter 5 allowed us to understand that the decomposition of 5BrU is related to laser fluencies. Hence, in Chapter 6 the dependency of laser fluence was assessed with three halogenated nucleobases, U, 5BrU and 5FU, to study if the fragmentation process of the individual analogue nucleobases, also known as radiosensitisers, was related to the formation/decomposition of U. The setup and methodology of the experiments were very similar to mimic the previous measurements. Whereas the resultant fragments of 5BrU and 5FU will overlap with U in the UV spectrum, we have carried out experiments to infer the modifications of halogenated nucleobases from the spectra of U. The fit of experimental data allowed quantification of the individual NBs concentration in the mixed solution after irradiation. With this methodology, we determined that 5FU presents a higher decomposition rate compared with 5BrU, and fragmentation mainly occurs due to dehalogenation along with damage to the aromatic ring of the base, a confirmation of the results presented in Chapter 5, where the fragmentation of 5BrU rings was proposed. Moreover, the slower decomposition kinetics of 5BrU suggest that recombination of the detached fragments U and Br can occur with the increasing illumination.

Although in Chapter 6 similar trends of decomposition were observed in spectrophotometric measurements, in Chapter 7 the irradiation of plasmid DNA did not show the same tendency in UV-Vis spectra, and π-π^* resonance revealed minimal differences in irradiated samples with and without AuNPs. This could be due to the fact that plasmid DNA is a mixture of nucleobases and the interaction of 532 nm Nd:YAG laser and AuNPs SPR with the DNA, could individualize the bases but all of them will still contribute to the characteristic absorption band of DNA. Therefore, minimal changes can be detected with this technique. Moreover, the hypothesis of the reduction of AuNPs size upon Nd:YAG laser exposition was confirmed in the DLS and TEM measurements.

In Chapter 6 we clearly show that photon-induced damage is triggered by the presence of AuNPs, responding affirmatively to the question “Can AuNPs increase the radiation damage?”. This conclusion and the massive degradation in the analogue NBs observed with our setup, supported the hypothesis that DNA molecules would also suffer modifications. We then tested the system with plasmid DNA (Chapter 7), a more complex and challenging molecule, with the objective of being a better analogue of higher biological systems, namely skin cancer cells.

Moreover, the decrease of AuNPs size distribution was confirmed, proposed in Chapter 5, with ongoing pulse laser (Chapter 7). We conclude that smaller AuNPs present higher rates of plasmid degradation due to 1) an increase of the surface area illuminated; 2) the increase of the temperature in the vicinity of DNA molecules, and 3) eventual explosion of the AuNPs (Coulomb effect) as the result of laser exposition. Furthermore, the illumination of AuNPs with plasmid DNA in aqueous solutions induced SSBs and DSBs in DNA double-strands. In the absence of AuNPs the damage kinetics was slower and less pronounced, confirming the radiosensitizer effect earlier attributed to AuNPs. This work also allowed to verify the production of radical species through water photolysis, namely hydroxyl radical and hydrogen peroxide. It was found that the generation of H_2O_2 seems to be a preferential route and it is enhanced when AuNPs assume smaller diameters.

During these years of experimental work, we also conducted exploratory experiments with plasmid DNA that are not presented in this thesis. Specifically, trials were carried out with pre-illuminated AuNPs for five minutes and, after this period, plasmid DNA was added to the solution. 532 nm laser illuminations were performed in the same conditions used previously. With this experiment, we intended to evaluate if the illumination of DNA with smaller diameter AuNPs lead to higher damage, since we have observed a higher production of damage with smaller diameter AuNPs. Surprisingly, after 5 minutes of irradiation the average size of AuNPs (DLS - 38 ± 8) did not differ from the control solution (DLS control - 37 ± 8). Possible explanations are that the presence of DNA hinders the coalescence of the nanoparticles or the cumulative photon exposition (i.e. 1 minute plus 4 minutes) has a greater effect on the rise of bulk temperature that leads to AuNPs explosion when compared to a single exposition of 5 minutes. In addition, this study did not show significant differences in

the formation of SSBs and DSBs as evaluated by AGE, and the concentration of free radical produced upon laser exposition was not considerably different from the results reported in this thesis. This fact points out that the damage production is more effective in the conditions tested when the exposure to Nd:YAG begins with larger AuNPs.

Regarding the well-known chain reaction of free radicals mechanisms, we have also conducted experiments to quantify the amount of the damage caused. For this, the samples exposed to laser light in the several conditions investigated were kept in the dark at RT for 24 h. After this time lapse, the damage was reassessed with AGE and fluorescence probes, and DLS measurements were also carried out. DLS showed that after 5 minutes of laser exposition, NPs were three times larger and this observation can be attributed to the coalescence of AuNPs after 24h. Furthermore, the yield of 7-OHCCA measured after 24h was slightly higher in irradiated solutions with AuNPs and with pre-irradiated AuNPs, when compared to measurements carried out immediately after laser exposition, suggesting that the generation of $OH^{\bullet}$ continues to occur, the chain reaction did not reach an ending point, even after irradiation ends. Additionally, AGE assays allowed us to verify the enhancement of the damage associated to the free radicals chain reactions since the extent of the relaxed and linear conformal DNA forms increased drastically in presence of AuNPs, with the consequent disappearance of the initial supercoiled form.

In summary, with this doctoral thesis, we had the opportunity to confirm the potential for a new, combined chemo-phototherapy based on visible light radiation and AuNPs, proving the outstanding potential of AuNPs as sensitizers. The novel findings in the interaction of 532 nm ns pulse laser with AuNPs and plasmid DNA, increase the confidence of the efficacy of such treatments in skin cancer treatments although further *in vitro* studies with cells lines, followed by *in vivo* studies, need to be performed to verify the usability of our conjugated system in medical therapies. We expect that the benefits exceed the possible damage caused in the vicinity of the illuminated area, namely if the AuNPs can be placed and confined within the tumour region.

8.5. Future work

Regarding the development of a biological dosimeter, future work should be focused on evaluating the sensitivity of a potential sensor for different incident wavelengths, namely from medical lamps with emission in the UVB (280 to 315 nm) and UVA (315 to 400 nm) regions. Both regions are known to cause sunburns and only 5% of UVA radiation is absorbed through the atmosphere. In recent years, several studies on the damage caused by UVA rays strongly suggest that it enhances the development of skin cancer. It is worth noting that UV exposure is cumulative.

Complementary experimental analysis and techniques are also important to refine and probe the data gathered so far. I consider it essential to explore in detail the following:

- The definitive and direct measurement of the size dependence and morphology alterations both of plasmid DNA and of the AuNPs, as a function of irradiation time. For this purpose, additional TEM measurements should be conducted, including analysing samples with larger irradiation periods.
- Atomic force microscopy-based infrared spectroscopy (AFM-IR) provides chemical analysis and compositional mapping with spatial resolution, far below conventional optical diffraction limits. This technique operates through the tip of an AFM probe, to locally detect thermal expansion in a sample resulting from absorption of IR radiation, providing spatial resolution of AFM combined with the chemical analysis and compositional imaging capabilities of IR spectroscopy. Hence, it would be very useful to evaluate DNA damage with AFM-IR, to visualise the damage induced in DNA molecules and to characterise and quantify the *in situ* damage driven by Nd:YAG and its relation with the presence of AuNPs. The evaluation of the damage extension, showing the SSBs and DBSs formed during the light exposition, would increase the knowledge and understanding of the AuNPs action mechanism.
- Additional IR measurements, using samples with higher DNA concentrations, to signal the sites where the damage is being caused in biological molecules.
- Perform the DHR-123 assay in presence of an electron scavenger to evaluate the production rate of H_2O_2.

Furthermore, *in vitro* assays with melanomas are crucial to investigate the response of skin cancer cell lines to the Nd:YAG laser in the presence of AuNPs. We already know the damage induced in plasmid DNA, thus it would be thrilling and challenging to upscale the system. Following this line of research, it would also be interesting and enriching to carry out *in vivo* assays in animal models, following the consolidation of the *in vitro* assays, to verify the efficacy of photothermal treatment and its applicability in clinical trials, eventually providing this treatment for the entire medical community in the fight against skin cancer and other types of skin lesions.

Annex I

Developed Work

Developed Work

A.1. Publications

- *DNA damage enhancement through radical formation by Nd:YAG laser irradiation in the presence of gold nanoparticles.* T. S. Marques, G. M. Ferreira, M. A. Śmiałek, J. P. Golding, M. Raposo, S. Eden and N. J. Mason. Manuscript under preparation for submission.
- *Decomposition of halogenated nucleobases by SPR excitation of gold nanoparticles.* T.S. Marques, M.A. Śmiałek, R. Schürmann, I. Bald, M. Raposo, S. Eden and N.J. Mason. **European Physical Journal D, Section: Atomic and Molecular Collisions**. pp. 1-9, 74, 222 (2020). ISSN: 1434-6060. (https://doi.org/10.1140/epjd/e2020-10208-3).
- *Kinetics of Molecular Decomposition under Irradiation of Gold Nanoparticles with nanosecond Laser Pulses – A 5-Bromouracil case study.* Telma S. Marques, Robin Schürmann, Kenny Ebel, Christian Heck, Małgorzata A. Śmiałek, Sam Eden, Nigel Mason and Ilko Bald. **The Journal of Chemical Physics, Special Topic on Emerging Directions in Plasmonics**. 152, 124712 (2020); doi: 10.1063/1.5137898.
- *Development of a DNA Biodosimeter for UV Radiation*, Telma S. Marques, Filipa Pires, Gonçalo Magalhães-Mota, Paulo A. Ribeiro, Maria Raposo and Nigel Mason, **Proceedings of the 6th International Conference on Photonics, Optics and Laser Technology (PHOTOPTICS 2018)**, Funchal, Portugal, 25-27 January, edited by Paulo A.Ribeiro and Maria Raposo, SCITEPRESS – Science and Technology Publications, Lda., ISBN: 978-989-758-286-8, 328-333, 2018.

A.2. Posters

- **4 to 6 September 2019 –** Nova Biophysica. Lisbon, Portugal. T.S.Marques, G.M.Ferreira, M.A.Śmiałek, J.P.Golding, M.Raposo, S.Eden and N.J.Mason. *Gold nanoparticles role on plasmid DNA damage with Nd:YAG laser (532nm);*
- **9 May 2018 –** 3rd edition NOVA Biomedical Engineering Workshop (NBEW) FCT/UNL, Lisbon. T.S. Marques, R. Schürmann, S.Eden, Małgorzata A. Śmiałek, I. Bald, M. Raposo

and N. J. Mason; *Effect of gold nanoparticles on the irradiation damage of DNA nucleobasis*;

- **22 to 24 January 2018 –** Argent (Advanced Radiotherapy, Generated by Exploiting Nanoprocesses and Technologies), International Conference, Orly – France. Poster presentation; T.S. Marques, R. Schürmann, S.Eden, Małgorzata A. Śmiałek, I. Bald, M. Raposo and N. J. Mason, *Evaluation of the Damage Induced in DNA Nucleobases by Irradiation of Gold Nanoparticles with Nd:YAG laser (532 nm)*;
- **3 May 2017 –** 2nd edition NOVA Biomedical Engineering Workshop (NBEW) FCT/UNL, Lisbon. Poster presentation; T. Marques, M. Raposo and N. J. Mason, *Effect of UV radiation on DNA multilayer films*.

A.3. Oral presentations

- **31 July and 1 to 3 August 2019 –** *Gold Nanoparticles: Interaction with DNA Molecules Through Visible Light*, T.S.Marques, G.M.Ferreira, M.A.Śmiałek, J.P.Golding, M.Raposo, S.Eden and N.J.Mason, 9th International Symposium "Atomic Cluster Collisions" (ISACC 2019). Canterbury, United Kingdom. Oral presentation. Winner of the prize best young researcher's talk.
- **6 to 9 September 2018 –** *Enhanced degradation of laser-irradiated DNA using Gold Nanoparticles*, Telma S. Marques, Sam Eden, Małgorzata A. Śmiałek, Ilko Bald, Maria Raposo and Nigel J. Mason, CIBB2018: Computational Intelligence methods for Bioinformatics and Biostatistics, 15th International Conference, Monte da Caparica – Portugal;
- **19 to 22 February 2018 –** *Study of the effect on DNA multilayer films when submitted to UV radiation*, Telma S. Marques, Maria Raposo and Nigel J. Mason, COST, Final Workshop and MC Meeting, Monte da Caparica – Portugal;
- **25 to 27 January 2018 –** *Development of a DNA Biodosimeter for UV Radiation*, Telma S. Marques, Filipa Pires, Gonçalo Magalhães-Mota, Paulo A. Ribeiro, Maria Raposo and Nigel J. Mason, Photoptics 2018, 6th International Conference on Photonics, Optics and Laser Technology, Funchal, Madeira – Portugal.

A.4. Organizing committee

- **6 to 9 September 2018 –** Organizing committee of CIBB2018: Computational Intelligence methods for Bioinformatics and Biostatistics, 15th International Conference, Monte da Caparica – Portugal;
- **19 to 22 February 2018 –** Organizing committee of COST, Final Workshop and MC Meeting, Monte da Caparica – Portugal;
- **17 to 20 July 2015 –** Organizing committee of POSMOL 2015 for the XVIII International Workshop on Low-Energy Positron and Positronium Physics & the XIX International Symposium on Electron-Molecule Collisions and Swarms, Universidade Nova de Lisboa Rectorate building, Campus de Campolide, Lisbon – Portugal.

A.5. Workshops participation

- **9 May 2018 –** 3rd edition NOVA Biomedical Engineering Workshop (NBEW), FCT/UNL, Lisbon;
- **3 May 2017 –** 2nd edition NOVA Biomedical Engineering Workshop (NBEW), FCT/UNL, Lisbon;
- **9 March 2017 –** Seminar Correlative Raman Imaging: New trends for nano and biomaterials, Lisbon;
- **13 November 2015 –** Workshop on Imaging and Radiation Biomarkers, Campus Tecnológico e Nuclear, Instituto Superior Técnico, Lisbon;
- **15-16 April 2015 –** LowDose-PT 2015 Biological effects and risks of low dose and protracted exposures to ionizing radiation, Campus Tecnológico e Nuclear, Instituto Superior Técnico, Lisbon.

A.6. Additional experimental work abroad

During this doctoral thesis, I had the opportunity to learn and acquire new skills and know-how that are not demonstrated in this work.

- **First trimester of 2019** – IR measurements were carried out for the cast films of plasmid DNA with and without AuNPs, exposed to laser light. These experiments were performed in two different equipments, Fourier-transform infrared spectroscopy (FTIR) and attenuated total reflection (ATR) measurement. However, regrettably, the results obtained with these experiments were inconclusive and did not add valuable information to clarify and characterise the biological damage of the spectral peaks according to the assigned DNA groups, which are well established in the literature;
- **29 to 30 November 2018 –** Training course on Multiscale Computational Methods for Complex Molecular Systems, MBN Research Center, Darwin Suites, School of Physical Sciences, University of Kent, Canterbury, United Kingdom;
- **1 to 10 November 2018 –** Experimental work at ELETTRA – third-generation Italian synchrotron radiation facility, Basovizza – Trieste (Italy). The experiments performed where PES, XPS and PEPICO measurements of cresols;
- **16 to 24 July 2018 –** Experimental work at ASTRID2 – ultimate synchrotron radiation source, ISA, Centre for Storage Ring Facilities, Aarhus, Denmark. The experiments performed where photoabsorption investigations of some terpenes and terpenoids of medical interest, and thus provide the information of their electronic structure with the aid of computer simulations and other spectroscopical measurements;
- **1 to 14 July and 12 to 25 August 2018 –** Training course on Computational Methods for Complex Molecular Systems at MBN Research Center facilities, Frankfurt Germany, aiming at modeling with MBN Studio software;
- **4 to 8 May 2018 –** MEDICIS-Promed Summer School on "Development and Pre-clinical Evaluation of Radiopharmaceuticals", held in Cascais, Portugal. Organised under the framework of the ITN "MEDICIS- Promed";
- **5 to 12 June 2017 –** Experimental work at ASTRID2 – ultimate synchrotron radiation source, ISA, Centre for Storage Ring Facilities, Aarhus, Denmark. The experiments performed where photoabsorption as well as infrared (IR) investigations of cresols and indole;
- **4 and 5 May 2017 –** Training course on Computational Methods for Complex Molecular Systems, held at the School of Physical Sciences, the Open University, Milton Keynes, United Kingdom;

- **20 to 31 March 2017 –** Training at Bundesanstalt für Materialforschung und -prüfung (BAM) Federal Institute for Materials Research and Testing, Berlin, Germany. Oral presentation of the results obtained during these two weeks entitled “Preliminary studies of nucleobases decomposition by pulsed laser irradiation of gold nanoparticles”;
- **9 March 2017 –** Seminar in Correlative Raman Imaging: New trends for nano and biomaterials, Lisbon (Portugal).

A.7. Awards

- **3 August 2019 –** Winner of the prize Best Young Researcher’s Talk in the frame of the 9th International Symposium "Atomic Cluster Collisions" (ISACC 2019). Canterbury, United Kingdom.